2022

Electronic and Optoelectronic Properties of Two-Dimensional Heterostructures for Next-Generation Device Technologies

Jesse Thompson
University of Central Florida

STARS Citation
Thompson, Jesse, "Electronic and Optoelectronic Properties of Two-Dimensional Heterostructures for Next-Generation Device Technologies" (2022). *Electronic Theses and Dissertations, 2020-*. 1099.
https://stars.library.ucf.edu/etd2020/1099

ELECTRONIC AND OPTOELECTRONIC PROPERTIES OF TWO-DIMENSIONAL HETEROSTRUCTURES FOR NEXT-GENERATION DEVICE TECHNOLOGIES

by

JESSE ERIC THOMPSON
B.S. Gordon College, 2012
M.S. University of Central Florida, 2018

A dissertation submitted in partial fulfilment of the requirements
for the degree of Doctor of Philosophy
in the Department of Physics
in the College of Sciences
at the University of Central Florida
Orlando, Florida

Spring Term
2022

Major Professor: Masahiro Ishigami

ABSTRACT

Since monolayer graphene was isolated in 2004, there has been significant interest in integrating layered materials into innovative device designs and hybrid materials to help solve pressing technological challenges. This is partially because they can typically be thinned to a two-dimensional (2D) form without suffering from roughness-induced scattering and can exhibit thickness-dependent variations in properties such as their energy band gap. This dissertation reports on investigations of electronic and optoelectronic device physics in 2D material heterostructures. The investigation of electronic device physics focuses on the interface between 2D molybdenum disulfide (MoS_2) and gold (Au), which behaves as a resistive switching element (RSE). RSEs are microelectronic switches whose resistances depend on the history of electrical stimuli they have experienced. Prototype computer memory cells utilizing RSEs have demonstrated non-volatile switching behavior and high data retention times, likely enabling more environmentally-conscious computing. The ultimate degree of lateral scaling that MoS_2-based RSEs can attain is currently unknown, but of great importance for determining their role in beyond-silicon computing applications. This work demonstrates, using the metallic tip of a scanning tunneling microscope as an electrode in a model MoS_2-based RSE, that switching events can be recorded even in device areas on the order of tens of nanometers across without the use of lithographic techniques. The investigation of optoelectronic device physics focuses on utilizing hexagonal boron nitride (hBN), an electrical insulator with an ~6.0 eV band gap, to fabricate ultraviolet photodetectors. The main advantage that hBN-based detectors have over Si-based detectors is that they are inherently insensitive to visible and infrared light without needing bulky or expensive optical band pass filters, thus eliminating signal contamination from ambient sources. This work describes the fabrication and characterization of several detectors featuring vertical designs, allowing for greater degrees of both vertical and lateral scaling.

“Adde parvum parvo magnus acervus erit.”

– Publius Ovidius Naso

ACKNOWLEDGMENTS

It has been said that it takes a village to raise a child. Well, in my experience, this proverb is equally true for raising a scientist. During the course of my graduate studies and research, I have been fortunate to be surrounded by many caring people who have generously devoted their time and effort to helping me grow not only as a scientist, but also as a human being. It is my pleasure to enumerate at least a few of them here.

First and foremost, this work would not have been possible without my research advisor, Dr. Masahiro Ishigami. From our very first meeting (which had to be rescheduled, as I accidentally missed the original time, probably working on homework or something), he has provided the freedom to discover what sorts of scientific endeavors interest me most, furnished a plethora of opportunities to learn a host of new skills (useful both in and out of the lab), and helped me to develop a habit of independence. I am sure it has been a challenging journey for us both, but also a worthwhile one that I hope will continue even after graduation. I am also thankful for the many fruitful discussions with the UCF Physics faculty over the years, whether during graduate coursework or over the course of research. In particular, Dr. Robert Peale's patient guidance proved indispensable to the success of multiple experiments and served to deepen my appreciation of electrodynamics (as well as Landau & Lifshitz, volumes 2 and 8).

I would be remiss if I did not acknowledge the many contributions by the hard-working and kind Physics department staff. Their tireless work and devotion is the very life-blood that keeps the department functioning smoothly, enabling the many and varied research endeavors undertaken by faculty and students alike. In particular, I would like to thank Esperanza Soto for continually watching out for the department's grad students, making sure that we never missed important deadlines, answering an endless stream of questions, and generally being there to help when needed. I would also like to thank Nikitta Campbell, Jessica Brooks, Leida Vera Nater, and Sierra Cliburn for all their help over the years with everything from restoring door access to answering countless questions about the intricacies of purchasing and accounting.

In keeping with the collaborative nature of science, I have been fortunate to have a number of friends and family to support me during my graduate school career. For starters, I owe a debt of gratitude to those members of the Ishigami Research Group with whom my own tenure overlapped: Michael Lodge, Brandon Blue, Darian Smalley, and Stephanie Lough. Their camaraderie, as well as their willingness to discuss matters both esoteric (ranging from their favorite stories from obscure folklore to mutual appreciation of languages long in disuse) and mundane (such as interesting recipes, movies, music, and video games), helped to brighten even the most stressful days and make light work of the most arduous tasks. Additionally, I am eternally grateful for the friends and family that supported me throughout my years in the Ph.D. program, including (but not limited to) my brother, Cody Thompson, mother, Deb Diehl, and lifelong friend, Justin Hastings. Without their support and encouragement, graduate school would have been a considerably more Sisyphean experience.

TABLE OF CONTENTS

LIST OF FIGURES

LIST OF TABLES

CHAPTER 1: INTRODUCTION

The desire to improve people's lives and, in so doing, to hopefully improve one's own standing, has driven the process of innovation throughout time. Technological advancement can be attained in a number of ways, including improving the design of an item or process, using better materials or tools, and even making things more compact and portable, for example. This is no less true now, when we have access to an impressive slate of devices which facilitate human interactions, transfer of knowledge, and greater productivity than any other point in history. Consider, for example, the development of computers. One of the most significant innovations in the development of modern computers was the introduction of silicon (Si), as this enabled the invention of the field effect transistor, which underpins all computational hardware. Since their advent, seemingly most innovative effort has been directed toward making increasingly compact transistors. This enabled denser packing of transistors, which in turn allowed for more computational power to become available, even for portable devices. However, after roughly 70 years of innovation, transistor devices are sufficiently small that it has become challenging to continue to scale their physical dimensions without suffering deleterious effects which threaten their performance. Many ingenuitive people have worked to find ways to overcome these challenges, but it is becoming increasingly difficult to do so. One way to ameliorate this situation is to introduce new materials, either in addition to or as a replacement for Si. Indeed, it is believed that next-generation device paradigms, both in the realm of computing hardware and other applications (such as wearable devices and energy storage) will depend critically on a diverse set of materials "beyond Si".

Two-dimensional (2D) materials are promising candidates for integration into next-generation device architectures. The first reason for this is that films of 2D materials with thicknesses of less than one nanometer can be readily prepared using a variety of techniques. For example, single atomic layers of very high quality 2D materials can be generated by thinning the bulk crystals from which they are made using a variety of facile methods. This is due to the fact that most 2D materials come from crystals that are layered in their bulk form. More specifically, the parent crystals are usually van der Waals (vdW) materials, which means that they are comprised of discrete layers held together by relatively weak van der Waals bonds (this is why graphite works for use in pencils). Additionally, for applications where achieving the absolute highest-quality is not necessarily required, ultra-thin films can be created using bottom up synthesis techniques. Regardless of the sample preparation mechanism, the relative ease of producing ultra-thin samples facilitates electronic devices which are extremely compact in the vertical direction. Additionally, many 2D materials have desirable physical properties, such as thermal stability [1–3], chemical inertness [4], a high degree of flexibility [5, 6], and high thermal conductivity [7, 8]. Finally, some 2D materials are semiconductors that exhibit a thickness-dependent properties. One prominent example is that, in transition metal dichalcogenides (TMDs), the electronic band gap tends to increase with decreasing sample thickness. Additionally, the modulation of the band gap can be accompanied by an indirect-to-direct band gap crossover by controlling the sample thickness [9, 10] or strain [11].

The motivation of the work described in this document is broadly to help facilitate the integration of 2D materials into next-generation device technologies. More specifically, this work was aimed at studying novel methods of characterizing 2D material-based devices and testing alternate methods and designs for fabricating such devices. The first chapter of this dissertation involves investigating the role that scanning tunneling microscopy can play in providing useful engineering information regarding the lateral scaling limit of resistance-based logical elements based on 2D semiconducting materials. The second portion of this dissertation, comprising Chapters 3 and 4, focuses on implementing a more compact and, therefore, likely more scalable, ultraviolet photodetector design utilizing an atomically-thin tunneling barrier.

CHAPTER 2: LATERALLY-CONFINED RESISTIVE SWITCHING IN MOLYBDENUM DISULFIDE

2.1 Introduction

Modern computers utilize multiple transistor-based technologies to store data and perform calculations, among other tasks. For example, transistors play a pivotal role in forming the logic elements that facilitate the complex calculations that computers carry out. Transistors are also one of the key components, along with capacitors, comprising the random access memory (RAM) cells that provide the high-speed data storage that is essential to the functioning of a computer's central processing unit (CPU). Finally, transistors and capacitors are also integral components in the construction of flash memory cells, which are being increasingly adopted for persistent data storage devices such as solid state drives and flash drives, edging out magnetic memory (e.g., hard drives) for personal computing devices. Historically, these three categories of devices (logic elements, RAM, and long-term data storage) have been designed and implemented in computer systems as physically separate entities, interconnected and controlled by yet another piece of hardware. Implementing these devices as separate hardware leads to significant bottlenecks in the system performance, as the time needed to pass information back and forth between long-term storage, short-term storage, and the CPU is not insignificant, limiting the throughput of the CPU that could be otherwise tasked with performing additional calculations. This is called the "von Neumann" bottleneck. However, thermal considerations, differences in required performance, and cost have

---

Note: This chapter includes figures adapted from those originally published by Thompson, J. (the author of this dissertation), *et al.*, in the *MRS Advances*, volume 4, number 48 in 2019. A complete citation to this article can be found in the LIST OF REFERENCES: [12]. These figures have been adapted with permission from Springer Nature (see Appendix A for copyright release notice). Figures reproduced herein bear specific notice of permission for reuse in the appropriate figure captions.

prevented engineers from designing a single system which unifies all three sub-systems into one unit.

The last decade has seen the proliferation of software-based machine learning (ML) algorithms which are expected to facilitate disruptive technological advancements in a variety of applications, such as medical diagnostics, autonomous navigation, and smart devices. Many state-of-the-art ML algorithms are neuromorphic in nature, emulating the way that the human brain functions to make predictions, perform classifications, *et cetera*. These algorithms often utilize neural networks (NNs), which are collections of interconnected artificial 'neurons', to encode previously-learned knowledge and apply this knowledge to new situations. Currently, NNs are simulated in software, with the network architecture and synaptic weights stored in memory. However, NNs must be trained on physical devices (such as computer graphics cards or supercomputing clusters) using large bodies of existing application-specific data. Training of NNs benefits immensely from hardware that is capable of parallel processing, as this helps to speed up the training process (which often takes significant amounts of time to complete). Nevertheless, this is a very computationally intensive task that requires a significant amount of memory, since the entire NN needs to be stored in memory for the most efficient training. In practice, memory is limited, possibly only allowing portions of the NN and training data to be loaded into RAM, acted upon, and saved to non-volatile storage before loading the next portion. The energy costs associated with training NNs can be quite high as a result, and the hardware used for training generates a significant amount of heat. This is likely to contribute to the broader ecological issues we face in our time. Additionally, it effectively precludes the use of mobile devices for NN training, which is disadvantageous in a world where distributed computing is becoming ever more important.

The training efficiency of NNs could be improved by using memory and logic elements that consume less power and generate less heat during computations. This would enable devices to implement NNs physically, rather than needing to simulate them using software. In this way, training, storing and usage of NNs could all happen on one device in such a way that parallel processing is inherently utilized, without needing to ever incur the energy and time costs of loading and unloading the NN's synaptic weights, architecture, *et cetera*. Additionally, the use of low power circuit elements would allow for larger NNs with more complex architectures, which are needed to approach the performance of the human brain, but are not feasible with traditional memories (due to excessive energy and cooling costs).

One way to enable low-power memory elements is to transition to a "resistive switching" paradigm. Resistive switches are two-terminal devices that utilize electrical resistance to physically represent and store data. Critically, the resistance state of the switch can be tuned by the application of an external stimulus, such as an electric field. This manner of storing data has an advantage over capacitor-based paradigms because electrical power is only applied to the memory cell during read or write operations, and no voltages are maintained across any of the elements. The lack of a persistent voltage means that there will not be any leakage current, and therefore refresh operations are not needed for resistive switches (in principle). The absence of leakage current is the primary benefit of resistive switching elements (RSEs) for low-power memory applications.

2D materials are promising candidates to serve as the active material in resistive switches. Some general benefits of utilizing 2D materials in device applications were discussed in Chapter 1. In addition to these, another advantage to using 2D materials in devices is that, unlike other materials, atomically-thin 2D material films do not suffer from roughness-induced electron scattering [13]. As a result, the electrical resistance of ultra-thin films of 2D materials remains finite with extreme vertical scaling. Indeed, ultra-low power resistive switching elements have recently been demonstrated using molybdenum disulfide (MoS_2) [14–17], graphene oxide [18, 19], and hexagonal boron nitride [20–23] as the active materials.

While a number of proof-of-concept 2D material-based resistive switching devices have been implemented on the lab scale, the ultimate degree to which the lateral dimensions of such devices can be scaled remains largely unknown. Ideally, 2D TMD-based memory cells could be scaled down such that their lateral dimensions are on the order of several nanometers. This would eliminate one physical constraint in the fabrication of extremely high-density packing of memory cells. The most straightforward way to determine the ultimate extent to which 2D TMD-based RSEs can be scaled is to fabricate ever smaller devices using lithographic techniques. Fabricating smaller RSEs requires lithographic processes capable of producing devices whose dimensions are below the diffraction limit of even ultraviolet light. While such technology is employed in state-of-the-art semiconductor device fabrication facilities (such as those used by Intel), it is not commonly available to most researchers. Thus, fabricating RSE devices with lateral dimensions on the order of several nanometers is likely to be very challenging in the near term.

The use of probe-based characterization techniques presents a unique opportunity to circumvent the fabrication challenges inherent to producing nanoscale RSEs. Several scanning probe microscopy techniques exist which utilize sharp, conductive tips. This tip, when placed on or very near the surface of a model RSE, could serve as one electrode of the RSE. Thus, the switching behavior of a model RSE device could be interrogated in areas similar to the diameter of the conductive tip employed by such a technique, which is usually on the order of tens to hundreds of nanometers. Conducting atomic force microscopy (C-AFM) is a candidate for performing such characterizations, but its resolution is generally limited to several nanometers, which means that it cannot generally resolve atomic level details of a device's surface. While C-AFM could be sufficient to study the lateral extent of switching in a model RSE, it would likely be unable to reveal atomic-scale variations in the sample, thus hindering correlation of any observed switching behavior with the underlying mechanism. Scanning tunneling microscopy is another probe-based technique that can provide the electronic behavior of a sample or device. Critically, scanning tunneling microscopes (STMs) can be used to resolve the atomic structure of samples, and would therefore afford the opportunity to perform *in situ* device characterizations, potentially enabling correlation of macroscopic switching phenomena with atomic scale changes in morphology and electronic properties. The goal of the work described in this chapter is aimed at utilizing an STM to perform nanoscale investigations on the switching behavior of a model, MoS_2-based RSE.

2.2 Background

2.2.1 *Resistive Switching in Macroscopic Devices*

As discussed above, resistive switching elements (RSEs) are two-terminal microelectronic devices that encode information using the resistance state of the device itself. RSEs usually consist of a metal-insulator-metal (MIM) design, as shown schematically in Figure 2.1. The insulating material is typically considered the active element in an RSE, as the device's resistance depends primarily on the electronic properties of the insulating material. A variety of mechanisms have been proposed to explain resistive switching phenomena, and it is generally understood that such mechanisms are electric field-driven. The reason for this is that the electric field set up in the insulating layer is responsible for causing physical changes to the device, which lead to a change in the observed resistance state. The switching mechanism demonstrated by an RSE depends critically on the material parameters of the device itself. This includes the choice of electrode material (e.g., whether it is electrochemically active or inert) and the insulator (e.g., whether the material has high ion mobility, an abundance of point defects or grain boundaries, significant solubility of the electrode materials, *et cetera*). Additionally, for a given material system, the relative orientation of the insulating material can also affect the device performance, for example by facilitating or hindering ion migration between the electrodes.

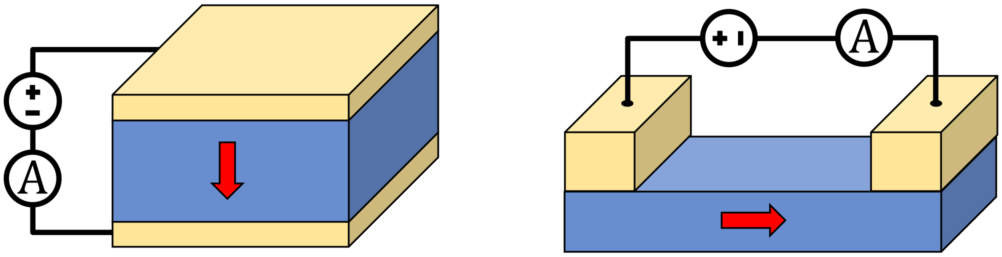

Figure 2.1: Schematic of resistive switching element device architectures. Left: Vertical device. Right: Lateral device.

Some resistive switching devices must undergo a conditioning process before their switching performance becomes stable. The reason for this is that, for some RSEs, the internal state of the pristine semiconducting layer is not properly ordered as to facilitate the switching process (e.g., it lacks a metallic filament for filamentry switching or a sufficient accumulation of oxygen vacancies for interfacial switching). Thus, a certain number of initial voltage sweeps may be required to alter the internal state of the semiconductor to set up the required ordering before stable switching can occur [24]. This process is called electroforming (or "forming" for short). During forming, the high and low resistance states of the device will likely vary considerably from sweep to sweep until it reaches an approximately steady-state value, indicating that the internal ordering is sufficient to allow for switching *via* the specific mechanism the material allows. The On-Off ratio is a common metric used to assess both forming progress and overall device performance. The On-Off ratio is usually determined by taking the ratio of the maximum current through the device when it is in its low resistance state (On) to that in the high resistance state (Off). A high and stable On-Off ratio is desirable for switches to be used for digital applications. Generally, the On-Off ratio will increase until the forming process is complete, though there can still be variation around the post-forming value for some switching mechanisms (e.g., for conductive filaments).

MoS_2 has been successfully integrated into resistive switching elements in various forms in recent history. Lab-scale realizations of monolayer and bilayer MoS_2-based RSE have utilized films exfoliated from synthetic single-crystals, grown by chemical vapor deposition (CVD) and deposited by sulfurization of molybdenum oxide films by atomic layer deposition (ALD) or from natural crystals [14, 15, 25–27]. Additionally, resistive switching has been observed in hybrid devices comprising MoS_2 and organic polymers [17]. A variety of mechanisms have been proposed to explain resistive switching behavior observed in the various device configurations. For example, monolayer-based devices with vertical architectures have demonstrated filament-like switching (with the filament being composed of sulfur vacancies) [25], while lateral devices demonstrated grain-boundary-mediated [28] and contact-mediated (interfacial) switching [29]. Additionally, devices based on multilayer or bulk MoS_2 have been reported to feature phase-change switching [30], migration of ionic dopants [26, 31], migration of oxygen ions facilitated by grain-boundaries [16], and filament growth by electrochemical metallization [27]. To date, relatively few studies have investigated the switching behavior at the atomistic level.

The resistance state of an RSE can be altered by the application of an external electric field. There are two families of techniques commonly used to accomplish this task. The first involves the use of direct current (DC). In this family of techniques, a DC voltage is applied between the electrodes of an RSE. The voltage is swept through a desired range, typically starting from 0 V and increasing up to some value (either positive or negative in polarity). At some point during the voltage sweep, when the voltage has reached a high enough value, a sudden increase in the measured current will occur. This corresponds to a change in resistance from a high-resistance state (HRS) to a low-resistance state (LRS). This is referred to as a “SET” operation. Switching that features abrupt changes in current is called “threshold switching”, and the voltage at which the resistance state occurs is referred to as the threshold voltage. Typically, the voltage would then be swept back to 0 V, ideally with the RSE retaining its resistance state in the process (this is required of candidate RSEs for non-volatile memory applications).

A similar operation can be performed to return the device to its high-resistance state (this is called a “RESET” operation). The general process involves again sweeping the voltage applied to the device to a certain threshold, above which the current will suddenly decrease. The polarity and value of the voltage required to perform a RESET depends on the type of switching exhibited by the device. Unipolar switching requires a voltage of the same polarity as the SET process, but at a higher value. On the other hand, a bipolar switching device would require the opposite voltage polarity used in the SET operation, but the magnitude of the RESET threshold voltage need not be larger than the SET threshold. IV curves representing bipolar and unipolar switching schemes are shown schematically in Figure 2.2. Despite the fact that the discussion of this section has thus far referred to RSEs as two-level systems (high and low resistances), it is possible for such devices to exhibit more than two levels. Accessing a particular resistance state (in RSEs that support them) involves controlling the magnitude and direction of the applied field, as well as the duration for which it is applied. Assessing the instantaneous resistance state of an RSE can be done by monitoring the current and voltage. The second family of measuring techniques involves applying AC voltages to the devices, typically in the form of a train of pulses. This strategy allows one to controllably access multiple resistance states of a RSE, which is useful for emulating biological neurons and synapses in neuromorphic computing applications.

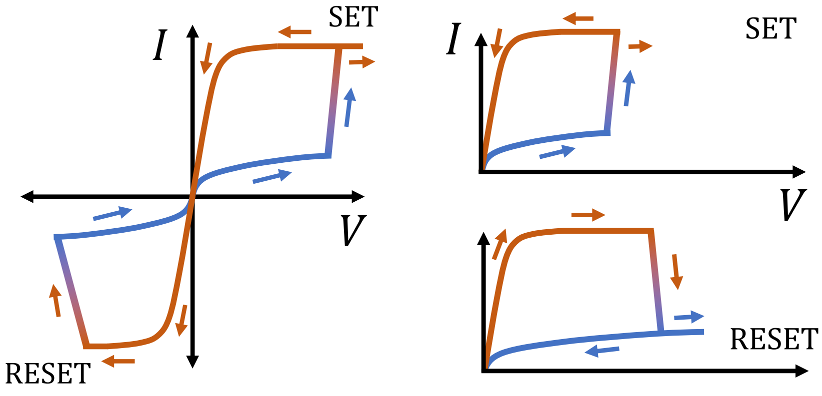

(a) Bipolar switching.

(b) Unipolar switching.

Figure 2.2: Schematic IV curves showing resistive switching schemes. Portions of the IV curve for which the resistive switching element is in a high-resistance state are shown in blue. while portions corresponding to the low-resistance state are shown in orange. Arrows indicate the direction of the voltage sweep during the SET and RESET operations.

A variety of macro- and micro-scale device measurements can be employed to infer the switching mechanism at play in a conventional RSE. DC voltage sweeps are the most common method for assessing a device's electronic behavior. In this technique, a potential difference is applied between the metallic contacts of an RSE and the resulting DC current passing through the device is measured. This voltage is then swept through a desired range, and a set of current vs voltage data is generated and can be plotted as an IV curve. Information regarding the conduction mechanism can be ascertained by fitting different models to the data (e.g., Ohmic, Schottky barrier, Fowler-Nordheim tunneling, trap-assisted, Poole-Frenkel, *et cetera* models). This, in turn, can be used to make an educated guess as to the switching mechanism dominant in the device. As a concrete example, a metallic filament connecting the two electrodes would be expected to demonstrate approximately Ohmic behavior, at least at low voltages.

Additional information can be gleaned from examining the spatial distribution of conducting regions of an RSE. For instance, if increased conductivity is highly localized on the device (i.e., in regions tens to hundreds of nanometers across), it is likely that the switching mechanism of the device is filament-based. Conversely, if the heightened conductivity is distributed over wider regions of the device, interfacial switching is likely dominant. Device area scaling (i.e., fabricating devices with different cross-sectional areas) can help to determine whether a switching mechanism is interfacial. However, scaling devices to ultra-small length scales (tens of nanometers or less) can be challenging, as such fabrication processes require specialized processing and significant process development. With this in mind, probe-based methods of evaluating device behavior and spatial distribution of conductivity are desirable, as they can allow one to circumvent the need for state-of-the-art lithographic processes.

2.2.2 Scanning Tunneling Microscopy Theory

Scanning tunneling microscopy (STM) is a scanning probe microscopy imaging technique that is able to achieve extremely high spatial resolution (much less than 1 nm both laterally and vertically). In typical STM, a sharp metallic tip is brought very close (usually to within 1 nm) to a conducting sample and a potential difference is applied between the tip and the sample. In classical physics, there should be no electrical current detected by an ammeter inserted into the tip-sample circuit, since there is no physical path through which the current can travel. However, the quantum mechanical wavefunctions of the electrons in the tip and the sample (i.e., their orbitals) extend into the intervening space, allowing quantum mechanical tunneling between the two to take place. This tunneling of electrons creates a small tunneling current, usually on the order of a few nanoamperes or less, which is measurable with a low-noise current-to-voltage amplifier (such as a transimpedance amplifier). The details of this tunneling depend on a number of factors, including the tip-sample separation distance (d) and applied voltage (often referred to as the “bias voltage”, V). It is conventional to apply the positive polarity of the bias voltage to the sample, and this convention will be assumed in the following discussion of STM. There are multiple mathematical models which can be used to describe the tunneling phenomena involved in STM, discussions of which may be found in various sources (such as the books by Wiessendanger and Voigtlander) [32, 33]. A summary of the most commonly-used theory is included below.

The Bardeen model is a useful tool for understanding how STM works and how to interpret the data it generates. The Bardeen model was first applied to metal-insulator-metal tunnel junctions and only later applied to STM. In this model, the tunneling current from an STM tip to a metallic sample is given by

$$I = \frac{4\pi e}{\hbar} \int_0^{eV} \rho_{tip}(\varepsilon - eV)\rho_{sample}(\varepsilon)|M(\varepsilon)|^2 d\varepsilon \quad , \tag{2.1}$$

where e is the elementary charge, V is the bias voltage (with the positive polarity applied to the sample), $\hbar$ is the reduced Planck’s constant, ρ_{tip} and ρ_{sample} are the energy-dependent densities of electronic states (DOS) in the tip and sample, and $M(\varepsilon)$ is the energy-dependent matrix element of the Hamiltonian describing the transition of an electron from the tip to the sample. ε is a dummy variable representing an arbitrary energy state between the Fermi level in the sample (corresponding to $\varepsilon = 0$) and the Fermi level in the tip ($\varepsilon = eV$). From this equation, we see that the tunneling current depends not only on the composition of the sample (through its density of states), but also on that of the STM tip. In some cases, experimenters are interested in qualitatively determining the DOS of the sample, so its exact nature does not need to be known *a priori*. Needing detailed knowledge of the tip’s DOS is generally avoided by properly conditioning an STM tip on a standard sample ahead of time, as will be discussed in Section 2.2.5. The crucial part to utilizing this analytical model is evaluating the matrix elements of the Hamiltonian, and this is not easy to do in closed form while maintaining generality. Making several simplifying assumptions, however, allows headway for illustrative purposes. First, if we assume that the sample is homogeneous and uniform, we can reduce the problem from being 3D to 1D. Second, if we assume that the energy of electrons is conserved during tunneling (referred to as "elastic tunneling"), many of the possible matrix elements can be neglected. Third, we assume that both the tip and the sample are metals with similar work functions (typically in the range of 4.5 - 6.0 eV). Finally, assume that the bias voltage is "small" (which typically means that eV is much less than the average of the work functions of the tip and sample). This is essentially assuming that the tunneling barrier is reasonably well-approximated as being rectangular. These assumptions yield an expression for $|M|^2$ that is similar to the transmission coefficient one would expect from a simple finite square well tunneling problem, and thus we refer to this quantity by the same name. The resulting expression is

$$|M(\varepsilon)|^2 \;\rightarrow\; T\left(d,\Phi\right) \propto exp\left(-2d\sqrt{\frac{2m}{\hbar^2}\Phi}\right) \quad ,$$

where d is the tip-sample separation distance, m is the mass of an electron, and Φ is the effective barrier height for this tunneling problem (which is generally taken to be the average of the work functions of the tip and sample). Thus, for very small bias voltages, the tunneling current can be approximated as

$$I(V,d,\Phi) \propto V \;\; exp\left(-2d\sqrt{\frac{2m}{\hbar^2}\Phi}\right) \quad . \tag{2.2}$$

We can reasonably neglect the DOS in Eqn. 2.1 in this case because they are expected to be relatively constant for small voltages. This assumption is essentially the Tersoff-Hamann approximation to the Bardeen model. STM is usually performed with bias voltages of about 1 V or less, which is sufficiently small compared to the work functions of most metals that it is essentially in the low bias regime.

As previously stated, STM is a microscopic technique that can image sample surfaces, typically achieving lateral resolutions on the order of 1 Å and with vertical resolution reaching about 10 pm (or one tenth of an Å). This is due to the fact that the tunneling current that one measures while rastering an STM tip over a sample depends exponentially on the tip-sample separation distance. A rule of thumb is that, for a tip and sample with work functions of about 5.0 eV, a decrease in the tip-sample separation distance by 1 Å will yield about an order of magnitude increase in the tunneling current. So, by maintaining a constant tunneling current as the tip is rastered over a uniform, homogeneous sample, the tip will maintain a constant tip-sample separation distance. An image of the sample's surface can then be mapped out by monitoring the lateral and vertical position of the tip (using piezoelectric drives). This manner of STM imaging is called "constant current" imaging and is the image technique employed in the work described in this document.

There is an important caveat relating to constant current imaging to discuss before concluding this section. Real samples are seldom perfectly uniform and homogeneous in composition, which complicates the interpretation of constant current STM images of their surfaces. Even slight changes in the local density of states (LDOS) of the sample will introduce apparent changes in the heightmap of the sample, even if the sample is perfectly flat across these regions. Such changes in the DOS could occur if the tip scans over regions composed of different materials, for example. It is precisely these imaging artifacts that prevent constant current STM images from being considered truly topographic in nature, and therefore some amount of finesse is required when performing quantitative analysis of non-homogeneous samples. Similar imaging artifacts have been observed in other scanning probe microscopy techniques [34–36].

2.2.3 Physics of Scanning Tunneling Spectroscopy

In addition to their high-resolution imaging capabilities, STMs can also be used to qualitatively assess the LDOS of a sample. This can be done by positioning the tip over a region of the sample for which the LDOS is to be interrogated, and then holding it in place (including in the vertical direction). Then, the bias voltage can be swept while recording the resulting tunneling current. This process is referred to as “scanning tunneling spectroscopy” (STS). To see how this gives information about the qualitative behavior of the sample’s LDOS, consider again Equation 2.1. Taking the derivative of both sides of the equation, considering only tunneling which occurs for electrons with energy $\varepsilon = eV$ (and neglecting the need for fractional calculus to perform the analytic differentiation of the integral), gives

$$\frac{dI}{dV} \approx \frac{4\pi e^2}{\hbar} \rho_{tip}(0) \rho_{sample}(eV) T(V, d, \Phi) \quad . \tag{2.3}$$

The derivative term on the left is commonly referred to as the differential conductance. Assuming the DOS of the tip is either constant or known (see Section 2.2.5) and neglecting the transmission coefficient, this expression can be further simplified to

$$\frac{dI}{dV} \propto \rho_{sample}(eV) \quad . \tag{2.4}$$

From this expression it is evident that the differential conductance can be considered to give a first-order estimate of the LDOS behavior of the sample. It is worth noting, however, that this only really provides a qualitative estimate of the LDOS. A somewhat more quantitative estimate could be attained by using a more nuanced model for the tunneling current and its constituent parts. For example, numerical calculations could be done using an *ab initio* simulation and compared to measured STS data.

2.2.4 Preparation of Tungsten Tips for Use in STM

STM imaging and spectroscopy require a microscopically sharp, clean, and stable tip, as described in Section 2.2.2. STM tips, including the one used during this work, are commonly prepared by electrochemically etching tungsten (W) wire. The details of this process can be found in the literature (such as in [37–39]), but a brief sketch is also provided here, along with a schematic shown in Figure 2.3, for completeness. The process generally involves partially immersing a W wire in an aqueous NaOH solution (usually with a 5.0 M concentration). A second wire, usually Pt or some other impervious material, is formed into a ring and submerged so that it rests just below the meniscus of the solution. Then a voltage is applied between the W wire (positive polarity) and the ring counter-electrode (negative polarity). Hydroxide ions in solution then oxidize the outer surface of the W wire, whereupon the sodium ions etch the WO_4^{-2} near the meniscus, thinning the wire in the process. Eventually, the wire in the vicinity of the meniscus will become so thin that the weight of the W wire suspended below the surface will cause a sudden break. When this happens, the lower portion of the wire will fall into the solution, leaving a very sharp point at the end of the suspended wire. As this happens, the voltage must be quickly removed or else the etching process will continue at the suspended wire, thus blunting the wire's apex. After the etching process, the suspended W wire is rinsed in DI water and either loaded into the STM system or stored for future use. This etching process typically produces STM tips with radii of curvature at the tip's apex in the range of 20 - 200 nm.

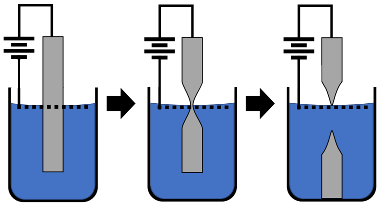

Figure 2.3: Summary of electrochemical etching process for W STM tips.

Prepared STM tips have a surface oxide layer regardless of whether the tip is prepared by etching or, less commonly, mechanical cutting. It is possible to perform STM through this oxide layer, but it is generally preferable to remove it. Doing so narrows the effective tunneling barrier between the metallic tip and the sample (discussed in Section 2.2.2) and prevents oxygen from degasing onto the sample. This, in turn, improves the resolution and stability of the tip. For the tip used in this work, we removed the oxide layer by selectively heating the apex of the tip by electron bombardment (often referred to as “flashing the tip”). In this process, electrons are emitted by a hot tungsten filament (*via* thermionic emission) and accelerated toward the tip (by the application of a voltage relative to a counter electrode). The kinetic energy of the accelerated electrons is transferred to the tip during the collisions, thus effectively heating the tip. Care must be taken, however, to avoid overheating the tip, as this can cause it to melt and become too blunt to yield high-resolution STM images. This process was performed in a dedicated apparatus inside the STM’s vacuum chamber to prevent the reformation of an oxide layer. The experimental details of the tip preparation process are discussed in Section 2.3.2.1.

2.2.5 STM Tip Conditioning

The final step before performing STM/STS is to condition the STM tip. Generally speaking, the apex of a tip tends to be relatively flat on the atomic scale. For example, a lateral cross-section of the tip (when held vertically) about 5 Å above the apex would likely have a radius of about 10 nm (measured from the central axis of the tip) if the apex has a radius of curvature of 100 nm. If such a tip were perfectly clean and bare, it would not be able to achieve high-resolution STM imaging. However, an unconditioned tip is very likely to have a disordered collection of atoms situated at its apex. To achieve the highest spatial resolution and ensure that the tip is stable enough to image for protracted periods, it is advantageous to carefully coat the end of a tip to produce a single, well-ordered asperity composed of metal atoms. As discussed in Section 2.2.2, even a very small change in tip-sample separation distance will likely have a profound effect on the amount of tunneling current in STM imaging. With this in mind, even having a single metal atom (typically with a radius of several Å) at the end of the tip could be sufficient, as long as it is the closest atom to the surface. Therefore, the goal of tip conditioning is to create such an arrangement of atoms at the apex.

Conditioning an STM tip involves performing one or more of a set of actions near a reference sample to form a suitable asperity at the tip’s apex. Tip preparation actions are quite varied, but they can be broadly categorized into two types of actions. The first type involves applying higher bias voltages to the tip/sample (either as a pulse or a sustained increase). This works to rearrange or atoms on the apex by applying a force to atoms near the tip (set up by a non-uniform electric field). The second type involves controllably bringing the tip into contact with the reference sample to either coat the tip with the sample material or scrape off existing apex atoms. This can be done by purposefully approaching the tip toward the sample until it ‘makes contact’ (which is typically taken to mean that the measured tunneling current rises above a certain threshold). Another method involves adjusting the scanning parameters (bias voltage, current setpoint, and closed-loop feedback gains) to make the tip scan closer to the sample and possibly interact with surface features such as step edges. There are two points worth noting about tip conditioning. First, it is very difficult to quantitatively determine the shape and size of an asperity on the tip using either imaging or tunneling spectroscopy, and so this is not usually done in practice. It is technically possible to do so, however, since STM images represent the convolution of the tip shape, surface morphology, and electronic properties of both. The second point to note is that, to date, no deterministic algorithms to produce repeatably high quality tips have yet been determined. This is likely a result of the extreme difficulty of quantitatively characterizing a tip’s shape *in situ* and the fact that a tip’s exact condition at any time depends significantly on the recent history of scanning and spectroscopy performed with the tip. With this in mind, the tip conditioning process has traditionally been considered to be a semi-random process and can be quite time-consuming.

2.2.6 Au(111) and the Herringbone Reconstruction

Au(111) on mica is a common reference sample used in conditioning an STM tip. The reason for this is that Au(111) on mica samples, when properly prepared, can be used both as a diagnostic surface to assess the quality of the tip and as a surface on which to perform the above-mentioned conditioning actions to improve the quality of the tip. However, before Au(111) on mica samples can be used effectively for tip conditioning, the surface of the Au must be cleaned of surface contamination. Cleaning is usually accomplished by performing cycles of argon (Ar) ion sputtering (to remove the surface contaminants in a manner similar to sand blasting) followed by thermal annealing to let the surface smooth itself out after being pitted by the Ar ion sputtering. The experimental details for accomplishing this Au(111) cleaning process are described in Section 2.3.2.2.

After the sputter-annealing cleaning process, the Au surface will have several morphological features that can be used to assess the quality of an STM tip. First, it will be largely covered by atomically-flat plateaus tens or even hundreds of nanometers across, as shown in Figure 2.4a. These plateaus will be bounded by step edges that are about 250 pm tall. Additionally, as the Au(111) cools, the Au lattice will locally buckle to form a more energetically-stable surface [40]. The resulting surface reconstruction, colloquially referred to as "herringbone" (or, more formally, 22 x $\sqrt{3}$), is a superlattice consisting of alternating regions of hexagonal close-packed (hcp) and face-centered cubic (fcc) lattice structures. The hcp and fcc subregions are separated from each other by stripes of atoms which have buckled upward slightly [41, 42]. This reconstruction is shown in Figures 2.4b-c, with the fcc and hcp subregions indicated in Figure 2.4b. The step edges and superlattice are useful features for assessing the quality of an STM tip for STM imaging, as they will not be sharply-resolved by a blunt tip.

The Au(111) surface can be used to judge the suitability of STM tip for STS studies as well as for STM imaging. Single-crystal Au(111) is known to have a relatively constant density of states, ranging from about 1 eV above the Fermi level to about -480 meV below the Fermi level (the Fermi level corresponds to V = 0 V in STM/STS experiments). Then, immediately below about -480 meV, there is a sudden suppression in the density of states [43]. With this in mind, an STS spectrum of Au(111) should appear reminiscent of a step function, with the step occurring at about -480 meV, as shown in Figure 2.5. These features are visible when then Au(111) sample is cooled to cryogenic temperatures. Using liquid nitrogen to cool the sample to 77 K is a common choice, but liquid helium may also be used to achieve a base temperature of 4.7 K. If the Au sample is

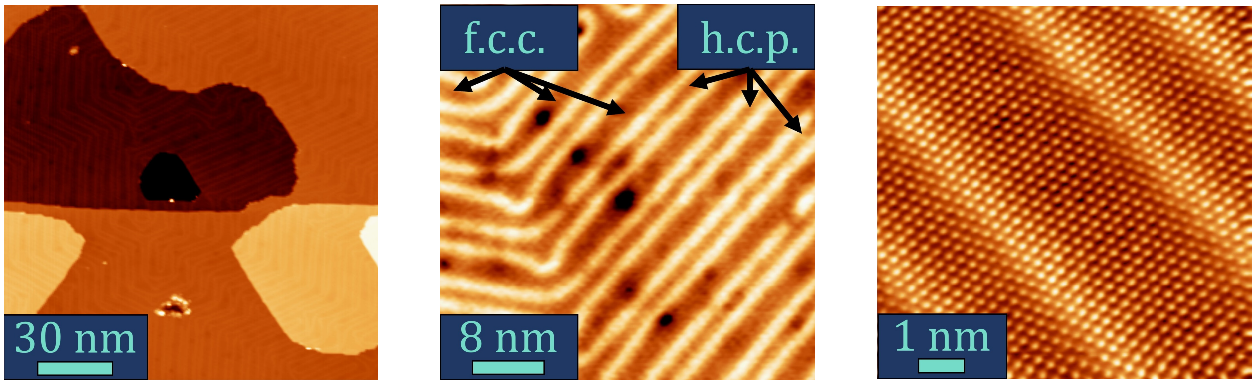

(a) 150 nm region showing atomically-flat plateaus and herringbone reconstruction.

(b) 40 nm region showing herringbone reconstruction with hcp and fcc regions indicated.

(c) 10 nm region showing well-resolved Au atoms and herringbone reconstruction.

Figure 2.4: STM micrographs of Au(111) on mica sample acquired with a well-conditioned tip.

cooled to about 4.7 K, an additional feature will appear in STS spectra which would not normally be visible at 77 K. Specifically, a slight enhancement of the density of states at -480 meV will be present in spectra taken over hcp regions, manifesting as a very slight peak right before the sudden drop-off. Conversely, similar spectra taken over a fcp region will show a slight suppression of the density of states at -480 meV, resulting in a two-level step rather than a single, abrupt step. Recall from Sections 2.2.2 and 2.2.3 that the density of states of both the tip and the sample contribute to the tunneling current.

With this discussion in mind, the conventional way to assess the cleanliness (and therefore the spectroscopic quality) of the tip is to acquire STS spectra on the Au surface and compare them to expected spectra. When the acquired spectra repeatably reproduce the expected behavior, the tip is deemed to be sufficiently clean and ready to be used for spectroscopy of other materials. In this way, Au(111) is commonly used to provide a baseline (though still qualitative) beginning state for the tip to ensure some amount of consistency between data acquisition runs and between different research groups.

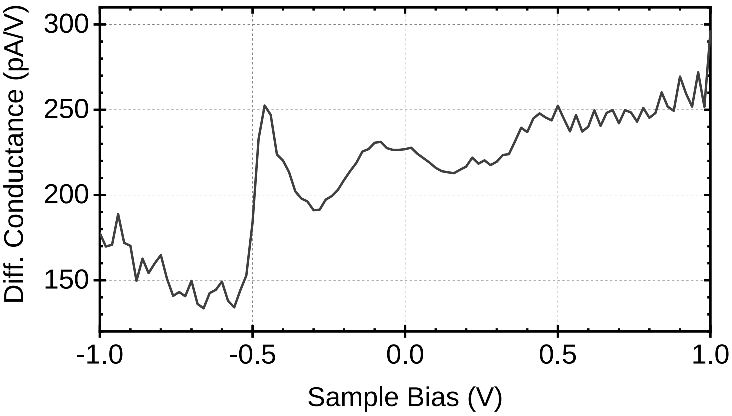

Figure 2.5: Sample STS spectrum of Au(111) acquired with a reasonably clean STM tip.

2.2.7 STM-Based Switching Experiments

As discussed in Section 2.2.1, IV curves are an important part of characterizing the switching behavior of resistive switching devices. In conventional RSEs, the electrodes used to apply a voltage to a RSE are physically in contact with the switching medium (the insulator between the electrodes). In principle, this means that the conduction mechanisms exhibited by the device itself (which can be different for different resistance states) will be either the dominant or the only factor that determines the shape of the IV curve. As such, the IV curve itself can be reliably used to ascertain which mechanism or mechanisms might be at work in the device. However, when an STM tip is used to apply the external voltage to the sample, it will not necessarily be in physical contact with the sample. This means that any current measured during a switching experiment will be a convolution of two separate mechanisms. First, there will be a contribution from the tunneling of electrons from the tip to the sample (e.g., direct tunneling, Fowler-Nordheim tunneling, or an intermediate tunneling regime). There will also be a second contribution corresponding to conduction through the sample itself. This complicates the process of interpreting IV curve data acquired using an STM tip. However, it is still possible to use such data to estimate the change in resistance of the sample from the data. To do so, we will use a simple circuit model that treats the tunnel junction as two resistors connected in series (shown schematically in Figure 2.6). The first resistor represents the effective resistance for electrons tunneling from the tip to the graphene (through the vacuum gap) and is calculated using Ohm's law ($R_{gap} = {}^{V_{bias}}\!/\!_{I_{tunneling}}$). As discussed in Section 2.2.2, the tunneling current (and therefore the "gap resistance") depends on the tip-sample separation distance. The second resistor represents the physical conduction of an electron from the graphene to the Au substrate (which completes the circuit) through the MoS_2 layer. This sample resistance (R_{sample}) is the quantity that we expect to change during a resistance switching event and is ultimately what we need to determine. The total junction resistance, then, will be

$$R_{junction} = R_{sample} + R_{gap} \quad . \tag{2.5}$$

We expect the junction resistance to change during a switching event. With this in mind, we can write two versions of Equation 2.5 (one for before the switching event and one for after). However, the only quantity that we can measure directly in an STM experiment is the total junction resistance before and after a switching event. This means that there will not be enough information to uniquely determine both the gap and sample resistances themselves from an STM IV curve, as there will only be two equations, but four unknowns. To begin remedying this issue, consider the orders of magnitude of typical gap and sample resistances. Vacuum gap resistances are usually on the order of 0.1-10 GΩ (e.g., with V = 1 and I = 1 nA). The resistance through a semiconducting monolayer MoS_2 film in the out-of-plane direction is expected to be about 0.2 - 10 GΩ for conduction through a 0.6-4 nm circular area (about the expected size of a typical asperity at the apex of an STM tip) with an out-of-plane conductivity of 0.23 ${}^{S}\!/\!_{m}$ [44]. With this in mind, we can assume that the gap and sample resistances are approximately equal ($R_{gap} \approx R_{sample}$) before resistive switching (e.g., the "off" state). After resistive switching, the MoS_2 should be more conductive than it was previously, so $R_{gap} \geq R_{sample}$ in the "On" state. Then, combining these expressions with Equation

2.5 and eliminating the gap resistance in favor of the total junction resistance, we see that

$$\begin{aligned} R_{Off} &\approx \frac{R_{junction,off}}{2} \\ R_{On} &\lesssim \frac{R_{junction,on}}{2} \end{aligned} \quad . \tag{2.6}$$

Finally, using the expressions above, the On-Off ratio for a RSE can be estimated as

$$\frac{R_{Off}}{R_{On}} \gtrsim \frac{R_{junction,Off}}{R_{junction,On}} \quad . \tag{2.7}$$

The On-Off ratio is a standard metric which can be used to assess the ease of correctly measuring a signal in a transistor or RSE, similar to the concept of the signal-to-noise ratio. Equation 2.7 provides a means of estimating the lower limit of the On-Off ratio in our experiments.

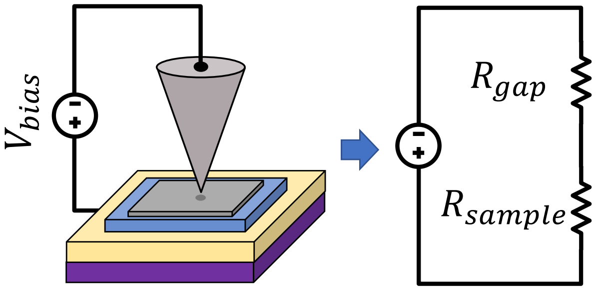

Figure 2.6: STM switching circuit model.

2.3 Methods

2.3.1 *Sample Preparation*

The sample preparation for this experiment involved two separate workflows to prepare individual components, which were eventually combined to make the model resistive switching element. The first workflow involved producing large-area exfoliated MoS_2 on a Au-coated substrate. The second workflow involved preparing the monolayer graphene used to cap the switching element. These workflows are described below and shown schematically in Figure 2.7.

There is an important note to make here. In this experiment, the STM tip will be used as the top electrode for the model RSE device discussed herein. However, we have nevertheless included a graphene top layer in this device. Under normal circumstances, this graphene top layer would serve as the top electrode of the device, particularly for device-scale switching. As such, it is not strictly necessary to accomplish the switching experiments performed in the STM system. Nevertheless, we were interested in visualizing morphological and electronic changes which occur in the RSE as a result of switching. With this in mind, we elected to include the graphene top electrode to more closely simulate what might be observed in future experiments, in which the graphene top layer would be connected to a separate voltage source to facilitate switching independent of the STM tip.

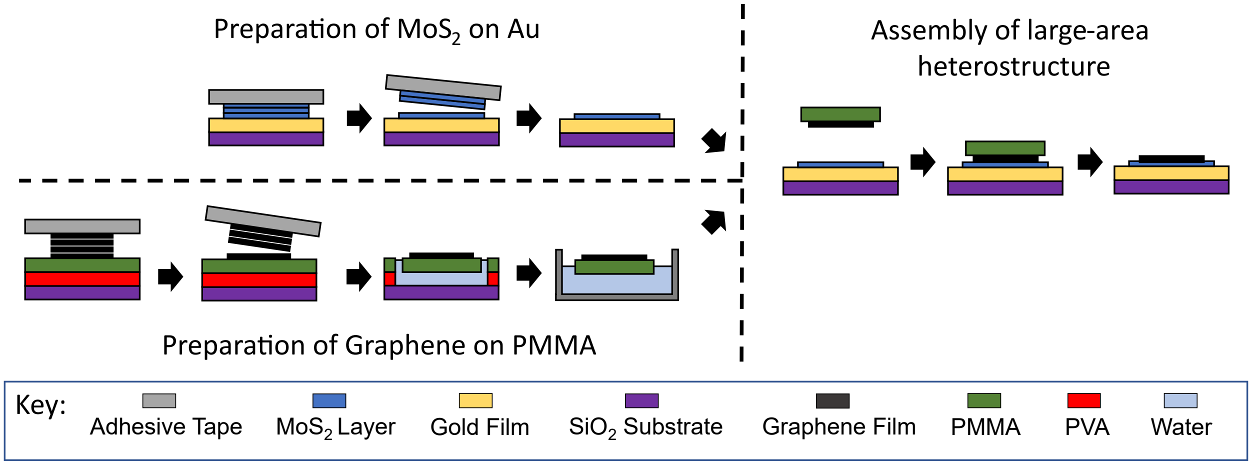

Figure 2.7: Schematic showing workflows used to fabricate MoS_2-based resistive switching element.

2.3.1.1 Preparation of Large-Area Monolayer Molybdenum Disulfide on Gold

The first task to produce a large-area monolayer MoS_2 film was to prepare a MoS_2 crystal for exfoliation. This was done by pre-cleaving a bulk crystal of MoS_2 (a natural crystal sourced from SPI Supplies) about three to five times, applying the formerly cleaved surface to a new piece of tape each time. Pre-cleaving the crystal was important because natural vdW crystals tend to have facets on their outer surfaces, which can make it difficult to generate large, flat areas required for high quality exfoliations. Cleaving the crystal several times effectively strips away the outer facets, leaving crystals which are more suitable for use in exfoliations. We used thermal release tape ("Graphene Transfer Tape" from Graphene Supermarket) to accomplish this.

The model MoS_2 resistive switching element used in this experiment was fabricated on an approximately 1 cm x 1 cm square chip of highly n-type doped Si with 280 nm of thermally-grown and polished SiO_2. This chip was cleaned by sequential sonication in acetone, isopropanol, and deionized (DI) water to remove surface contaminants (including some adventitious carbon present in ambient air and particulates from the cleaving process, *et cetera*). We also found that treating the substrate with any amount of reactive ion etching (using an O_2 plasma) was beneficial for increasing the areal coverage of the final exfoliated monolayer MoS_2 regions.

The next step in preparing the sample involved depositing the Au layer atop the Si chip, with a thin Cr layer between the Au and Si to enhance the adhesion between the two materials. To this end, we loaded the cleaned SiO_2/Si substrate into the vacuum chamber of a thermal evaporator. The chamber was then evacuated using a turbomolecular pump backed by a rotary pump until a pressure of $2 \cdot 10^{-6}$ Torr was reached. Then we degassed the Cr source (Cr-plated W rod, product # CRW-1 from R.D. Mathis) with a shutter interposed between the Cr source and the substrate. This continued until we saw the pressure in the chamber start to fall, indicating that we were evaporating pure Cr rather than CrO_x (the Cr source was effectively acting as a sublimation pump, since Cr is a "getter"). Following this, we opened the shutter, deposited 2 nm of Cr at a rate of 0.5 $^{Å}/_{s}$, and then closed the shutter again. The subsequent Au deposition followed a similar procedure, but the pressure in the chamber didn't decrease during the degassing stage (Au is not a getter). For Au depositions, we used Au pellets (99.999 % purity, product # EVMAUXX50G from Kurt J. Lesker) placed in an alumina-coated Mo boat (product # S2B-AO-Mo, from R.D. Mathis). We deposited 15 nm of Au atop the Cr adhesion layer at a rate of 2 $Å/s$. We found that depositing metal films in these thickness ranges generally resulted in larger-area monolayer coverage of the exfoliated samples. Additionally, depositing at around 0.5 - 1.0 $Å/s$ was sufficient to produce decent samples, but using higher depositions rates (1.5-3.0 $Å/s$) generally produced the best samples. Finally, we let the sample cool under vacuum for about 15 minutes before venting the chamber and retrieving the sample.

The final step in this workflow involved performing a Au-assisted exfoliation of MoS_2. In essence, this simply involved bringing the prepared (pre-cleaved) MoS_2 crystal into contact with the prepared Au-coated substrate and then peeling the bulk crystal away again. This should leave behind regions of monolayer, multilayer, and bulk MoS_2 on the *Au* surface, with monolayer coverage being the largest fraction in the ideal case. After performing a series of trials, we found that this was best accomplished in multiple steps. First, we firmly pressed the prepared MoS_2 flake into the Au surface immediately after it was removed from the thermal evaporator. It has been shown that minimizing the exposure time of the Au surface to ambient conditions is important, because any adventitious carbon or other atmospheric contaminants adsorbed onto the Au inhibit intimate contact between the Au and the MoS_2, reducing the exfoliation efficacy [45, 46]. We found that pressing the MoS_2 into the Au within about 30 seconds from removing from the evaporator was sufficient to yield large-area monolayer regions. After about 30 seconds, though, we observed that the areal coverage of monolayer regions decreases with increasing times, with about 2 minutes being the longest we could wait before pressing to generate appreciable monolayer regions. Additionally, we found that it was important to press the MoS_2 with some amount of force (using one's finger), but that the amount of force did not have a significant impact on the resulting monolayer coverage. The exception to this is that, if one were to press too hard, the substrate could crack.

After pressing the MoS_2 into the Au, we heated the sample (including the tape, crystal, and substrate) on a hotplate to 110 °C. This performed two functions. First, it released the flake from the thermal release tape (100 °C is the release temperature of the tape), leaving it adhered to the Au-coated substrate. Second, it likely helped to drive moisture from the MoS_2-Au interface, thus encouraging stronger adhesion between the two (similar to the role heating plays in wet transfer processes for CVD graphene, as in [47–49]). This is the primary reason we chose to use thermal release tape for this process, as heating other types of tape typically results in the tape melting onto the substrate during heating and producing inferior exfoliation results. Finally, we used a second piece of thermal release tape to pick up the bulk MoS_2 crystal from the substrate for future use, while leaving exfoliated MoS_2 behind on the substrate. We found that the best results were generated when the tape was peeled up slowly (over the course of a few seconds rather than immediately),

2.3.1.2 Preparation and Transfer of Graphene Top Layer

We used mechanical exfoliation to prepare samples of monolayer graphene. However, the process that we used differed from typical mechanical exfoliation (including Au-assisted) techniques. Typical mechanical exfoliation involves exfoliating a crystal directly onto the desired substrate, which would have been very difficult to do with the MoS_2-Au heterostructure that was discussed in the previous section. This is related to the fact that mechanical exfoliation is a stochastic process, and one can never really know in advance what exactly will be produced by an exfoliation. Thus, we could not be sure that, even if we successfully guided a graphite flake to the monolayer MoS_2 region, that anything would actually exfoliate onto the MoS_2 itself. Additionally, there would be no guarantee that any graphene or graphite that adhered to the MoS_2 would be a single- or few-layer. With this in mind, we used a modified exfoliation technique that would allow us to transfer exfoliated graphene onto the MoS_2 in a targeted fashion.

The targeted transfer process used in this experiment involved first producing a sacrificial substrate that would allow us to pick up a desired graphene flake and manipulate it with macroscopic tools. This substrate was a SiO_2/Si wafer onto which we spin coated first a layer of polyvinyl alcohol (PVA) followed by a top layer of poly(methyl methacrylate) (PMMA). An important note is that PVA is a water-soluble polymer, while PMMA is insoluble in water. We then pre-cleaved a bulk graphite crystal (Kish graphite, obtained from Graphene Supermarket) using thermal release tape and then thermally released the cleaved flakes onto the top surface (PMMA) of the sacrificial substrate. Following this, we used additional tape to re-cleave the previously released flake, removing most of the graphite from the PMMA surface. This resulted in mostly bulk graphite and thicker multilayer graphene flakes being left atop the PMMA, but we were able to identify several few-layer flakes by optical microscopy using differences in optical contrast from the substrate.

The final stage of the targeted transfer process involved picking up a selected film of few-layer graphene and transferring it onto the MoS_2 surface. The first step in doing so is to use a sharp object (a dentist's pick in our case) to scribe a ring in the PMMA/PVA around the desired graphene film, thus exposing the PVA in the side walls of the trench (as shown schematically in Figure 2.7). We then used a micropipette to carefully dispense small amounts of water around the outside of the ring such that it wetted the side walls. Since PVA is water-soluble, the PVA film in the immediate vicinity of the scribed circle began to dissolve. Over time, the water spread underneath the island of PMMA with the desired graphene film due to capillary action, dissolving the PVA in the process. Eventually, the water dissolved the entire PVA layer coupling the PMMA and graphene to the substrate and left the PMMA island floating. We then carefully dipped the substrate into a beaker of water in such a way that the floating island remained on the surface of the water in the beaker. Next, we used a small metal loop to pick the floating island of PMMA/graphene up out of the water and left it to dry suspended in air. Once dry, we used a 4-axis micro-manipulator stage to bring the graphene/PMMA into contact with the desired monolayer MoS_2 region on the previously-prepared heterostructure, with the graphene facing downward toward the heterostructure arranged beneath. We did this while viewing both the heterostructure and the suspended graphene film through an optical microscope, adjusting the positioning as we lowered the graphene to ensure that it contacted the region of interest on the MoS_2. After making contact with the MoS_2 we heated the sample stage to 80-120 °C to soften the PMMA, enabling us to remove the loop while the graphene/PMMA remained on the sample. After this, we cooled the sample, then immersed it sequentially in acetone and isopropanol baths to dissolve the PMMA layer. We note that the heterostructure stacking process followed hitherto is expected to yield a sample whose interlayer interfaces are clean at the atomic scale, as the interfacial surfaces should not have been exposed to processing polymers or other contaminants during the stacking.

Before proceeding with more sample preparation steps, we used Raman spectroscopy to confirm the presence of both monolayer graphene and MoS_2 in the region of interest on the sample. This was done using a WITec 300RA confocal Raman system with ~16 mW of illumination by a 532 nm laser. Additionally, the Raman system was set to use a 100X microscope objective lens and a diffraction grating with 1880 $^{lines}/_{mm}$. Acquiring spectra involved 15 accumulations, with each accumulation having a 15-second integration time. Further discussion, including interpretation of the Raman spectra acquired in this way, is given in Section 2.4.

We performed two final annealing steps before we used the sample described here to perform switching experiments. The first was hydrogen-argon annealing, which has been shown to effectively clean the small amounts of PMMA residue left behind on graphene after a solvent rinse [50]. To accomplish this, we loaded the heterostructure into a tube furnace and heated it at 350 °C for one hour with 973 sccm of Ar and 518 sccm of hydrogen gas flowing through the tube. We then mounted the heterostructure to a molybdenum STM sample plate and transferred the sample plate into an ultra-high vacuum chamber adjacent to the STM chamber, whereupon we heated the sample in vacuum (~10^{-9} Torr for one hour to drive off any moisture from exposure to atmosphere. This was accomplished using the heating stage described in Section 2.3.2. Finally, we cooled the sample and stored it under ultra-high vacuum (~10^{-11} Torr) in the STM chamber until we were ready to perform the switching experiments.

2.3.2 Scanning Tunneling Microscopy and Spectroscopy

The STM/STS work described in this document was conducted using a Scienta-Omicron Low-Temperature STM system. Unless otherwise stated, STM and STS data acquisitions were performed in an ultra-high vacuum (UHV) chamber that was maintained at an internal pressure on the order of 10^{-11} Torr. Both the STM scan head and any samples being interrogated were cooled to ~77 K using a bath cryostat (filled with liquid nitrogen) in thermal contact with the scan head and samples. We used a Nanonis instrument stack (Version 4), including an integrated lock-in amplifier, to control the STM and to affect the acquisitions. Additionally, the STM was equipped with a long-range microscope camera to assist in positioning the STM tip over the intended region of a sample (to within about several microns laterally). We used primarily open source software (WSXM [51] and Gwyddion [52]) to analyze SPM images during the course of this work.

A second UHV chamber was directly adjoined to the STM vacuum chamber to allow for sample preparation tasks to be carried out in UHV conditions. This chamber will be referred to as the “prep chamber” in this document. Specifically, this chamber housed a heating stage capable of thermally annealing samples (typically by resistive, or indirect heating) up to about 900 °C. We used this heating stage to degas samples in vacuum (~10^{-9} – 10^{-10} Torr) to help in preparing clean, stable surfaces suitable for STM imaging. This chamber was also equipped with an Ar ion sputtering source that was used in conjunction with the sample heating stage to prepare atomically-flat and clean Au(111) on mica samples for tip conditioning (described later in Section 2.3.2.2).

2.3.2.1 Preparation of the Tungsten STM Tip

We used an electrochemically-etched W tip for the STM work described in this document. The tip is one purchased from Bruker (product # DTT10), then mounted in a special tip holder for use in the Scienta-Omicron STM system described in Section 2.3.2. After loading the tip into the vacuum chamber, we heated the apex of the tip using the electron bombardment technique (described in Section 2.2.4) using the "tip prep tool" integrated into the STM vacuum chamber. To accomplish this, we set the filament current to 2.72 A to heat the filament and then applied a 1.0 kV accelerating voltage (relative to the STM tip holder). We then slowly inserted the tip into the apparatus until we measured 1.5 mA - 2.0 mA of current through the tip, indicating that the thermionically-emitted electrons from the filament were being absorbed into the tip. We also noted that the pressure in the STM chamber rose during this process, indicating that the tip was outgasing water vapor and the oxide layer. After holding the tip in this configuration for 10 seconds, we retracted the tip from the apparatus and loaded it into the STM scan head. Scanning electron microscope (SEM) images of a tip representative of the one used for this study are shown in Figure 2.8b-c. From these images, we estimate the apex radius of curvature of our STM tip to be about 100 nm.

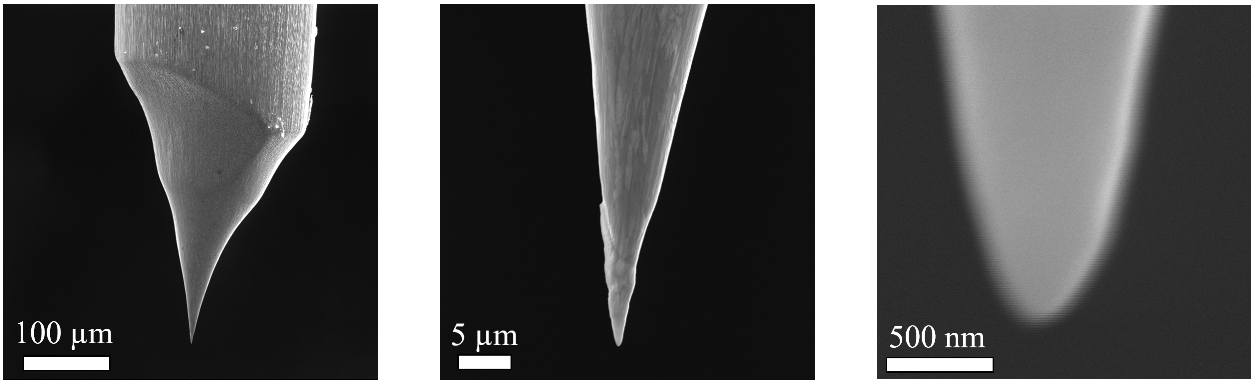

(a) SEM image with etched section visible.

(b) SEM image near the tip's apex.

(c) SEM image zoomed in on the tip's apex.

Figure 2.8: Scanning electron micrographs of a typical electrochemically-etched W tip.

2.3.2.2 Preparation of a Reconstructed Au(111) Sample

The first step to conditioning the STM tip was to prepare a reconstructed sample Au(111) on mica. To this end, we mounted a Au(111) on mica sample to a molybdenum STM sample plate, loaded it into the STM system's prep chamber, and then annealed it in a UHV heater stage to about 350 °C for about 30 minutes using the resistive (indirect) heater. At the end of the 30-minute annealing period (and after powering down the ion pump in the vacuum chamber), we positioned the sample (mounted in the heater stage) in the path of an Ar ion sputtering source in the prep chamber. We then applied a 2 kV accelerating voltage to the sputtering source and continuously flowed a small amount of Ar gas into the sputtering source using a leak valve. The sputtering source then ionized the Ar atoms and accelerated them toward the Au on mica sample (which was set to ground). We sputtered the Au surface in this way, maintaining an Ar ion current in the range of 10 μA - 20 μA (with the average being about 16 μA), for 1 minute and then closed the leak valve. Importantly, we ensured that the pressure in the prep chamber never rose above about $3 \cdot 10^{-5}$ Torr, thus avoiding corona discharges in the sputtering source due to high voltage. We then repeated this process twice, ending with a final annealing step that lasted about 45 minutes. After the final thermal anneal, we loaded the sample into the STM scan head, whereupon it cooled to 77 K by means of the liquid nitrogen cryostat.

2.3.2.3 Tip Conditioning

We conditioned the prepared STM tip using the clean, reconstructed Au(111) on mica sample. We generally made use of bias voltage pulsing, controlled tip-sample contact, and scanning with reduced tip-sample distances (and higher current) to condition the tip, as described in Section 2.2.5. Tip conditioning continued until we were able to repeatably acquire STM images of the Au(111) surface with well-resolved step edges and the herringbone reconstruction visible (images of which are shown in Figure 2.4). Additionally, the images needed to be largely free of tip-changes and other imaging artifacts (such as tip changes or multi-tip artifacts, which are signs of an unstable tip). We deemed the tip to be fit for STM imaging when these conditions were satisfied. However, we then assessed the suitability of the tip for performing spectroscopic measurements (as discussed in Section 2.2.5). We continued the conditioning process until we were able to acquire both high-quality STM images and STS spectra which demonstrated the expected density of states behavior (shown in Figure 2.5), before moving on to the planned experiments.

2.3.3 Switching Experiments

We used the voltage sweeping functionality integrated into the Nanonis hardware and software to affect the resistive switching and checking experiments. As discussed in Section 2.2.2, the positive polarity end of the voltage was applied to the sample (via the sample plate), while the negative polarity was applied to the STM tip. Before performing any switching experiments, we first imaged an area of the surface and positioned the STM tip over the location for a switching experiment. We then adjusted the current setpoint to 100 pA and the bias voltage to 1.0 V (corresponding to an effective tunneling resistance of 10 GΩ). This had the effect of adjusting the tip-sample separation distance (likely somewhere around 6 Å, see Section 2.2.2 for a discussion of this) to a consistent value. As discussed at the end of Section 2.2.2, the interpretation of the effective tunneling resistance corresponding to a consistent tip-sample separation distance assumes consistent LDOS of the sample and tip. In STM parlance, the process of setting the tip-sample distance is referred to as 'stabilizing' the tip. After the tip had been stabilized, the feedback system was locked, meaning that the piezoelectric drives controlling the vertical and lateral motions of the tip held the tip fixed in the same spot for the duration of the sweeping process. At the beginning of a switching experiment (after stabilizing the tip), we swept the bias voltage to the maximum positive value it would attain during the process (usually 4.0 V). We then swept the voltage down to the minimum value we wanted it to attain (either 0 V or - 4.0 V), recording the tunneling current as a function of applied voltage. Finally, we swept the voltage back to its starting point, also recording the current. This concludes the process of running a switching experiment. As such, the feedback system was restored, restabilizing the tip and preparing for subsequent imaging or additional switching experiments. Each switching experiment took a total of 2 seconds to complete. We specifically chose this sweep time to maximize the amount of settling and integration time at each point, while minimizing the effects of thermal drift. Another important note is that we switched the current preamplifier integrated into the STM system to work in low current gain mode to increase the maximum current level that could be recorded during the experiments.

2.4 Results and Discussion

We produced a model resistive switching element large enough to perform STM studies using the methods discussed above. An optical micrograph of the resulting RSE is shown in Figure 2.9a. Specifically, the region of the sample in which we performed our STM studies is outlined in this figure in black, which denotes the area covered by both graphene and monolayer MoS_2. The region outlined in red denotes one of the regions of monolayer MoS_2 coverage on the sample. A bounding box drawn to encompass most of the graphene-MoS_2 overlap area would be about 68 μm x 37 μm, indicating that the total sample area available is about 2500 μm^2.

The Raman spectroscopy data in the main plot of Figure 2.9b confirms the presence of graphene in the region comprising the model RSE. The data includes a set of material-specific peaks in the Raman spectrum that serve as “fingerprints” to identify the presence of graphene. This includes the *G* and *2D* peaks characteristic of graphene, centered at 1576 cm^{-1} and 2690 cm^{-1}, respectively. There are several points of note relating to these peaks. First, the intensity ratio of the *2D* peak to the *G* peak is approximately unity, which suggests that the interrogated graphene is few-layer rather than single layer (for which the expected intensity ratio would be about 2 or greater) [53, 54]. Second, the full width at half maximum (FWHM) of the *2D* peak in this Raman data is approximately 66 cm^{-1} rather than the 25 cm^{-1} expected of single layer

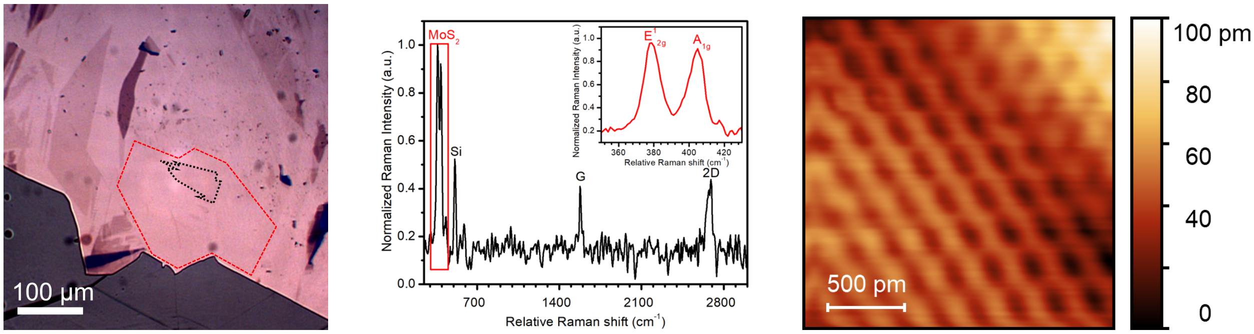

(a) Optical micrograph of model RSE. Red outlined region represents monolayer MoS_2 and the black area represents monolayer graphene.

(b) Raman spectrum acquired on the RSE. This spectrum utilized 532 nm laser excitation.

(c) STM image of the RSE showing the graphene lattice. Stabilization parameters for this image: I = 500 pA, V = 500 mV.

Figure 2.9: Initial characterizations of the model MoS_2-based RSE. Reprinted with permission from Springer Nature: Springer *MRS Advances*, [12], (“STM Tip-Induced Switching in Molybdenum Disulfide-Based Atomristors”, Thompson, J., et al.), © 2019.

graphene. This is also suggestive of few-layer graphene (about 4-5 layers) [55]. One might also expect to see a third peak, referred to as the *D* peak. This would be centered at around 1350 cm^{-1} and is activated by the presence of lattice defects (such as grain boundaries and vacancy defects) [53, 56]. We see in the main part of Figure 2.9b that the *D* peak is either absent or sufficiently weak that it is essentially indistinguishable from the background noise. This suggests that the graphene present in our model RSE is of high crystalline quality, as is expected from exfoliated graphene.

The Raman spectrum shown in Figure 2.9b contains a second set of characteristic peaks that indicate the presence of monolayer MoS_2. The relevant peaks are outlined by a red box in the main figure. The inset figure shows a higher resolution version of this region of the Raman spectrum. The two peaks present in this region, namely the E^1_{2g} peak at 378 cm^{-1} and the A_{1g} peak at 404 cm^{-1}, indicate the presence of MoS_2. However, both peaks are redshifted compared to their expected positions for MoS_2 exfoliated onto SiO_2/Si [57, 58]. Similar degrees of shifting have been observed previously in both exfoliated and CVD-grown monolayer samples and is attributed to a combination of effects caused by MoS_2-substrate coupling [59, 60]. The shifting of the E^1_{2g} and A_{1g} peaks is consistent with a tensile strain of about 1.2% induced in the MoS_2 by the Au substrate [61]. The fact that we see strain-induced redshifting of the MoS_2 characteristic peaks in our model RSE indicates that the MoS_2-Au interface is likely to be very nearly pristine. This is as one would expect, given that the sample was fabricated in such a way that no process polymers (e.g., PMMA) were ever introduced to either of the surfaces (MoS_2 or Au) which formed the interface. Additionally, the success of the Au-assisted exfoliation process used in the sample preparation process (which is critically dependent on interface cleanliness) suggests that the MoS_2-Au interface should be largely free of adventitious carbon and other atmospheric contaminants.

Our preliminary STM imaging of the model RSE confirms the atomically-clean nature of at least some portions of the sample, establishing the sample's suitability for further STM studies. We assessed the nanoscale cleanliness of the sample by imaging multiple regions on the surface of the sample using the STM. At least several of the regions we explored exhibited surface morphologies with height variations up to several tens of nanometers. Additionally, achieving stable STM imaging proved difficult in these regions. These two factors made it nearly impossible to acquire atomically-resolved STM images of the surface in these regions. Eventually, we found a region on the sample that was sufficiently clean as to yield stable, atomic resolution images of the graphene surface, as shown in Figure 2.9c. This image shows the graphene honeycomb lattice.

We performed the work done in our study in the first atomically clean region that we found, in an effort to preserve the cleanliness of the tip as much as possible. An STM heightmap image of this region is shown in Figure 2.10a. This image features an atomically-resolved graphene lattice, as evidenced by the honeycomb structure and several elevated regions. These elevated, elongated regions are likely due to subsurface graphene layers rolling up during the sample preparation process to form "scrolls". Nevertheless, the top layer of graphene seemed to be continuous, despite the scroll. STS spectra taken with the tip centered directly over and between graphene scrolls appear nearly identical, as shown in Figure 2.10b, indicating that the LDOS isn't significantly impacted by the presence of the scrolls.

The STS spectra shown in Figure 2.10b confirms that the graphene top layer is not in direct electrical contact with the Au substrate. The data shown in the main plot exhibits a small "gapped" region around the Fermi level (i.e., around a bias voltage of 0 V) in which the differential conductance (and therefore the sample's LDOS) is significantly suppressed. The gapped region extends from about -240 mV to about 356 mV (yielding a gap width of about 596 meV), with the measured signal level in this region corresponding to the noise floor of the data acquisition hardware. It is known that STM tunneling into graphene on SiO_2/Si substrates is a phonon-mediated process, and therefore that a small "phonon gap" would be expected in STS spectra of graphene directly contacting a metal electrode [62]. However, the gap that we observe in our data is significantly wider than the expected phonon gap (130 meV), suggesting that the observed gap is not due to phonon-mediated tunneling. This, in turn, suggests that our graphene is not directly contacting the Au substrate, and therefore any measured current must travel through the intervening MoS_2 layer. With this in mind, one might expect the gapped region to be much wider, reminiscent of the semiconducting bandgap of MoS_2 (about 1.9 eV for monolayer samples) [63]. However, it has been shown that thermal annealing of MoS_2 on Au leads to increased MoS_2-Au hybridization [64]. Such increased sample-substrate interaction effectively changes the character of the MoS_2 from semiconducting toward a more metallic (i.e. conducting) nature. In this way, the bandgap observed in STS spectra of annealed MoS_2 on Au samples can shrink to even several hundred meV or less, depending on the strength of the hybridization. Since the sample used in this study was thermally annealed to 450 °C, we expect at least partial hybridization to have occurred, and thus the small, but finite, gap we observed is consistent with the expected behavior of a sample prepared in the manner described above.

Figure 2.11a shows that we were able to switch the resistance state of the sample using the STM. In this case, we steadily swept the sample bias voltage from 0 V to 4 V and then back

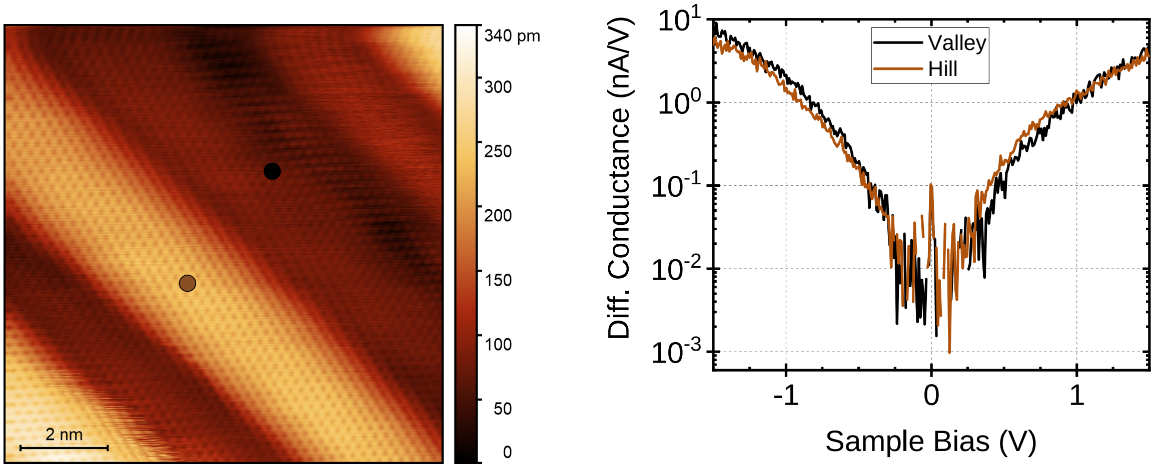

(a) Constant current STM image of the area where switching was performed. Stabilization parameters: V = 600 mV , I = 1.5 nA.

(b) Differential conductance spectra taken in different spots in the region of switching. Each curve's color correspond to the location shown at left as colored dots.

Figure 2.10: Pre-switching characterization of the RSE surface. Subfigure A: Reprinted with permission from Springer Nature: Springer *MRS Advances*, [12], ("STM Tip-Induced Switching in Molybdenum Disulfide-Based Atomristors", Thompson, J., et al.), © 2019.

to 0 V. The forward sweep (with increasing voltage, shown in dark gray) features several small jumps in current as the bias voltage was raised from 0 to about 1.75 V, followed by a more abrupt increase at about 2.1 V. We attribute the jumps in current to changing of the internal resistance of the sample. From about 2.1 V to the end of the forward sweep, the current plateaued at 333 nA, which corresponds to the compliance current limit of the current preamplifier in the STM's data acquisition hardware. During the reverse sweep (shown in red) the current exhibited a significant amount of hysteresis, remaining at the compliance level until about 0.6 V, whereafter it sharply fell back toward the origin. This hysteretic behavior is consistent with the expected behavior for a change in sample resistance, as probed by an STM tip that was held at a constant tip-sample separation distance.

As discussed in Section 2.2.7, we can use the IV curve data (shown in Figure 2.11) to

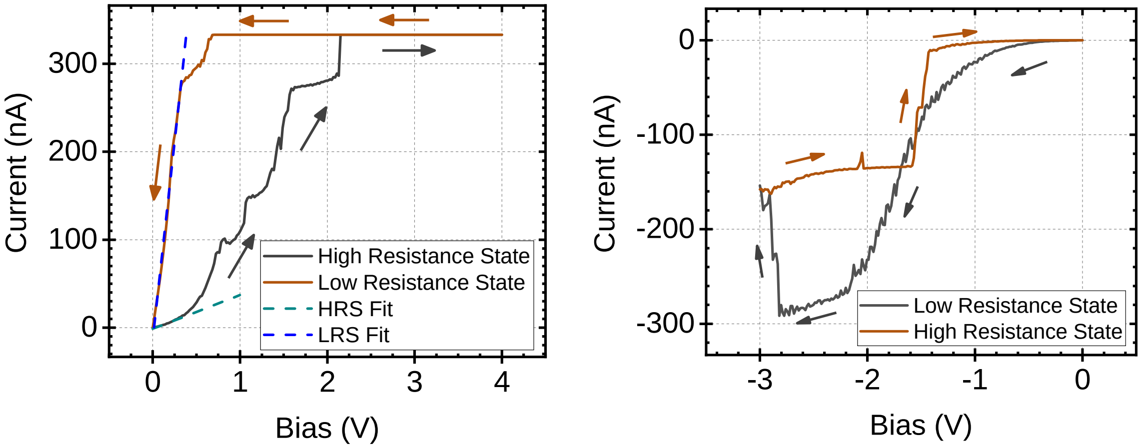

(a) Switch On

(b) Switch Off

Figure 2.11: IV curves from the first switching experiment. Arrows indicate the direction of the sweeps, and colors denote the resistance state of the sample. Dashed lines represent linear fits to the zero-bias data, from which the effective junction resistances were determined. Subfigure A: Adapted from: *MRS Advances*, [12], ("STM Tip-Induced Switching in Molybdenum Disulfide-Based Atomristors", Thompson, J., et al.), © 2019.

estimate the On-Off ratio of the sample. To do so, we consider the zero-bias behavior of the forward and reverse sweeps. There are two reasons to focus on the zero-bias (i.e. the very low-bias) rather than the high-bias regime. First, this is the region most representative of a pure quantum mechanical tunneling problem (as opposed to Fowler-Nordheim tunneling, *et cetera*), as discussed in Section 2.2.2, and is therefore the most straightforward to interpret. Second, we expect the resistive behavior of the sample to be stable only for very small biases, as applying higher biases would likely lead to changes in the resistive state and thus do not represent steady-state behavior. To begin the analysis, we perform a linear regression and use the reciprocal of the slope to estimate the observed resistance at very low biases for both the forward and reverse sweeps. The resistances obtained in this way represent the total resistance of the entire tunnel junction before and after the switching event. This yields $R_{junction,Off} = 31.1$ MΩ and $R_{junction,On} = 1.1$ MΩ. Substituting these values into Equation 2.7 gives an On-Off ratio greater than or equal to about 28.8.

We found that the resistance of the sample could be switched back to a higher state by performing a voltage sweep similar to the one described above, but in the negative direction. The IV curve data for this is shown in Figure 2.11b. During this process, the voltage was steadily swept to - 3.0 V with the same sweep speed used in the previous process. However, unlike before, the current never reached the compliance current of the preamplifier. Instead, at around -2.8 V, the current dropped suddenly. During the sweep back toward 0 V we see a similar drop in current at around -1.8 V. We attribute such sudden decreases in current to a lowering of the resistance state of the sample and is consistent with bipolar switching.

The STM images in Figure 2.12 show that the graphene surface remains intact and free of contaminants. This fact allows us to rule out the possibility that the observed changes in current seen in Figure 2.11 could have been due to materials being deposited from the tip onto the surface. Additionally, we note that subsequent imaging of this sample produced clearly-resolved images, suggesting that the shape and condition of the tip had not changed significantly from before the first switching attempt.

It is apparent from Figure 2.12b that a change in morphology of the sample did occur during the switching event discussed above. While one might be tempted to attribute the entirety of the observed change in sample resistance discussed above to such a change in morphology, we believe that this line of reasoning misses the mark. Certainly, there would be an attractive electrostatic force exerted between the tip and sample, such that the graphene layer could possibly be picked up from the surface of the sample (if enough work were done to exfoliate the top layer of graphene from sub-layers), coming in contact with the tip in the process. Indeed, tip-induced exfoliation of graphene from highly-ordered pyrolitic graphite samples has been observed by others in the field (as described in [65], for example), particularly when the graphite is freestanding (e.g., on a transmission electron microscope grid). However, to the best of our knowledge, all such reports of *in situ* lifting or exfoliation utilized graphene/graphite that was electrically shorted directly to the applied voltage source. In essence, this means that the graphene/graphite served as the STM

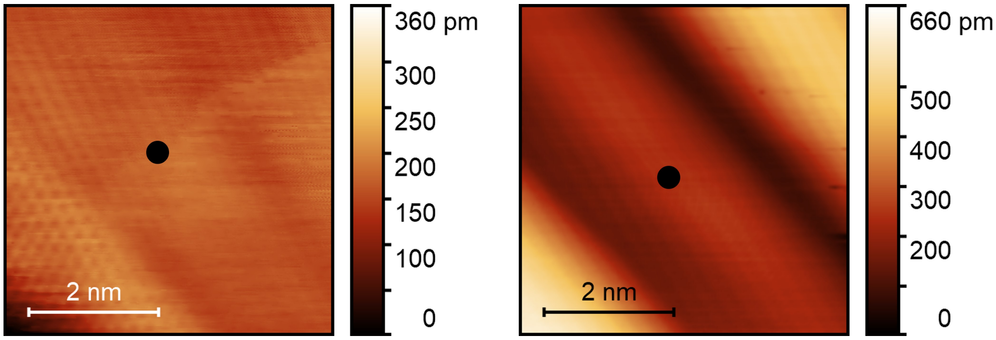

(a) Before switching, sample in the Off state. Stabilization parameters: V = 500 mV, I = 0.9 nA.

(b) After first switching, sample in the On state. Stabilization parameters: V = 500 mV, I = 1.0 nA.

Figure 2.12: Constant current STM images of the area where switching experiments were performed. Black dots signify the location of the center of the STM tip during switching. Reprinted with permission from Springer Nature: Springer *MRS Advances*, [12], ("STM Tip-Induced Switching in Molybdenum Disulfide-Based Atomristors", Thompson, J., et al.), © 2019.

tip's counter electrode directly. This differs from our arrangement, in which the graphene layer does not directly contact the source of the voltage (the Au layer in our sample, which is connected to the sample plate, etc.). This means that the graphene in our device was partially electrically screened by the MoS_2, and thus we expect the attractive force between the graphene and the STM tip to be reduced as a result. By performing an electrostatics calculation (detailed in Appendix B), we estimate that the graphene in our sample geometry would have experienced attractive forces smaller than the graphene in the aforementioned reports by a factor of about 7-10, and thus any lifting effects should be similarly less pronounced. Additionally, other reports of graphene lifting show that the area of effect is typically on the order of the lateral size of the STM tip (i.e. tens to hundreds of nanometers). The images shown in Figure 2.12 are inconsistent with such findings. Finally, the STM image shown in Figure 2.12b was taken after the first (positive) switching sweep, with no other sweeps having been done (specifically no negative sweeps). This means that, if the graphene had been significantly lifted off the sample, the large-scale lifting should have been evident, as there would have been no way for the graphene to relax back onto the sample's surface (the sample plate is mounted into the STM chamber upside down, so gravity would not assist in this case). With this in mind, we affirm that the changes in morphology of the sample could have contributed to the apparent switching behavior observed in Figure 2.11, but we believe there is insufficient evidence to suggest that the switching can be entirely explained by such changes.

We performed additional voltage sweeps to evaluate the reproducibility and endurance of the switching behavior after the first switching cycle. The evaluation process involved performing thirteen additional voltage sweeps in the same region as the first. Additionally, each sweep included first a positive polarity sweep (as in Figure 2.11a), but also included a negative polarity sweep immediately following the positive portion (as in Figure 2.11b). These sweeps featured pinched hysteresis loops, as expected for resistive switching devices. However, the exact character of the hysteresis loops varied over the course of the evaluation process. Figure 2.13a shows a representative sampling of the variations we observed during this process. Some aspects of this data are similar to the first sweep. For example, the average threshold voltage for switching to a lower resistance state (determined as the voltage at which the tunneling current reached the preamplifier's compliance limit of 333 nA) was 2.48 V ± 0.30 V for these sweeps, as opposed to about 2.1 V for the first sweep. On a related note, the threshold voltage for switching back into the high resistance state was -2.46 V ± 0.37 V. However, some aspects of the hysteretic effects differ from those observed in the first switch. Specifically, the voltage range over which the measured current remained at the 333 nA compliance level of the preamplifier is significantly smaller than it was during the first sweep. The lower portion of Figure 2.13b shows the On-Off ratio, calculated from the zero-bias junction resistances as discussed above, as a function of sweep index. The data displays a general trend toward lower On-Off ratios as more sweeps were performed, with the ratio roughly stabilizing to a value of approximately 2 by the end of the evaluation process (except for two outliers). The zero-bias junction resistances obtained for these sweeps using the fitting technique discussed above are shown in the upper part of Figure 2.13b.

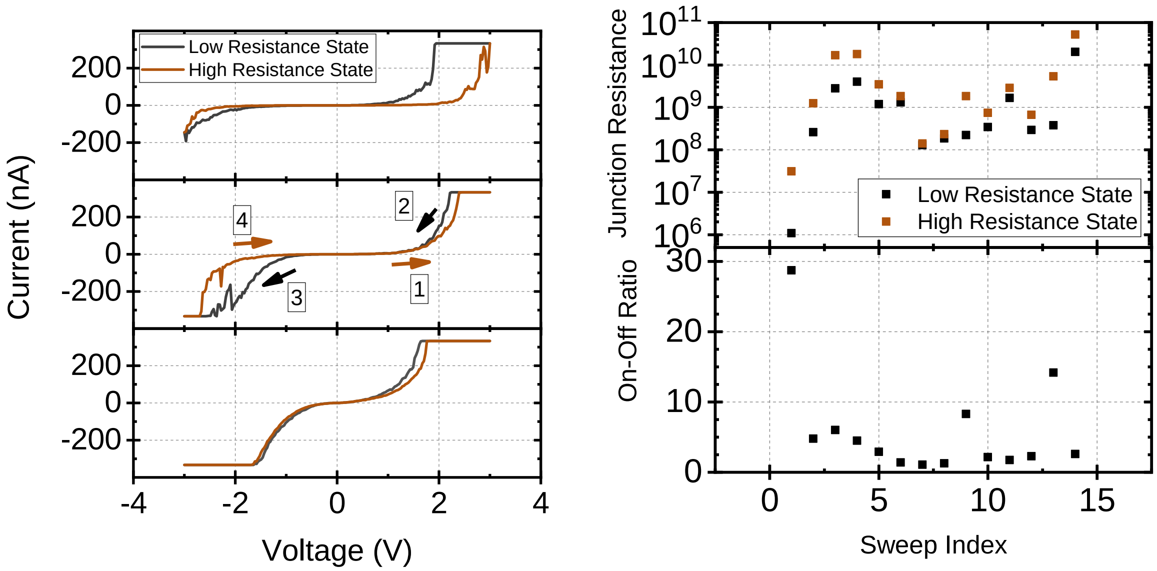

(a) IV curves from subsequent switching events.

(b) On-Off ratio for subsequent switching events.

Figure 2.13: Data for subsequent switching events.

The switching data collected over the course of this experiment shows that, while the switching behavior persisted over multiple switching attempts, there was significant variation from sweep to sweep. It is possible that changes in surface morphology could have contributed to this variation. However, as before, we assert that morphological changes alone are insufficient to fully explain the observed behavior for several reasons. Our reasoning for this is that both attractive and repulsive forces would have been required to affect the surface morphology in such that the tunnel junction resistance could both increase and decrease (during a switch off and a switch on event, respectively). However, it is unlikely that repulsive forces would have played a role in our switching experiments. This is because any tip-sample forces participating in these voltage sweeps would be due to either van der Waals or electrostatic interactions. While both of these interactions can, in principle, cause a repulsive force, they could not have done so here. Exertion of a repulsive force from a van der Waals interaction would require the tip to have approached the sample by at least several Angstroms to access the repulsive regime of the interaction. This did not happen, as the tip was held in place during voltage sweeps. On the other hand, a repulsive electrostatic force would require that the charges induced on the sample's surface (by application of a voltage) be of the same polarity as those accumulating on the tip. However, we know from electrostatics that the charges induced on the sample would be of opposite polarity to those on the tip, so the interaction would be purely attractive.

Determination of the resistive switching mechanism at play in this model RSE from the data shown above is complicated by the non-contact nature of the measurement process. In a typical resistive switching scheme, the metal contacts would be in direct physical contact with the semiconducting layer. This would allow one to fit various mathematical models to the IV curve data and make a judgement about the dominant conduction mechanism or mechanisms contributing to the observed current. This, in turn, could provide information about the physical factors which dictate the switching behavior (e.g., to determine if the switching is filamentary or interfacial). In principle, similar fitting procedures could be applied to our data to make similar determinations. However, due to the fact that our measured data is a convolution of at least two conduction mechanisms (i.e., tunneling from tip to sample and traveling through the sample), doing so would require a more sophisticated model than the one we employed thus far. At this point, it is worth mentioning that, in the time between when the work described so far in this chapter was published and the time of writing this dissertation, a journal article authored by Hus *et al.* was published regarding an experiment similar to the one described herein [66]. This study also utilized an STM tip to probe switching behavior in MoS_2, but their sample consisted of only MoS_2 on Au, lacking the graphene top layer. As a result, they were able to directly visualize the atomic structure of the MoS_2 and to discern the presence of structural defects in the lattice. Despite the differences in sample composition, they observed switching behavior similar to that which we had previously observed (and which is shown in Figures 2.11 and 2.13). Interestingly, they determined that the switching behavior they observed was due to migration of Au atoms from the substrate into sulfur vacancy sites (namely sulfur di-vacancies), providing a sort of pointlike filament for current to flow through. These observations, coupled with the similarity of their results to our own, suggest that the switching mechanism at work in our RSE is likely also due to the controlled substitutional doping of Au atoms into sulfur vacancies in the MoS_2 layer.

2.5 Concluding Thoughts and Opportunities for Future Work

The work described above shows that it is possible to use an STM to probe the device behavior of a resistive switching element at extremely small length scales. Additionally, it is possible to do so in a non-destructive manner (using the non-contact technique discussed above) and without the need for lithographic fabrication processes, which could have difficulty achieving such small device areas for more typical testing methods without the use of state-of-the-art techniques not commonly available in most fabrication facilities at the time of writing. In principle, an STM could be used in the manner discussed above to achieve very fine control over the spatial distribution of resistance states of a sample or device, which could be useful for “writing” nanometer-scale logic elements. However, the low throughput of STM and stringent sample preparation process would limit the practical applicability of this technique and would therefore likely preclude any industrial scale application of such. With this in mind, the real benefit of the technique described herein is its ability to probe nanometer-scale device behavior while simultaneously discerning morphological and quantum mechanical changes in the device. This, in turn, would provide feedback on switching mechanisms and factors that affect the stability and robustness of switching behavior in a variety of candidate materials. Such feedback is expected to prove useful for providing critical information needed to bring various nascent technologies to the point of commercial and industrial relevance.

There are at least a few ways that the work described above could be iterated upon to yield even more metrological and analytic power. First, the analysis of data acquired during switching experiments would benefit from development of a more sophisticated model for the conductive behavior of the tunnel junction and sample. Work in this vein would likely be able to reveal additional information about the primary conduction mechanism at play in the sample. Performing STM imaging over larger length scales, as well as low-bias STS, both before and after switching experiments could yield important information about the spatial extent of switching. In fact, STM is uniquely suited to perform this task as, by its very nature, it acquires spatial maps which represent the convolution of morphological and electronic properties. Additionally, while the work by Hus *et al.* provides valuable insight into changes in resistance of a MoS_2 monolayer alone, it is likely that the electrodes themselves play an important role in determining the overall character of the switching behavior of resistive switching devices. Thus, it would likely be fruitful to perform studies comparable to those described herein and in [66] in such a way that the switching behavior can be interrogated both with and without a top electrode in the same region. One possible way to do this could be to leverage the attractive forces exerted by the tip (discussed throughout this chapter) to fold and unfold a monolayer graphene sheet in a selected area of the sample. Another interesting avenue for exploration is to more quantitatively determine the role of structural defects in controlling the switching behavior. For example, it could be possible to increase the On-Off ratio of a switching device if the switching area had a higher density of sulfur vacancies (di-vacancy or otherwise), or possibly even engineer the material so that it could host multiple resistance states (rather than being strictly a two-level system). Systematic thermal annealing could be used to create defects in a TMD-on-Au sample. However, STM is also capable of atomic manipulation, so the local density and type of defects could be deterministically tailored to suit an experimenter's whim without resorting to macroscopic manipulations such as thermal annealing.

Finally, a series of hybrid switching experiments could be performed in the Omicron STM system. In such experiments, a thin top electrode such as graphene would be included in the RSE device to be tested. However, the top electrode would be connected to an external voltage source while being isolated from the sample plate (and therefore from contacting the Au substrate directly). In this way, two types of switching experiments could be performed in the STM chamber. The first is the kind described in this chapter, in which the STM tip serves as the top electrode. The second, however, would be the more common switching experiments that an RSE would normally be used for, in which the voltage signals are applied directly to the contacts on the sample rather than remotely via the STM tip. These two types of switching experiments, when combined with STM imaging, could provide detailed information regarding the spatial extent of low-resistance regions induced in the sample. This would be possibly primarily due to the convolution of morphological and electronic features in images produced by STMs.

CHAPTER 3: TOWARD SOLAR-BLIND THIN FILM HEXAGONAL BORON NITRIDE-BASED PHOTODETECTORS FOR ULTRAVIOLET SENSING - PART 1

3.1 Introduction

Ultraviolet (UV) light remains comparatively underutilized in device applications, as it is generally considered to be harmful to humans (e.g., causing sunburns). Fortunately, most of the UV light from the solar radiance impinging on the earth is absorbed by ozone molecules in the stratosphere [68, 69]. This includes all the light with wavelengths between 200 nm and 280 nm (UVC) and most in the range of 280 nm - 315 nm (UVB). The absence of UVC light near the surface of the Earth enables UV photodetectors to be used in several important terrestrial applications. First, fluctuations in the density of ozone in the stratosphere can be monitored by measuring local variations in the amount of UVC light detected at the surface of the Earth [70–72]. Second, changes in UVB and UVC light can be used in flame detection systems to aid in the early detection of forest fires, for example [73–75]. Finally, UV-based prototype non-line-of-sight communication systems have been developed for possible use in defense applications [76]. In addition to terrestrial applications, image sensors capable of detecting light in the UV range are desirable for developing space-based telescopes capable of performing UV astronomy.

Despite the applications discussed above, UV photodetectors remain largely underutilized. The primary reason for this is that many UV detectors have historically been made from materials

---

Note: This chapter includes figures adapted from those originally published by Thompson, J. (the author of this dissertation), *et al.*, in the *MRS Advances*, volume 5, number 37 in 2020. A complete citation to this article can be found in the LIST OF REFERENCES: [67]. These figures have been adapted with permission from Springer Nature (see Appendix A for copyright release notice). Figures reproduced herein bear specific notice of permission for reuse in the appropriate figure captions.

with relatively small band gaps, such as Si (with a band gap of 1.12 eV). In particular, this has hindered the wavelength-specificity of such detector devices, as longer wavelengths (from outside the UV range) possesses sufficient energy to create a photoresponse in such detectors. This means that bare detectors suffered from poor signal-to-noise performance due to the presence of significant amounts of background signal (especially from ambient visible light) and relatively weak UV signals to be detected. This issue can be remedied by fitting the detector with an optical bandpass filter, but this adds extra cost, complexity, and bulk to the detector, and likely further diminishes an already relatively weak signal.

Development of UV detectors that are insensitive to longer wavelength light would contribute significantly to solving the signal-to-noise issue. Such detectors are termed "visible blind" if they are inherently insensitive to visible light, and "solar blind" if they are insensitive to the entire portion of the solar irradiance outside the UV range, without the use of band pass filters. A promising avenue for developing such detectors involves utilizing wide band gap (WBG) semiconductors as the absorbing material in the detector. Such WBG semiconductors should have a band gap energy that is slightly lower than the photon energy of the longest wavelength light to be detected, but greater than that of any light to be rejected. The key advantage this imparts is that electron-hole pairs will not be generated in the absorbing layer, and therefore no photoresponse will be generated (at least not by the internal photoelectric effect). Multiple prototype solar blind UV photodetectors have been developed [77–82]. For example, many have utilized oxides (such as gallium oxide) as the WBG semiconducting material. While such detectors have demonstrated solar blind UV detection, achieving response times of much less than one second remains challenging for some device designs, likely due charge-trapping effects [83]. Additionally, it has been challenging to fabricate high-quality p-type semiconducting layers, which is problematic, as these devices usually rely on p-n junctions to function.

Layered WBG semiconductors offer another potential solution to achieve solar blind UV photodetector devices. Of these, hexagonal boron nitride (hBN) is particularly desirable for such applications, as it has a band gap in the range of 5.5 eV - 6.07 eV [84–88]. Additionally, the absorption coefficient of hBN in the ultraviolet range is higher (up to about $5 \cdot 10^5 cm^{-1}$) [87], than other wide band gap semiconductors, for example, Ga_2O_3 (which has an absorption coefficient of around $1 \cdot 10^5 cm^{-1}$) [89]. This means that films of hBN can be thinner than those of other wide band gap semiconductors while still absorbing a similar amount of light. These qualities indicate that hBN is well-suited for integration into solar-blind UV photodetectors, despite the fact that it is an indirect band gap material [84]. Additionally, these factors suggest that such detectors could potentially feature dark currents on the order of less than 1 pA and a cutoff wavelength of about 225 nm, while offering similar or better optical response than those made from other materials, making them highly competitive with other state-of-the-art technologies [90].

Similar to MoS_2, ultra-thin (2D) hBN films can be prepared by a variety of methods, including mechanical exfoliation [91, 92], solution processing [93–95], or CVD [88, 96–98]. hBN also has excellent thermal stability [99], chemical stability in harsh environments [100, 101], high in-plane thermal conductivity [102, 103], high dielectric strength [104–107], and is generally chemically inert [4, 100]. These qualities make hBN materially-advantageous for integration into UV photodetector devices for use in harsh environments. Indeed, there has been some work toward implementing thin film-based UV detectors utilizing hBN.

hBN-based UV photodetector devices have been fabricated using a variety of material deposition techniques, including high temperature sputtering [108], mechanical exfoliation [109], and pulsed laser deposition of hBN nanosheets [110, 111]. These devices have demonstrated that they are sensitive to light in the UV range, but they are all based on a lateral design. This means that the hBN absorbing layer runs parallel to the surface of the substrate. Lateral designs are not ideal for creating densely-packed detector arrays, as their metal contacts or other on-chip connections typically occupy a significant amount of space around the absorbing layer. Most importantly, however, is the fact that some active area of the absorber itself must generally be sacrificed to enable electrical contacts to be made, as contacts are typically deposited atop the absorber itself. This effectively leads to a trade-off between having compact devices, generally sacrificing signal-to-noise performance, or having larger-area devices that are highly responsive, but sacrificing packing density. While such designs are suitable for single-pixel light detectors, their laterally-extended nature is not ideal for fabricating multi-pixel arrays, as would be used in a UV sensitive camera, for example.

In this work, we describe efforts to fabricate an hBN-based UV photodetector which features a vertical device design. Vertical designs are expected to simultaneously allow for a greater degree of area-scaling without necessarily sacrificing the signal detection performance. The key feature that severely limits the performance tradeoffs discussed in the previous paragraph is that, in our vertical device design, the entire hBN absorbing layer is flanked above and below by the electrodes. In this way, extremely thin layers of hBN can be used, conferring the benefit of vertical compactness and reducing the ‘width’ of the Schottky or tunneling barrier to a sufficient extent that one could, in principle, hope to achieve measurable device responses at reasonably low operating voltages. To facilitate this design, we chose to use graphene as the electrode material. There are several reasons for making this design choice. First, graphene is largely transparent, with monolayer samples exhibiting greater than 97 % transparency throughout the visible and near-infrared wavelength ranges [112, 113]. Additionally, graphene affords an opportunity to extend the range of operation of an hBN-based detector to wavelengths somewhat above what the band gap of hBN would allow (longer than about 225 nm). This is because $\pi - \pi^*$ intra-band transitions result in an exciton-related peak in the absorbance of graphene centered at 4.62 eV (268 nm) and extending from about 3.5 eV to 5.1 eV (243 nm - 354 nm) [113, 114]. Thus, the inclusion of graphene in vertical devices serves not only as a transparent top electrode (in the visible and infrared ranges, preserving the solar blindness of the device), but also as an optically active layer enabling detection of wavelengths over a broader range of wavelengths in the UV.

3.2 Background

3.2.1 Basic Energy Band Theory

All crystalline material is composed of one or more type of atom arranged in a repeating, geometric arrangement called a lattice. The nuclei comprising such a lattice are positively charged and form a repeating pattern of potential wells in the material, called a lattice potential. The quantum mechanical state of any non-bonding electrons in the material depends, therefore, on the periodic arrangement of potentials. Whereas the energy states that an electron can occupy in isolated atoms are discrete, the energy states in a crystal become smeared out as a result of the lattice potential, forming essentially continuous bands of allowable energy states. The lower-energy band is referred to as the valence band, while the higher-energy is called the conduction band. Depending on the type or types of atoms comprising the material, a certain number of electrons will exist in the material at equilibrium. These electrons will start filling the electronic bands from the lowest energy state, proceeding to fill higher energy states. The probability that a specific energy level will be filled by an electron is given by the Fermi-Dirac distribution:

$$f_{FD}(\varepsilon) = \frac{1}{e^{\beta(\varepsilon - E_F)} + 1} \quad . \tag{3.1}$$

In the above equation, f_{FD} represents the probability for a state with energy ε to be occupied by a fermion. Additionally, $\beta \equiv k_B T$, where k_B is Boltzmann's constant and T is the temperature of the material in question. For a (theoretical) sample at absolute zero (0 K), the highest energy level with an occupation probability of 1 is called the Fermi energy, or the chemical potential, in statistical physics parlance. For a sample at a finite temperature, there is a chance that some electrons near the Fermi energy (now called the Fermi level, E_F) can be thermally excited to higher energy levels above the Fermi level. This is shown schematically in Figure 3.1. It is worth noting that having an occupation probability of 1 does not guarantee that an electron will occupy a specific energy level.

This is because there must be an available state at the energy level in question for an electron to actually occupy the energy level, which is not always the case. The number of available states as a function of energy is called the “density of states” (DOS).

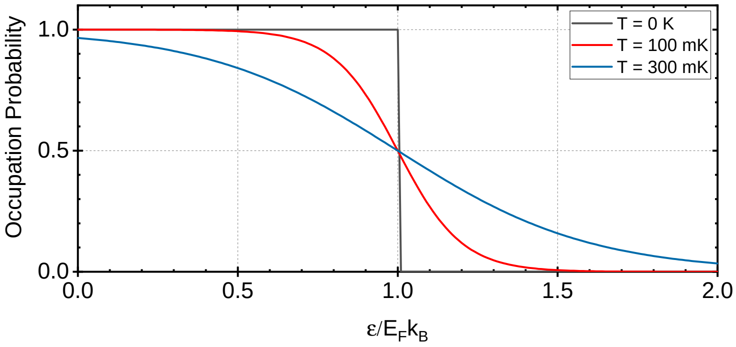

Figure 3.1: Plot showing the Fermi-Dirac distribution

The electronic behavior of a material is dependent on the details of its energy bands. In metals, the conduction and valence bands overlap, whereas in insulators (including semiconductors), the two bands are separated by an energy band gap (E_g) in which there are no allowable energy states for an electron to occupy (shown schematically in Figure 3.2a). The high conductivity of a metal stems from the fact that the Fermi level in a metal at finite temperature usually overlaps with the conduction band, leading to significant occupation of conduction band states. Since conduction band electrons are free to move around inside the material, they enable current to flow. In an insulator or semiconductor, however, the Fermi level resides in the band gap. This means that semiconductors and insulators have comparatively few (or no) conduction electrons and therefore have high resistance.

While we have discussed that the electron energy states in a crystalline solid smear to form an essentially continuous band, this is not quite the whole picture. There are generally sub-bands that make up the conduction and valence bands, each contributing their own density of states. The DOS of such bands depend not only on the energy of an electron which might occupy the state, but also the momentum of the electron (denotes as k). The band gap of a material is usually calculated as the smallest energy difference between a sub-band in the valence band and another in the conduction band.

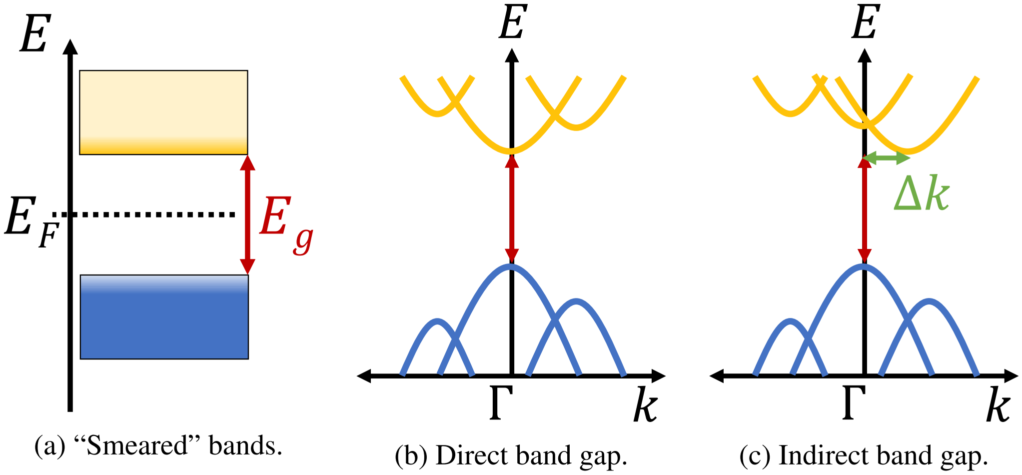

(a) “Smeared” bands. (b) Direct band gap. (c) Indirect band gap.

Figure 3.2: Schematics showing the energy band gap for a semiconductor or insulator. Blue shapes denote the valence band, while yellow represents the conduction band.

3.2.2 A Brief Discussion of Light-Matter Interactions

As discussed above, this chapter is devoted to discussing work done to design, implement, and test ultraviolet photodetector devices. As such, a discussion of relevant light-matter interactions will help to establish a theoretical foundation upon which further discussion can rest. With this in mind, the goal of this section is to provide an overview of such concepts. However, we acknowledge that light-matter interaction phenomena are complicated and diverse in nature, and cannot (and will not) be treated in their entirety in this section.

We are concerned with photon-electron interactions, as these are primarily responsible for the functioning of semiconductor-based photodetector devices. In particular, when a photon with energy equal to or greater than the band gap of a semiconductor or insulator is absorbed by the material it is possible for an electron at or near the top of the valence band to be excited to an energy state in the conduction band, leaving behind a hole in the valence band. Depending on the electron and hole mobilities of the material, the charge carriers can travel through the material under the influence of an external electric field and possibly be measured as current, until the electron or hole recombines with its counterpart. Charge carriers generated by photo-excitation are called “photo-carriers” and the resulting current is a “photocurrent”. There are two notes to make on this subject.

While photon energy is an important factor determining whether a photon will be able to generate an electron-hole pair, momentum is another important consideration. Electron excitation (at least as discussed in this work) requires that momentum be conserved as well as energy. There are two options to ensure that momentum is conserved during a photo-excitation event. The first involves the electron in question transitioning to a state in the conduction band with the same momentum as the initial state. When the smallest energy gap occurs between two sub-bands whose extrema occur at the same momentum, the band gap is said to be direct (shown schematically in Figure 3.2b). When the closest sub-bands occur at different momenta, the band gap is said to be indirect (Figure 3.2c). Thus, in order for an electron to be excited from the valence to the conduction band, either the final state must have the same momentum as the initial state, or an absorbed photon (or a phonon in the material) must provide the correct amount of momentum to the transitioning electron to reach the final state.

3.2.3 Basic Optical Spectroscopy Theory

Optical spectroscopic techniques are useful tools for measuring some optical behaviors of various materials. In the simplest terms, optical spectroscopy involves shining light on a material, letting the light interact with the material, and measuring either the reflected or transmitted optical power as a function of wavelength. Generally, spectra produced in this manner will be either transmittance or reflectance spectra. A transmittance spectrum gives the fraction of incident light, as a function of wavelength, that has been transmitted through the sample. Reflectance spectra are similar, but for light that has been reflected from the sample. These can be calculated from intensity data using the following equations:

$$R(\lambda) = \frac{I_r(\lambda)}{I_0(\lambda)} \quad , \quad T(\lambda) = \frac{I_t(\lambda)}{I_0(\lambda)} \quad , \tag{3.2}$$

where I denotes a measured intensity, subscripts 0, r, and t denote the incident, reflected, and transmitted portions, R the reflectance, T the transmittance and λ the wavelength of light. A third type of spectrum could be produced. This is called absorptance (A) and represents the portion of light absorbed by the material. Absorptance cannot generally be measured directly in a spectrometer. In principle, it could be calculated using conservation of energy, which in this case states that all the light incident on a sample must be reflected, transmitted, or absorbed:

$$1 = T + R + A \quad . \tag{3.3}$$

However, this is problematic for many spectroscopy experiments, in which only the transmittance is measured. Instead, a different approach is employed to determine the absorption characteristics of a sample. This approach involves calculating the absorption coefficient, which represents the degree to which a material absorbs incident light per unit length [115]. For non-reflective samples, the absorption coefficient is calculated using Lambert's law, which states that the intensity of light transmitted through a homogeneous medium decays exponentially with the path length of the light through the medium:

$$I_t(\ell) = I_0 e^{-\alpha\ell} \quad . \tag{3.4}$$

In this equation, α is the absorption coefficient of the medium and ℓ is the path length through the medium. Solving this equation for the absorption coefficient gives

$$\alpha = -\frac{1}{\ell} ln\left(\frac{I_t}{I_0}\right) = -\frac{ln(T)}{\ell} \quad . \tag{3.5}$$

The absorption coefficient is also a wavelength-dependent quantity. For completeness, we note that discussions involving the use of ultraviolet-visible spectroscopy to characterize the absorption characteristics usually make reference to another quantity, called the “absorbance”. This confusingly-named quantity is distinct from the absorptance (A) discussed above (despite sounding very similar) and is simply given by $\mathscr{A} = -ln(T)$. It is common for some spectrometers to allow a user to “measure” the absorbance spectrum of a sample, but the spectrometer is actually measuring the transmittance and performing the math for the user internally to produce the spectrum.

3.2.4 Determination of Optical Energy Band Gaps in Semiconductors

Optical spectroscopy can be used to experimentally determine the energy band gap of a semiconductor or insulator. In this section, we will discuss specifically a method to perform this task using ultraviolet-visible spectroscopy, even though other techniques (such as photolumninescence) can also be used. This method requires that one has an absorption coefficient spectrum for the semiconductor or insulator in question (determined as described at the end of Section 3.2.3). Additionally, the spectrum must include data at photon energies (wavelengths) that are equal to or greater than the material’s expected band gap. The essence of this analysis is Tauc’s relation:

$$(\alpha h\nu)^{1/n} = \beta\left(h\nu - E_g\right) \quad , \tag{3.6}$$

where $h\nu$ is the energy of a photon, α and E_g are again the absorption coefficient and band gap energy, and β is a constant. In this equation, n is equal to either $1/2$ if the material in question is a direct band gap material, or 2 if it has an indirect band gap [116]. The first step to determining the band gap of the material is to plot the left-hand side of Tauc's relation (with the appropriate value of n) vs photon energy (this is called a Tauc plot). Under ideal conditions, such a plot would contain a single peak centered somewhat above the expected band gap energy and constant for energies below the band gap. This peak, corresponding to the absorption band of the material, should have an approximately linear section occurring part way between the base and the apex. In principle, the band gap energy corresponds to the onset of the absorption band. However, there are multiple ways that one could quantify the onset, with the most common method proceeding as follows. A linear fit is made to the approximately linear portion of the low-energy band edge (i.e., the lower-energy side of the peak). From Tauc's relation, the slope of the fitted line will be β and the y-intercept will be $b \equiv -\beta E_g$. Graphically, the band gap energy is then the x-intercept of the linear fit (shown schematically in Figure 3.3). Numerically, the band gap energy can be determined from the slope and y-intercept as

$$E_g = \frac{-b}{\beta} \quad . \tag{3.7}$$

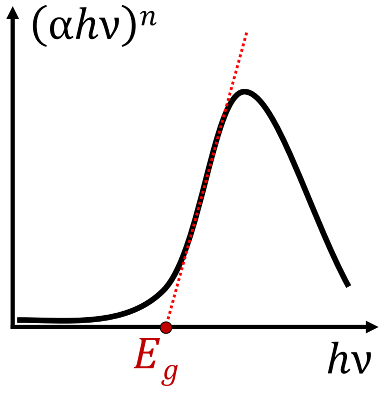

Figure 3.3: Schematic representation of a Tauc plot, with a linear fit to the low-energy absorption band edge.

3.2.5 Photoconductivity Measurements

There are at least two types of photodetectors that are relevant to the discussion of this chapter. The first type of device is a photoconductive detector. The working principle of a photoconductive detector is that incident light reaching the detector generates electron-hole pairs in the active material (generally a semiconductor, but hBN in this work). The photo-generated charge carriers (i.e., photo-carriers) effectively contribute to the total number of mobile charge carriers in the material. In a photoconductivity-based device measurement, when a voltage is applied across such a device, a current can be measured. This current will have two components. The first component is due to the equilibrium charge carriers intrinsic to the material. Since such a current is present even without exposing the device to light, it is commonly called a "dark current", and essentially forms a background. The second component is due to the photo-carriers and is therefore called "photocurrent". Thus, operating a detector in photoconductive mode typically involves applying a known voltage across the device and measuring the photocurrent generated by incident light. The measurement circuit for a photoconductive device can be relatively simple. In principle, one only needs to connect a voltage source and an ammeter in series with the photodetector device, creating a closed circuit. Depending on the design and composition of the detector, the photocurrent can be quite small for incident light in some wavelength ranges, sometimes even on the order of nanoamperes to picoamperes. For detectors and applications where the photocurrent is small, it may be necessary to use a current amplifier (such as a transimpedance amplifier) to measure the signal rather than a normal ammeter. Such measurements can be particularly challenging when the dark current or the noise level of the detector is significantly higher than the photocurrent.

The second type of detector operates in a photovoltaic rather than photoconductive mode. The operation of photovoltaic devices also depends on the generation of photo-carriers due to incident light. However, no external voltage is applied to the device and the measurement circuit typically involves an open-circuit. In principle, this means that photo-carriers can accumulate on the contacts of the device. The accumulation of charge (with one polarity on each electrode) will set up a potential difference between the contacts. When this happens, one need only use a voltmeter to measure the established potential difference. Such a measured potential difference is called an open-circuit photovoltage.

Carrier recombination is an important process which, in part, determines the operating efficiency of a photodetector. As discussed above, when a photon is absorbed by a photodetector, an electron-hole pair is created in the material. The photo-generated electron and hole can behave in several ways after photon absorption. The first behavior is to remain separate from each other. This is the ideal case for a photodetector, as the photo-generated electron and hole must remain separate in order to be measured as photocurrent or photovoltage. Diode-based photodetectors accomplish charge separation by utilizing the electric field present in the depletion region of a p-n junction, which pushes electrons generated in the depletion regions in one direction and holes in the other. Conversely, the Coulomb interaction will draw the two oppositely-charged particles toward each other (or toward other oppositely-charged particles). If an electron and hole get too close, there is a chance that the two will recombine (either radiatively or non-radiatively), become neutral again, and thus not contribute to a photoresponse. Electron-hole pairs can demonstrate other behaviors, such as forming excitons (an electron-hole pair in which each particle orbits each other for a time before recombining) or a trion (either two electrons and one hole, or vice versa). Since excitons are charge-neutral, they cannot themselves contribute to an electrical photo-response. However, trions can contribute, in principle, as they carry a net charge (depending on the combination of particles involved). Regardless, a photo-carrier must make its way to a contact and be measured by the external equipment before it recombines (i.e., during the “lifetime” of the carrier) for it to contribute to the photo-response of the detector.

3.3 Methods

3.3.1 Sample Preparation

The sample fabrication process for this project involved putting together multiple material components to form the final device. Below are descriptions of each of the processes used to fabricate and assemble each of the constituent parts, and a schematic of the device design is shown in Figure 3.4.

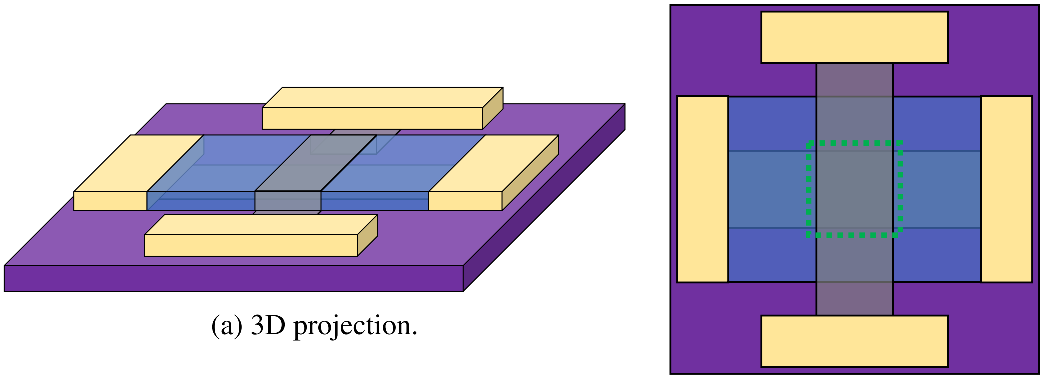

(a) 3D projection.

(b) Overhead view of device.

Figure 3.4: Schematics showing the construction of the prototype CVD hBN-based vertical ultraviolet photodetector discussed in this chapter. The green dashed region shows the active area of the device. Subfigure B: Reprinted with permission from Springer Nature: Springer *MRS Advances*, [67], ("Solar-Blind Ultraviolet Photodetectors Based on Vertical Graphene-Hexagonal Boron Nitride Heterostructures", Thompson, J., et al.), © 2020.

3.3.1.1 CVD Graphene Growth

Graphene sheets served as the electrode material for our vertical hBN-based UV photodetector device. The graphene sheets used in this project were polycrystalline, monolayer samples grown by chemical vapor deposition (CVD). The CVD growth process began by first cleaning a 250 μm thick polycrystalline copper (Cu) foil. In order to remove adventitious carbon from the surface of this foil, and to present a cleaner surface, we sequentially sonicated the foil in acetone, isopropanol, and water for 5 minutes each before blow-drying with dry nitrogen. Since Cu tarnishes easily when exposed to atmospheric conditions, we also removed the surface layers of the foil by immersing it in a 20% acetic acid aqueous solution for five minutes, followed by 5-minute immersions in two separate DI water baths to rinse away any residual acid. In this way, a mostly pristine surface was exposed for further processing. We then loaded the cleaned foil into a quartz tube placed inside a tube furnace. This was followed by sealing and evacuating the tube using a mechanical vacuum pump until it reached a base pressure of approximately 30 microns (i.e., 30 microns of mercury). This was done to remove any residual atmospheric gases from the system. Next, we flushed the gas delivery system through the tube for 10 minutes with 10 sccm of hydrogen and 20 sccm of methane gases, using mass flow controllers to regulate the flow rates. Following the flushing process, we turned off the gas flow through the tube, returning it to its base pressure. Then we ramped the temperature of the furnace to a final temperature of 970 °C over the course of one hour. When the temperature had stabilized, we flowed 2 sccm of hydrogen gas and 20 sccm of methane through the tube. During this process, any methane molecules impinging on the surface of the Cu foil would have been pyrolized, nucleating onto the surface of the copper and possibly being dissolved into the foil itself [117–120]. After a growth period of 15 minutes, we removed the copper foil from the hot zone of the furnace by sliding the furnace along the length of the tube using a dedicated rail system. This caused the sample to rapidly cool. During the cooling process, it is believed that the dissolved carbon in the copper foil precipitates to the top and bottom surfaces of the foil, usually forming individual graphene domains at multiple nucleation sites, resulting in a polycrystalline graphene film on both sides of the Cu foil. After several minutes, we stopped the flow of the gases and left the system to cool to room temperature at the base pressure. Finally, we removed the foil from the tube and stored it until the desired time-of-use.

3.3.1.2 Multilayer hBN Purchased from 2D Semiconductors

We obtained multilayer hBN samples from 2D Semiconductors for use in this work. The hBN films were polycrystalline in nature and were grown by CVD on Cu foil. Additionally, the hBN films were nominally five layers thick. Given that the out-of-plane lattice constant of hBN is 3.33 Å, five layers of hBN corresponds to a nominal thickness of about 1.67 nm [121].

3.3.2 Device Fabrication

This subsection is organized into several parts. The specific details of the sample fabrication process used to construct the photodetector device are discussed in Section 3.3.2.5. However, the fabrication process combines several device processing techniques to achieve the ultimate goal. For the sake of clarity and to provide context, general discussions of each of these techniques are presented before discussing the device fabrication process itself (i.e., in Sections 3.3.2.1 - 3.3.2.4).

3.3.2.1 Wet Transfer Process

We used a “wet transfer” process to remove CVD-grown materials from their growth substrates and transfer them onto a new substrate for incorporation into the hBN-based photodetector device. The process will be described here as the process of transferring CVD graphene, but the same process was also used to transfer the multilayer hBN. Wet transfers begin by spin coating the desired CVD-grown graphene film with a support polymer layer. In our case, we applied an approximately 375 nm thick film of poly(methyl methacrylate) (PMMA) using a spin coating process. This involved spin coating the graphene-on-copper foil sample with a PMMA solution (495 PMMA A4 from MicroChem) at 2000 RPM for 1 minute, followed by a soft-bake on a hot plate set to 150 °C for 5 minutes in air to drive out any remaining solvent from the PMMA film. We specifically coated the graphene film which had been grown on the top side of the foil (as it was positioned in the tube furnace during growth), as the top-side graphene film tends to be of higher quality than the back-side graphene. The next step in the wet transfer process is to remove the back-side graphene from the foil to prevent it from interfering with the transfer. We accomplished this by floating the graphene-on-copper foil sample with the top-side graphene face up on a 10 %(v/v) nitric acid solution (in DI water) for 10 minutes. During this time, the nitric acid chemically etched the bottom surface of the copper foil (since the top surface was protected by the PMMA layer), thus releasing the back-side graphene from the foil and letting it fall into solution. After removing the back-side graphene, we rinsed the nitric acid from the copper foil in sequential DI water baths, then placed the foil (with freshly-exposed copper face down and top-side graphene face up) on the surface of a 2 %(v/v) ammonium persulfate (APS) solution overnight. The APS solution etched away the remaining copper foil, leaving only the polymer-supported top-side graphene floating on the surface of the APS solution. We then used a clean glass microscope slide to carefully scoop the floating PMMA-graphene film from the APS solution and place it onto the surface of a DI water bath to rinse away any remaining APS solution, then repeated this process for a second DI water bath. The final stage in the wet transfer process involved using the target substrate to scoop the graphene film from the surface of the bath. This process resulted in a significant amount of water at the interface between the graphene film and the target substrate, which needed be dried before the graphene would securely adhere to the substrate. With this in mind, we placed the graphene-coated substrate on a hot plate set to 85 °C, ramped the temperature up to 110 °C over the course of 5 minutes, then held at this temperature for 10 minutes. We found that the temperature ramp and hold method effectively removed the water from the sample-substrate interface, while also preventing catastrophic rupturing of the graphene films due to violent generation and escape of steam at the interface. Finally, the PMMA layer was removed by sequentially soaking the sample-substrate in acetone, isopropanol, and DI water baths for 10 minutes each before being blow-dried with dry nitrogen.

3.3.2.2 Contact Pad Patterning

We used the shadow-masking technique to pattern Au/Cr contact pads on our device. While shadow masking is typically limited to patterning structures which are relatively large when compared with photolithography and electron beam lithography, it is simpler and faster to execute. The process begins by preparing the substrate or device onto which metal contacts are to be patterned. In the case of this work, we patterned two sets of contacts (one set for each graphene electrode) by repeating the following process twice. The first step was to arrange the desired shadow mask (similar to a stencil pattern) over the device, ensuring proper alignment during the process (shown as step 1 in Figure 3.5). Next, we loaded the masked sample into the vacuum chamber of a thermal evaporator (in the Ishigami lab), whereupon the chamber was evacuated to a base pressure of $2 \cdot 10^{-6}$ Torr. After the chamber had reached base pressure, we degassed both the Cr and Au sources, with a shutter interposed between the sources and the device to block any material that would have been otherwise deposited. This removed any surface oxides or other contaminants from the sources, ensuring the cleanliness of the metal films soon to be deposited to form the contacts. We then deposited 5 nm of Cr at a rate of 0.8 $^{\text{Å}}\!/\!_{s}$, followed by 60 nm of Au at a rate of 1.5 $^{\text{Å}}\!/\!_{s}$. The Cr served as an adhesion layer, binding the Au to the substrate. This is shown schematically in step 2 of Figure 3.5. Following this process, we let the sample cool under vacuum for 30 - 60 minutes before removing it from the chamber. Finally, we removed the shadow mask from the device, leaving behind the patterned contacts (shown schematically in step 3 of Figure 3.5), and stored it in a nitrogen box until the time came for further processing.

3.3.2.3 Reactive Ion Etching

Reactive ion etching (RIE) is a technique that can be used to remove certain materials from samples and is often used in lithographic processes. The working principle of RIE is as follows. A sample with material to be etched is first loaded into a vacuum chamber and the vacuum chamber

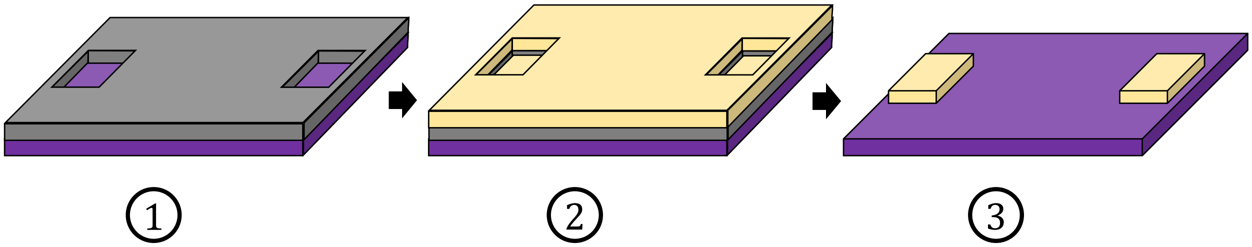

Figure 3.5: Schematic outlining the main steps of a shadow masking process to pattern two counter-electrodes. Purple color denotes the silicon substrate, dark gray the shadow mask, and yellow the deposited Au/Cr.

is evacuated to its base pressure. A small amount of a processing gas (O_2 and SF_6 are common choices) is controllably leaked into the chamber (typically using mass flow controllers to accurately control the flow), creating a low-pressure ambient of the process gas in the chamber. The pressure in the chamber is regulated by controlling the effective pumping speed of the vacuum pump, which continuously acts on the chamber, by means of a valve at the outlet port of the chamber. When the pressure has equilibrated to the desired level, a radio frequency (RF) signal (i.e., an AC voltage, typically with a frequency of 13.56 MHz) is applied between a pair of parallel electrodes inside the chamber, one of which the sample is typically placed atop. The AC voltage signal is strong enough to strip electrons from the processing gas molecules, thus ionizing the gas and sparking a plasma. The processing gas is chosen specifically such that, when it is converted into a plasma, the resulting molecules will be highly chemically reactive with the material to be etched. These ionized molecules are then allowed to impinge on the surface of the sample (with minimal kinetic energy, as this is not a sputtering technique), whereupon they react with the material to be etched. The ionized processing gas molecules are then pulled away from the surface of the sample, bringing the reacted material with it. Finally, both the ionized processing gas molecules and the reacted molecules from the sample are removed from the chamber by the vacuum pump. The rate of etching during this process depends on various factors, including the composition of the process gas, the pressure in the chamber during the etching process, and the amount of RF power delivered to the electrodes.

We used RIE to selectively etch graphene during the fabrication process described in this chapter. We carried out the RIE using a Samco reactive ion etching system equipped with a radio frequency generator (manufactured by Advanced Energy, model # RFX-600). Before performing the RIE process, the system was evacuated to a base pressure of 20 mTorr. We used O_2 (flowing at 5 sccm) as the processing gas, as it effectively etches graphene. During the etching process, the system maintained a pressure of 53 mTorr in the chamber and applied 50 W of RF power. We subjected the sample to the resulting O_2 plasma for 3 seconds. After processing, we re-evacuated the chamber to remove residual O_2 ambient before venting the system to retrieve the sample.

3.3.2.4 Wire Bonding

Wire bonding is a commonly-used method of making electrical contact between contact pads on a sample or device and a chip carrier, thus enabling improved interfacing of measurement equipment with delicate microelectronic devices. The process is deceptively simple: a thin wire is pressed into physical contact with a contact pad (perhaps on the sample) by a tool in the wire bonder, at which point the wire bonder sends an ultrasonic signal to the wire, applying additional force and locally heating the wire in the process. This, in turn, causes the wire to melt at the point of contact with the sample and, ideally, create a strong mechanical and electrical connection to the contact pad. After a bond is made with a contact pad, additional wire (still attached to the newly-made bond) can be un-spooled and drawn toward another bonding pad (perhaps on a chip carrier) and the bonding process repeated. Finally, the remaining wire at the bonding tool will be severed from the second bond site, thus leaving the bonded wire in place to electrically connect the two contact pads. A bonding tool and wire are shown in Figure 3.6a-b and an example wire bond is shown in Figure 3.6c. While this process is, in principle, very simple, the success rate of bonds attempted depends sensitively on the bonding parameters used (such as bonding force, ultrasonic pulse length, and bonding tool temperature), sample cleanliness and technique (e.g., the angle of approach used when lowering the bonding tool to make a bond). For this reason, it is common for bonding processes to take a not insignificant amount of process optimization. In this work, we used a West Bond wire bonder equipped with a 45 ° wedge. The wedge was responsible for feeding wire to the bonding tool, and clamping the wire in place when necessary. We used Si-doped Al wire (1% Si in 99% Al) with a diameter of 1 mil and an elongation rating of 0.5-2% for the purposes of this work. More details relating to wire bonding, including the procedure and troubleshooting hints, are included in Appendix D.

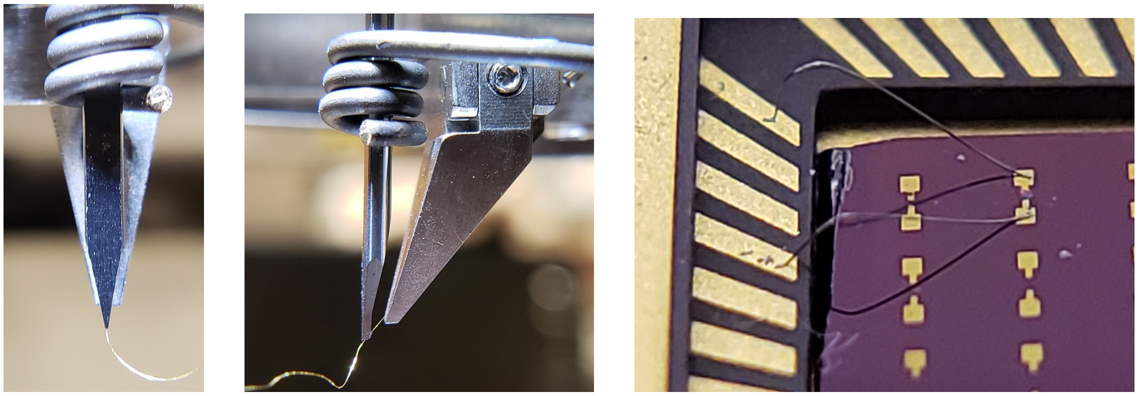

(a) Front view.

(b) Profile view.

(c) Example wire bonds made between a dummy sample and a chip carrier.

Figure 3.6: Pictures showing the bonding tool and 45 ° wedge of a West Bond wire bonder (Subfigures a and b) and example wire bonds.

3.3.2.5 Device Fabrication Process

We used a multistep process to fabricate the CVD hBN-based UV photodetector discussed in this chapter. This section will describe the fabrication process, while the details for the individual steps and techniques can be found in the preceding sections. For this work, we used an approximately 1 cm x 1 cm square chip of highly n-type doped Si, with 280 nm of polished thermal oxide grown on the top surface as the substrate. Before performing any of the following processing steps, we cleaned the substrate by sonicating it sequentially in acetone, isopropanol, and DI water, followed by blow-drying it with dry nitrogen.

The first step of the fabrication process involved preparing the bottom electrode of the vertical photodetector device. We did this by transferring a 4 mm x 8 mm film of CVD-grown, monolayer graphene onto the substrate, employing the wet transfer method described in Section 3.3.2.1. In this case, we used the SiO_2/Si substrate itself to scoop the graphene film from the surface of the final bath, being careful to align the film with the center of the substrate as well as possible. After the adhesion-promoting bake and removal of the PMMA support layer from the top surface of the graphene, we patterned a set of two contact pads, one covering each of the shorter sides of the graphene strip. We used shadow masking to define the pattern and thermal evaporation to deposit the 55 nm thick Au/Cr contacts, as described in Section 3.3.2.2. The fabrication process up to this point is shown schematically as steps 1 and 2 in Figure 3.7.

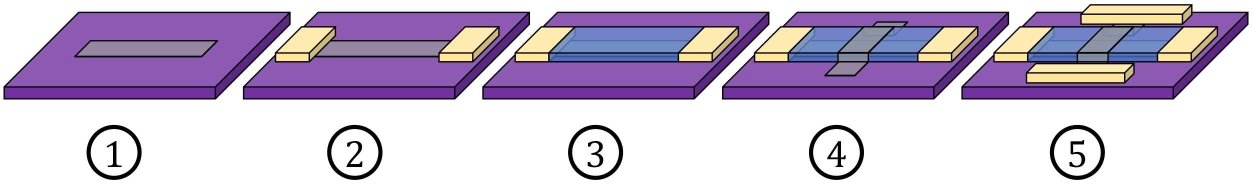

Figure 3.7: Schematic showing the main steps taken to fabricate the vertical, CVD hBN-based photodetector.

The next task was to stack the multilayer hBN film atop the bottom graphene electrode. This process was essentially identical to the wet transfer of graphene described above, except that we started with a ~6 mm x 6 mm multilayer hBN film on copper. When scooping the hBN film from the water bath, we took care to completely cover the bottom graphene electrode, as well as a small portion of its Au/Cr counter-electrodes. One additional deviation from the graphene wet transfer process is that we did not immediately dissolve the support polymer layer from the hBN film. The end result of this process is shown as step 3 in Figure 3.7.

Before proceeding with the remaining steps of the device fabrication process, we needed to ensure that there would be no electrical shorts between the top and bottom electrodes of the device. While the wet transfer method described in Section 3.3.2.1 is effective for transferring large-area films, it can cause structural damage to delicate monolayer and few-layer films, even with the use of a support polymer. Such damage usually manifests itself in the form of rips and tears. Since this device geometry is vertical in nature, any rips or tears in the hBN layer would allow the top graphene electrode to drape down onto the bottom graphene electrode, thus creating a short circuit between the electrodes. Such a short circuit would amount to a path for a large "leakage current" through the device, hindering our ability to detect the photocurrent signal, and significantly reducing the ultimate signal-to-noise ratio of the device. To prevent any possible shorts, we treated the sample with reactive ion etching, with the support polymer from the hBN transfer still in place, to remove any exposed graphene from the bottom electrode. The rationale for this is that any damage to the hBN film would most likely also result in corresponding damage to the support polymer. It is precisely these damaged regions that would allow the top graphene to contact the exposed bottom electrode. In this way, the support polymer film essentially acted as an etch mask, exposing the bottom layer graphene which needed to be removed, while protecting the rest of the hBN and graphene films. The reactive ion etching was performed as described in Section 3.3.2.3. After completing the RIE, we dissolved any remaining support polymer from the hBN as described in Section 3.3.2.1.

The penultimate task in fabricating the detector involved establishing the top electrode. This electrode comprised another 4 mm x 8 mm strip of monolayer, CVD graphene stacked atop the hBN film perpendicular to the bottom layer of graphene (as shown schematically in step 4 of Figure 3.4). As described above for the bottom electrode, we dissolved the support polymer layer from the graphene and patterned another set of Au/Cr contact pads for the top graphene electrode. This arrangement resulted in a 16 mm^2 area where the graphene electrodes (each 4 mm wide) overlapped, with one electrode on each surface of the hBN. This means that the vertical CVD hBN-based UV photodetector had an active area of 16 mm^2. The result of this process is step 4 in Figure 3.7.

Before we could perform any electrical measurements of the device, we needed to mount the finished device in a chip carrier. The use of a chip carrier not only allowed for more convenient handling of the delicate device, but also facilitated more robust electrical contact between the device itself and any measuring equipment. We used a leadless chip carrier with 68 contact pads (LCC, part number LCC06860 obtained from Spectrum Semiconductor Materials, Inc.), shown schematically in Figure 3.8a. This type of LCC is meant to be inserted into an appropriate LCC socket (e.g., part number 620-68-SM-G10-S14-1 from Andon Electronics Corp). Such sockets are usually surface mount devices, and must be soldered to a suitable printed circuit board (PCB). In our case, the PCB was a PLCC-68 socket to PGA-68 adapter board (product number PA0108C-R purchased from Proto-Advantage) with the socket replaced by the one mentioned above. The PCB had connection pins which were compatible with Dupont-style jumper wires. A schematic of the assembled socket and PCB is shown in Figure 3.8b. We used wire bonding (described in Section 3.3.2.4) to make electrical connections between the contact pads on the device and the leadless chip carrier.

3.3.3 Ultraviolet-Visible-Near Infrared Spectrometry

We used ultraviolet-visible-near infrared (UV-Vis-NIR) spectroscopy to determine the energy band gap of the multilayer, CVD hBN films used in this chapter. To this end, we prepared a sample of the hBN film, taken from the same source as the one described above, using the wet transfer technique (described in Section 3.3.2.1), but without any of the additional processing used to fabricate the UV photodetector device described above. Since UV-Vis-NIR spectroscopy is most commonly performed in transmission mode, the substrate onto which we transferred the hBN film needed to be transparent and as spectroscopically featureless in the ultraviolet and visible regions of the electromagnetic spectrum as possible. This was done to ensure that we could get transmit-

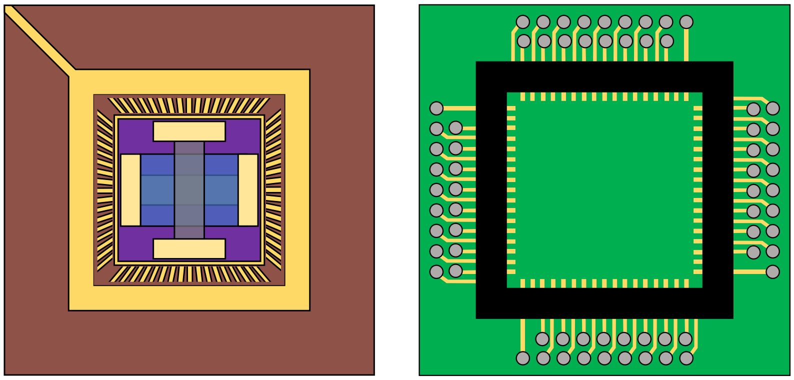

(a) Overhead view of the photodetector device mounted in the leadless chip carrier.

(b) Overhead view of the socket and PCB used to secure the chip carrier.

Figure 3.8: Schematics of the chip carrier and socket used to interface the photodetector device with the measurement electronics. The LCC shown at left would be inserted into the cavity (surrounded by the black ring) in the diagram at right.

tance data that was primarily representative of the hBN film rather than the substrate itself. For this reason, we chose to use single-crystalline, optical grade, Z-cut quartz (1 cm x 1 cm x 1 mm, two-side polished, product number SOZ101010S2 from MTI Corp) as the substrate material.

We used a Cary 500i UV-Vis-NIR spectrophotometer to perform our spectroscopic investigations. The spectrophotometer was equipped with deuterium and mercury lamps to provide optical excitation in the wavelength range of about 175 nm to 2000 nm. We let the lamps in the instrument warm up for one hour before performing any measurements to ensure that their output was stable. Finally, we mounted the hBN/quartz sample in the front beam path of the spectrophotometer using a custom-designed, 3D printed flush mounting adapter. This adapter helped to ensure that the sample was properly centered in the beam and that the light passing through the sample would do so at nominally normal incidence. A technical drawing of this adapter is included in Appendix E, labelled as “Cary UV-Vis Adapter”, and an image of the 3D model shown in Figure 3.9. A brief description of the adapter is as follows. The slot in the front face of the adapter was designed to be only slightly larger than the beam passing through the spectrophotometer. The slot would be aligned with the beam when the adapter was oriented with the more closely-spaced horizontal indentations toward the bottom of the adapter. Thus, placing the sample so that it covered the entire slot guaranteed that the entire beam (which was elongated rather than circular) would pass through the sample. We set the spectrophotometer to measure with a spectral bandwidth (SBW) of 2 nm and an acquisition time of 0.2 seconds per data point. Additionally, we set the instrument to perform the source changeover (from UV to Vis-IR) at 400 nm, while the detector and grating changeovers occurred at 850 nm. Instrumentation changeovers cause artifacts (jump discontinuities) to appear in the recorded spectra, which were corrected for using standard background correction procedures.

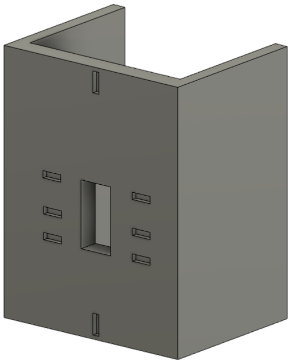

Figure 3.9: 3D rendering of the UV-Vis-NIR adapter used to align the sample to the beam path. The slot in the center of the front face allows the beam to pass through. The smaller indentations on the front face are intended to assist in aligning the sample. The middle set of indentations are more closely spaced to the bottom set than the top set (in the orientation shown here), indicating that the adapter is right-side up.

3.3.4 Photoconductivity and Photovoltaic Measurements

Our optoelectronic characterizations of the CVD hBN-based photodetector device involved measuring IV curves both with and without UV illumination, as well as measuring the photoconductive and photovoltaic responses. All such measurements involved electrically interfacing with the photodetector device through the LCC socket (as described at the end of Section 3.3.2.5) by means of Dupont-style jumper wires. To measure the current-voltage response of the device (i.e., IV curves), we used a Keithley 2400 SourceMeter unit (SMU) to both apply a voltage between the top and bottom electrodes of the device and to measure the resulting current. During IV curve acquisitions, we first grounded both electrodes, then swept to the negative end of the desired voltage range, swept the voltage to the positive end of the desired range, collecting IV data during the process, and then back to 0 V at the end of an acquisition. Photoconductivity measurements also utilized a Keithley 2400 SourceMeter unit, but we held the applied voltage at a constant value throughout the entire test, rather than sweeping it, while also continuously measuring the current through the device. Finally, we used a Keithley 2000 Multimeter to measure the photovoltage set up between the top and bottom electrodes during the photovoltaic measurements. The data acquisition was handled in all cases using custom LabVIEW virtual instruments (VIs) used in concert with a GPIB-to-USB adapter interface. The measurement set up acquired data at the default sampling rate of the SMU, corresponding to about 13 Hz (or one sample every 77 ms).

We used two commercially-available UV lamps to provide optical excitation during the optoelectronic characterizations described above. The first UV source was a low-pressure mercury lamp (Ster-L-Ray G18T5L-U from Atlantic Ultraviolet). According to the manufacturer's specifications, the main wavelength component of light emitted from this lamp occurred at 254 nm, corresponding to a photon energy of 4.89 eV) and accounted for about 85 % of the total emitted optical power. The remaining power was distributed between emission lines in the wavelength range between 313 nm and 546 nm (2.27 eV - 3.96 eV). We estimate that this source provided an optical power density of about 23 $^{\mu W}/_{cm^2}$ at our device during the measurement process. The second lamp was a high intensity handheld germicidal lamp (UVP Blak-Ray B-100A from Analytik Jena). The manufacturer specifications for this lamp indicated that the primary emitted wavelength was 365 nm (3.40 eV), with a small fraction of the emitted power occurring in the range of 315 nm to 400 nm (3.1 eV - 3.9 eV). We estimate that this source produced an optical power density of about 6700 $\mu W/cm^2$ at our device during the measurement process. During the photoconductive and photovoltaic measurements, we alternated between periods with and without illumination of the photodetector device, testing with only one type of lamp during a measurement. To accomplish this, we switched the Ster-L-Ray lamp on and off at approximately 30 second intervals, while we chose to physically move the handheld germicidal lamp away from and back to the device (being careful to return it to the same position each time) at about the same intervals. We specifically chose to move the handheld lamp rather than switch it on and off because it took at least one minute to turn on and warm up before a significant portion of its steady state UV output level could be reached. The Ster-L-Ray lamp, on the other hand, typically required no warm up time, emitting almost immediately after receiving power from its power ballast. For convenience, we will henceforth refer to the low-pressure mercury lamp described as UV Source 1, and the handheld germicidal lamp will be referred to as UV Source 2.

3.4 Results and Discussion

Our optical characterization shows that the multilayer CVD hBN used in this experiment has an optical band gap approximately consistent with that expected from the literature. Optical transmittance data, shown in Figure 3.10a, reveals that the hBN film absorbs light primarily in the UV range below about 215 nm (i.e., above about 5.7 eV), with a maximum absorptance of 0.18 occurring at 202 nm (6.1 eV). In contrast, the absorptance for light with wavelengths longer than 215 nm (only a portion of which is shown in Figure 3.10a) is less than 0.05. This indicates that, while the film absorbed a small portion of light in the upper-middle ultraviolet to infrared range, most of the absorption happened in the lower-middle to far ultraviolet range. These results suggest that the hBN films used in this study were able to absorb an appreciable amount of the incident UV light, despite the fact that the film is only a few layers thick.

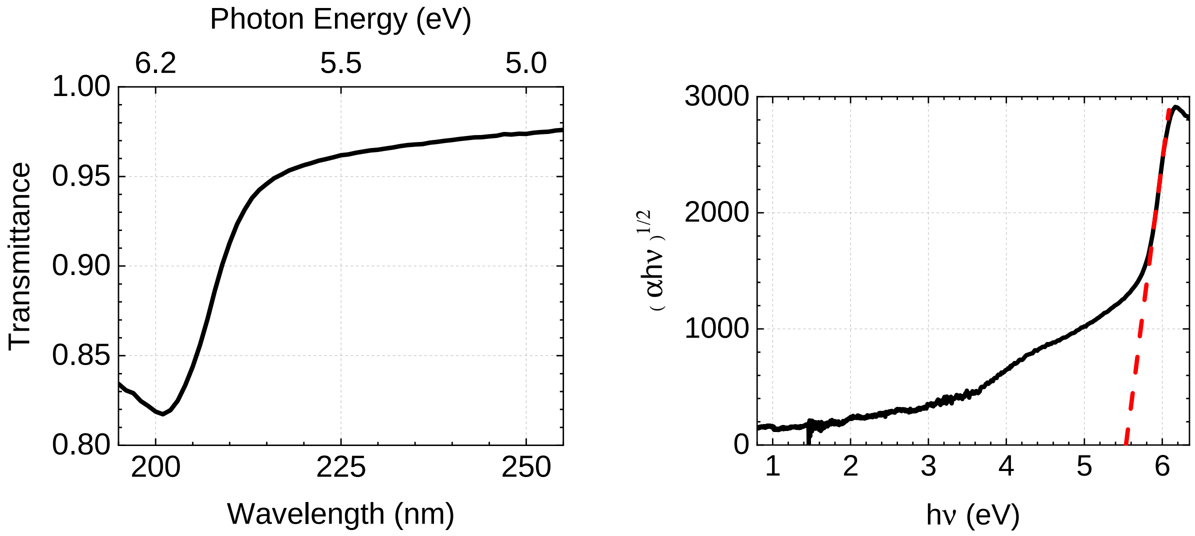

(a) Transmittance spectrum.

(b) Tauc plot. The dashed red line represents the fit to the linear portion of the low-energy absorption band edge.

Figure 3.10: Optical characterizations of multilayer hBN samples used in this chapter. Reprinted with permission from Springer Nature: Springer *MRS Advances*, [67], ("Solar-Blind Ultraviolet Photodetectors Based on Vertical Graphene-Hexagonal Boron Nitride Heterostructures", Thompson, J., et al.), © 2020.

Figure 3.10b shows a Tauc plot, generated according to the procedure detailed in Section 3.2.4. Since hBN films comprising more than one layer are known to have an indirect band gap, $n = 2$ is the appropriate choice for the exponent in Equation 3.6 [84, 122]. The result of this analysis is that the optical band gap of the hBN used in this experiment is about 5.53 eV, in relatively good agreement with other values reported in the literature [87, 90, 123, 124]. However, we note that the absorption band edge is not as abrupt as one might expect, due to the presence of one or more broad absorption tails centered around 4.5 eV. These are possibly an Urbach tail and a weak-absorption tail. These kinds of tails are typically due to disorder in the measured film. This disorder creates in-gap states near the valence and conduction bands, thus allowing electron transitions to occur at energies that would normally be forbidden. The tails could be due to Nitrogen vacancies or carbon substitutional defects [125, 126].

Figure 3.11a shows an IV curve, representative of our CVD hBN UV photodetector device, acquired in the dark. It is evident from this plot that currents on the order of microamperes, which are easily measurable with the setup described in Section 3.3.4, could be produced by the application of less than 1 V to the device. With this in mind, and to prevent possible dielectric breakdown of the device, we chose to focus on the low voltage behavior of our device during further characterizations. Careful inspection of Figure 3.11a reveals that there is a slight non-linear dependence of the current on the applied voltage in the low voltage regime, but that the curve is symmetric about the origin. Nevertheless, we estimate that the effective resistance of the photodetector device is about 2.14 kΩ. We also measured IV curves for the graphene electrodes individually, applying the voltage across the pairs of contacts on opposing ends of each graphene electrode. These IV curves were highly linear and were consistent with a total resistance of 273 Ω for each graphene channel. The marked difference in resistance between the graphene electrodes and the device as a whole suggests that the efforts to prevent electrical shorting (described in Section 3.3.2.5) were successful.

Acquiring additional IV curves with the photodetector device under illumination by UV Source 1 (as described in Section 3.3.4) shows small, but measurable, differences from the IV curves taken without illumination. The differences in current with and without illumination were too small to be seen at the scale present in Figure 3.11a, so we did not plot a curve acquired under illumination on this plot. Instead, we calculated the absolute value of the difference in current between the two curves, and this is shown in Figure 3.11b. From this plot, we see that the current through the device with illumination is greater than that without illumination, except at around zero bias. This is as we would expect for photoconductive measurements of a photodetector, and provides initial confirmation of the operation of the device.

The UV photodetector device further demonstrated photo-induced modulations of conductivity under the influence of time-varying illumination. The details of this experiment are discussed

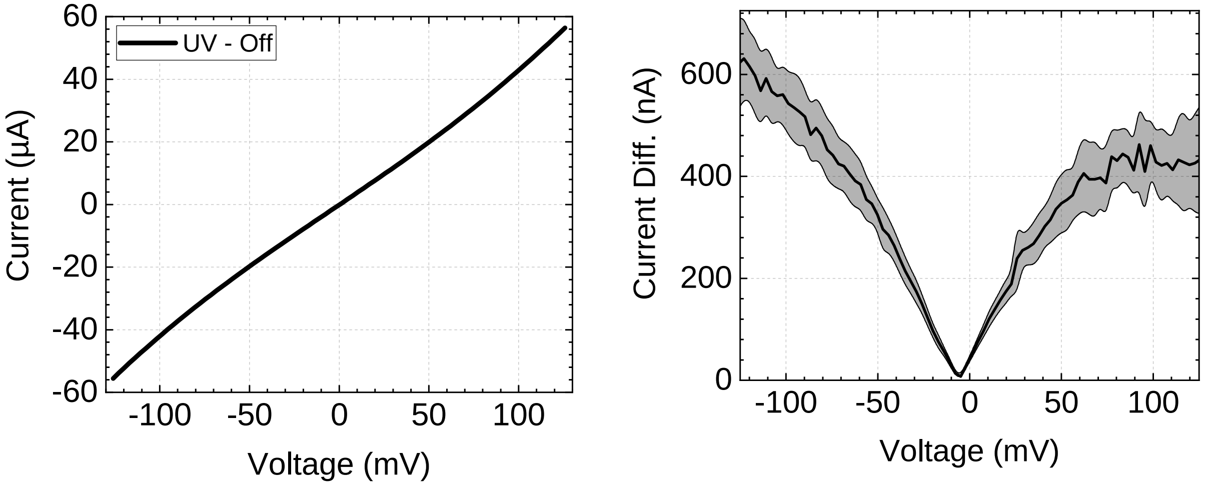

(a) IV curve of photodetector device.

(b) Current magnitude difference spectrum.

Figure 3.11: Selected IV curve data showing differences between measurements taken with and without UV illumination. Reprinted with permission from Springer Nature: Springer *MRS Advances*, [67], (“Solar-Blind Ultraviolet Photodetectors Based on Vertical Graphene-Hexagonal Boron Nitride Heterostructures”, Thompson, J., et al.), © 2020.

at the end of Section 3.3.4. In brief, we exposed the device to alternating periods of darkness and illumination by the UV lamps and measured the resulting current. During these measurements, we applied a constant 150 mV voltage bias to the device. Figure 3.12a shows the time series data collected while using UV Source 1 during periods of illumination. The lower panel indicates the illumination status of the device (e.g., “UV On” corresponds to the device being illuminated), while the top panel shows the measured current. From this plot we see that, during periods without illumination, the dark current was relatively consistent and had an average value of 69.302 μA $\pm$ 0.016 μA. This is due to leakage current through the device and is comparable to that of other, similar heterostructures [127]. Conversely, during periods of illumination the current rapidly increased to an average value of 69.933 μA $\pm$ 0.022 μA. The difference between these two current values corresponds to a 631 nA photocurrent generated by the UV illumination.

Figure 3.12b shows a portion of the data from the upper panel of Figure 3.12a, focusing in

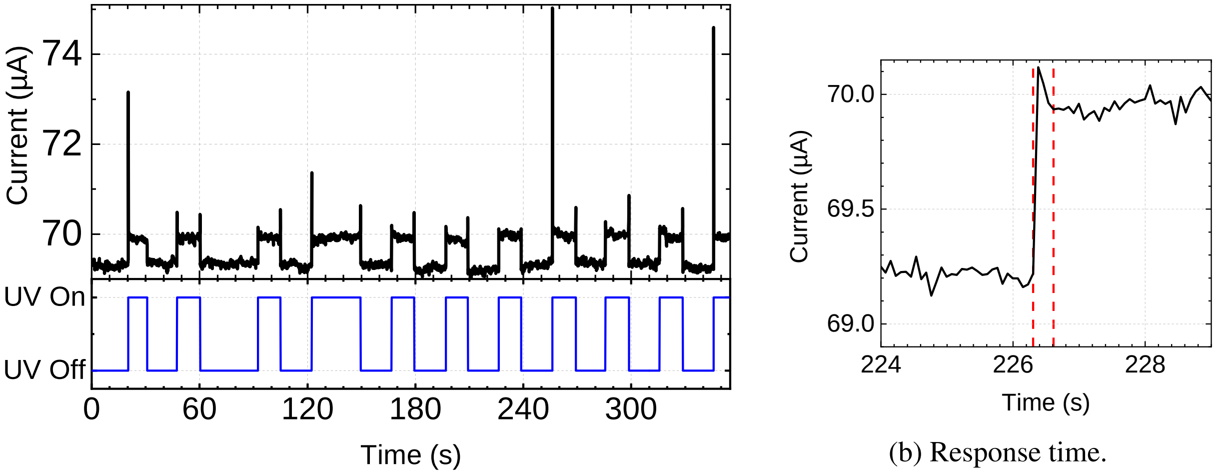

(a) Photocurrent plot for UV Source 1.

(b) Response time.

Figure 3.12: Photocurrent data from experiment. Reprinted with permission from Springer Nature: Springer *MRS Advances*, [67], ("Solar-Blind Ultraviolet Photodetectors Based on Vertical Graphene-Hexagonal Boron Nitride Heterostructures", Thompson, J., et al.), © 2020.

on one of the transitions from dark current to photocurrent. The left vertical, dashed line represents the time at which UV Source 1 began outputting. The current increases immediately afterward, forming a sudden spike before settling down to a steady state value. The right dashed line represents the time at which the steady-state current was reached. The separation between the two dashed lines, then, represents the total time needed for the device to reach steady-state operation after being illuminated by UV Source 1, which serves as an estimate for the response time of the device. Taking the average of the corresponding times for the data shown in Figure 3.12a gives a value of 310 ms ± 40 ms. It is worth noting that this method of determining the response time of the device is somewhat different from the standard methods used elsewhere, in which the response time is usually defined as the time needed for a photodetector to reach either 71% or 90% of its steady-state value. However, there are two complicating factors which make the standard methods less applicable here. The first is the presence of the initial spike in current after switching the light on, as this obscures the asymptotic approach of the current to its steady-state value, which would be expected in the absence of other effects. The second, and more import, factor is that the temporal resolution of our measurement apparatus was insufficient to visualize the transient behavior of the device with sufficient confidence. This is evident from the fact that there were only four data points between the two vertical lines in Figure 3.12b. Performing similar characterizations of the photodetector device using UV Source 2 showed no discernible deviation from the dark current, even during periods of illumination. Given that UV Source 2 had a significantly higher optical power density than UV Source 1, this indicates that the photodetector was essentially insensitive to light with wavelengths between about 315 nm to 400 nm (3.1 eV - 3.9 eV). This is consistent with what one might expect given the Tauc plot shown in Figure 3.10b.

We found that the hBN photodetector device was able to operate in photovoltaic mode. Figure 3.13 shows time series data of the voltage measured across the contacts of the photoconductor, as measured by the Keithley Multimeter 2000, under alternating periods of darkness and illumination by UV Source 1. During periods of darkness, the measured voltage was 3.5 μV $\pm$ 1.0 μV, which we attribute to an instrument offset artifact. With the photodetector device illuminated, however, the measured voltage jumped to -206.9 μV $\pm$ 6.1 μV. These measurements, when taken together with the photoresponse measurements discussed above, suggest that a finite number of photocarriers were able to diffuse from the hBN layer to the contacts before recombining, creating a small potential difference in the process. Repeating these measurements with UV Source 2 yielded no measurable deviation from voltages measured in darkness.

Having observed both photocurrent and photovoltaic responses to UV Source 1, but not UV Source 2, it is worth discussing several possible mechanisms by which such photoresponses could have been produced. The first, and simplest, mechanism that could be responsible for the observations made above is the photovoltaic effect at work in the hBN layer. As discussed in Section 3.2.2, this would involve the promotion of an electron into the conduction band, leaving behind a hole in the valence band in the hBN, and would be caused by absorption of a photon with energy greater than or equal to the band gap of the hBN. The Tauc plot shown in Figure 3.10b yields

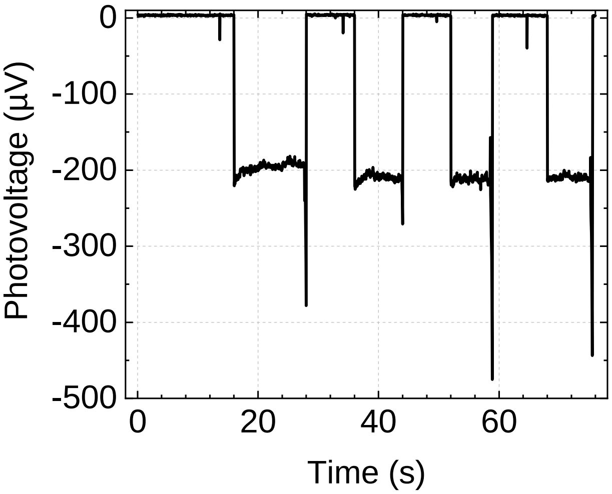

Figure 3.13: Measured photovoltage with alternating periods of darkness (V = 3.5 μV) and illumination by UV Source 1 (V = -206.9 μV). Reprinted with permission from Springer Nature: Springer *MRS Advances*, [67], ("Solar-Blind Ultraviolet Photodetectors Based on Vertical Graphene-Hexagonal Boron Nitride Heterostructures", Thompson, J., et al.), © 2020.

a band gap of 5.53 eV, which is somewhat larger than the energy of the highest-energy photons used in these experiments (254 nm, or 4.89 eV). Nevertheless, Figure 3.10b shows finite absorption of photons with energies lower than the band gap energy. This is evidenced by the presence of the tails at the absorption band edge, and implies a non-zero density of electronic states extending out into what would have otherwise been the forbidden region separating the valence and conduction bands in the first Brillouin zone. This, in turn, suggests that it is plausible to have observed photovoltaic behavior (and a resulting photocurrent response) from at least some light used in this experiment. Judging from the fact that only UV Source 1, whose primary emission line is much closer to the absorption band edge than UV Source 2, produced a measurable photoresponse, we tentatively propose that the mechanism involved could be the photovoltaic effect.

The lack of a photoresponse due to UV Source 2 suggests that the photoresponse due to UV Source 1 was not due to thermal effects in the substrate itself. Specifically, one might assert that the photoresponse shown in Figure 3.12a could possibly be due to the field effect rather than photocarriers being generated in the hBN layer. The rationale for this line of thought is as follows. The substrate on which the photodetector device discussed in this chapter was fabricated is composed of a top layer of SiO_2, with the remainder of the substrate being highly-doped Si. Si has a band gap of around 1.12 eV, which means that all the light used in this experiment possesses sufficient energy to promote electrons from the valence band to the conduction band, generating excess charge carriers in the Si [128–130]. In this way, the substrate would effectively act as a back-gate (with the highly-doped Si being the back-gate electrode and the SiO_2 serving as the gate oxide). Any excess, photo-generated charge carriers residing in the Si would set up an electric field, which would then be able to modulate the conductivity of the graphene films in the detector (as in a field effect transistor). Such a modulation of conductivity would look very similar to a photoresponse, even though it would have nothing to do with the device itself. This effect is called photogating. As stated above, however, the lack of a photoresponse due to UV Source 2 rules out this explanation for the photoresponse shown in Figure 3.12a. The reason for this is that, if photogating were responsible for the current modulations, it should have been present during our measurements with UV Source 2. In fact, it should have been much more pronounced in measurements of UV Source 2 than for UV Source 1, as the optical power density of UV Source 2 was significantly larger than that of UV Source 1. With this in mind, we rule out the possibility of photogating as the mechanism at work in our device.

Another potential mechanism that could be at play in our photodetector device is the photovoltaic effect in the graphene electrodes themselves. Indeed, photovoltaic devices comprising graphene channels have been demonstrated in the past [131–134]. However, such devices depend on the presence of a p-n junction (facilitated by electrostatically gating multiple neighboring regions of the graphene with opposite polarity). This is because the electric field established at the junction is needed to separate the electrons from the holes, preventing carrier recombination. In principle, one could argue that, since the entire photodetector device in our experiments was exposed to the UV light, the observed photocurrent response could be due to carrier generation in the graphene very near the metal contacts themselves. However, the exceedingly short carrier lifetimes in graphene impose severe limitations on such a contribution in the absence of a means of charge-separation. We estimate that only about 1 pA of photocurrent would have been generated in this way for our device when illuminated by UV Source 1. Under illumination by UV Source 2, we estimate that such a photocurrent would contribute 443 pA to the overall photocurrent. The details of these estimates can be found in Appendix C. These estimates are dramatically lower than the photoresponse shown in Figure 3.12a. With this discussion in mind, it seems unlikely that the photovoltaic effect working in the graphene electrodes is sufficient to explain the observed photoresponse.

The photothermoelectric (PTE) effect is a third possible mechanism that one might consider for explaining the photoresponse for a photodetector device composed at least partially of graphene. Photodetector devices based on the PTE operate utilizing the Seebeck effect, similar to the operation of a thermocouple. As such, a PTE-based device must include a junction between two regions with different Seebeck coefficients. To accomplish this, two different materials could be combined two form a heterojunction. However, devices comprising only graphene have also demonstrated PTE operation. These all-graphene devices essentially formed a homojunction by leveraging electrostatic gating and the field effect [135, 136]. Essentially, one region of the graphene was made to be p-type, while the neighboring region was made to be n-type, forming a p-n junction between them. In this way, the Seebeck coefficient of each region of the graphene film could be controlled electrostatically. In order for a PTE-based device to function, there must be a temperature gradient in the sample. The discussion to this point has focused on the thermoelectric effect specifically. The optical part of the PTE involves using a laser to locally heat the graphene film used in the device. If the junction itself is heated, the thermoelectric effect will generate a thermo-voltage due to the optical heating, which in turn can set up a photocurrent. With this discussion out of the way, we move to discussing our hBN photodetector device. Recall that our device was symmetric (Au-Graphene-hBN-Graphene-Au), with no way to locally alter the Seebeck coefficient, unlike in the studies cited above. Additionally, the entirety of our device was illuminated by the light sources. These two factors, taken together, suggest that there should not have been any net contribution to the measured photoresponse due to the PTE. This is because, even if a thermo-voltage were generated in our device (say, at a Au-Graphene junction), the symmetric nature would result in the same thermo-voltage being generated on the opposite side of the device, thus cancelling each other out. This suggests that the PTE shouldn't have played a significant role in our photoresponse.

The final two mechanisms that we consider here are photon-assisted Schottky emission and photon-assisted tunneling. As discussed above, when the graphene layer absorbs a photon, an electron from the valence band will be promoted to the conduction band (as long as there is an available state at the appropriate energy level), leaving behind a hole. Immediately after the photon absorption, the promoted electron will be at a higher energy state, determined by the energy of the absorbed photon and the starting energy state of the electron. Over time, carrier-carrier interactions facilitate the transfer of kinetic energy between any carriers involved. This process is called thermalization. After this process happens enough times, a new distribution of carriers in the conduction and valence bands will be set up. However, the distribution over energy states will not be consistent with the Fermi-Dirac distribution for the temperature of the sample [137]. Instead, it will be better modeled by the Fermi-Dirac function evaluated at an effective temperature higher than that of the sample. For this reason, the carriers involved are referred to as "hot carriers". The result of this is that some hot carriers can have enough energy to undergo Schottky emission over the Schottky barrier due to the hBN [138]. However, if the hot carrier distribution is insufficient to allow for Schottky emission, tunneling through the barrier is another potential option. Photons can assist with such a tunneling process by promoting electrons to a high enough energy level in the graphene that they will be able to access the triangular region of the tunnel barrier (caused by the application of voltage). This is referred to as photon-assisted tunneling and is more likely to happen with the application of higher voltages.

Hot carrier-based photodetector devices comprising graphene and a semiconducting or insulating tunnel barrier have been demonstrated in the past [139, 140]. Additionally, devices similar to the one discussed in this chapter (comprising graphene-hBN-graphene) have also been demonstrated. In this case, exfoliated materials were used, the devices were fabricated with thicker hBN layers, and the devices were characterized for wavelengths in the visible and infrared ranges (450 nm to 2000 nm) [141]. The authors of this study concluded that the photoresponse exhibited by their devices followed one of two mechanisms, based on the applied voltage and the energy of the incident photons. For cases where the ratio of the bias voltage (V) to photon energy ($h\nu$) was low, photon-assisted Schottky emission (which is a hot carrier effect) was found to be the primary mechanism. For cases where the ratio was high, tunneling was found to be the dominant mechanism, due to the effective lowering and narrowing of the tunnel barrier by higher applied voltages. In both cases, holes rather than electrons were deemed the likely candidate for being primarily responsible for the photocurrent, as the tunnel barrier for holes was determined to be smaller than that of electrons using first principles calculations.

The work reported by Ma, *et al.* in [141] makes a strong case for photon-assisted Schottky emission playing a significant role in the functioning of our device. However, there are several important differences between the device design utilized in the cited study compared to the one reported herein. The first of these is the fact that the hBN in the cited study was thicker than that used in this study by about a factor of four. The increased barrier width (thickness) is likely to have suppressed tunneling current to a greater degree. This argument is consistent with the authors' statement that they measured virtually no dark current in their devices, and that photoexcitation was required to detect any current. Given the exponential dependence of tunneling (as described in Section 2.2.2 for direct tunneling), reducing the tunnel barrier width by a factor of four is likely to yield a larger tunneling current by a factor of about 55 (i.e., $e^{-d_0/4d_0} \approx 55$). Thus, we might expect tunneling current to play a more significant role in our photodetector device than the one reported in the cited study. As such, we cannot rule out the possibility that both photon-assisted tunneling and photon-assisted Schottky emission could contribute to the photoresponse in our device.

Despite the allure of the photon-assisted mechanisms discussed in the previous paragraph, there remains one fundamental difference between the work discussed herein and the work by Ma *et al.* that has significant bearing on the functioning of our device. The fundamental difference relates to the range of wavelengths used to interrogate the behavior of the devices in each study. As previously mentioned, Ma *et al.* utilized light in the visible and infrared ranges. While wavelengths in this range are sufficient to establish photon-assisted Schottky emission and tunneling, they lack the required energy to directly photo-excite carriers in the hBN layer itself. Conversely, the device discussed in this work is specifically intended to leverage the hBN layer as an active material, rather than just a tunneling barrier. As such, we assert that the photovoltaic effect, photon-assisted Schottky emission, and photon-assisted tunneling are likely to have worked together to form the photoresponse that we observed in this experiment.

3.5 Concluding Thoughts and Opportunities for Future Work

The work described in this chapter focused on fabricating and performing initial characterizations of a thin film UV photodetector based on hBN featuring a vertical device geometry. While most hBN/graphene based photodetectors utilize exfoliated materials, typically due to their generally higher crystalline quality, we used CVD-grown materials in our device. We made this design choice specifically with an eye toward enabling scalable fabrication and deployment of thin film UV photodetectors for future applications, for which exfoliated materials are unsuitable. By using multiple UV light sources, we demonstrated that our photodetector device operated in photoconductive mode when exposed to UV light with wavelengths around 256 nm, but remained largely insensitive to light with longer wavelengths. Finally, we discussed possible photoresponse mechanisms that could be at work in our device. These results confirm that vertical graphene/hBN heterostructures can be used to measure UV light signals, extending the confirmed wavelength range of operation for similar devices reported in the literature.

There are multiple paths forward for improving upon and extending the work reported in this chapter. Of particular relevance to the detector design discussed in this chapter, it would be beneficial to perform a number of additional characterizations of other large-area, CVD hBN-based vertical photodetector devices. The primary goal of such characterizations would be to more robustly identify the mechanism or mechanisms at play in such devices when exposed to UV light in the 200 nm - 400 nm wavelength range, as this would complement other characterizations of similar devices discussed in the literature. With this in mind, it would be beneficial to measure the photoresponse of our device design under illumination by a high-intensity light source that can output light with wavelengths between at least 200 nm and 400 nm, but measuring below 200 nm and into the visible spectrum would be beneficial as well. Optical parametric oscillators are one option that is well-suited to this task, as they are capable of continuously varying the wavelength of their emitted light. Another benefit is that they tend to have very narrow spectral emission lines, which is highly desirable for measuring the wavelength-dependent response of detectors. Another option could be to use a deuterium or Xenon arc lamp, which are commonly used to provide UV, visible, and infrared light for spectrophotometric experiments (e.g., UV-Vis-NIR). For the purposes of performing wavelength-specific experiments, these have the disadvantage of being broadband sources. As such, their use would also necessitate the use of optical band-pass filters to achieve wavelength-specificity.

In addition to measuring the response of hBN photodetectors over a broader range of wavelengths, there are several other measurements that, when combined with wavelength-specific response measurements, would go a long way toward fully understanding the photocurrent generation mechanisms at play. In principle, the simplest of these is to acquire IV curves and measure the photoresponse over a larger voltage range. Such measurements, when combined with fitting of the IV curves by various conduction mechanism models (such as direct or intermediate tunneling regimes, Fowler-Nordheim tunneling, or Schottky emission) would provide empirical evidence to support one or more photoresponse mechanisms, as discussed above. Performing temperature-dependent and optical power-dependent measurements would provide useful insight into the conduction and photoresponse mechanisms involved.

Moving beyond the realm of additional measurement strategies to complement the existing characterizations discussed in this chapter, several other opportunities exist. For example, as discussed in Section 3.1, fabrication of a UV-sensitive image sensor could be beneficial for applications in space research or UV spectroscopy applications. With this in mind, CVD graphene and hBN films could be patterned lithographically to create multi-pixel arrays, where each pixel would essentially be a photodetector device similar to the one discussed in this chapter. The crossbar geometry, with top and bottom graphene electrodes being patterned into strips with a rotational offset of 90 ° between layers, would be a relatively simple design to accomplish this task. This would require the implementation of dedicated read-out circuitry, however, to be practical. It would be advantageous for such an image sensor to feature very small pixels to offer very high resolution imaging capabilities. As such, another avenue of exploration could involve fabricating detectors with one or more pixel with different active areas, material thicknesses, material compositions and general electrode design. Exploring such a parameter space would enable optimization of a final image sensor design to maximize signal (e.g., with larger pixels or thicker hBN layers), minimize dark current (e.g., thicker hBN layer), and improve device response time. Additionally, variations in device behavior due to differences in material provenance (e.g., CVD or exfoliated materials) could be more fully explored. These characterizations are expected to facilitate the rational design of future thin film UV photodetectors and image sensors.

CHAPTER 4: TOWARD SOLAR-BLIND THIN FILM HEXAGONAL BORON NITRIDE-BASED PHOTODETECTORS FOR ULTRAVIOLET SENSING - PART 2

4.1 Introduction

This chapter, much like the previous one, involves work done toward fabricating hBN-based UV photodetector devices. Additionally, the device designs and compositions of the devices discussed in this chapter are similar to those in Chapter 3, in that both utilize vertical rather than lateral detector designs and both utilize graphene as the top electrode material. However, unlike in the last chapter, the hBN used in the work for this chapter was exfoliated from single-crystals rather than grown via CVD processes. We chose to use exfoliated hBN in this work because exfoliated crystals are generally of higher quality and are more likely to conform to the ideal properties that one would expect from a pure material. The goal of the work discussed in this chapter was two-fold. First, we wanted to begin a study for comparing the behavior of photodetector devices fabricated using materials (in this case, hBN) of different provenances. Second, we wanted to provide a more complete characterization of the optical response of hBN-based detectors. In this way, we hoped to gain a more robust understanding of how the composition and processing of such photodetectors could be leveraged to produce more responsive, larger-area detectors.

4.2 Background

4.2.1 Electron Beam Lithography

4.2.1.1 The General Process

Electron beam lithography (EBL) is a lithographic technique that can be used in the process of patterning a material on a sample. The result of the patterning process is similar to that of shadow masking (discussed in Section 3.3.2.2). The main difference between shadow masking and EBL is how the mask is produced. In shadow masking, the pattern to be used is pre-defined in a thin sheet of metal, usually being made in a machine shop or other physical manufacturing facilities. In EBL, however, the pattern to be used is created in a thin layer of polymer directly atop the sample or device to be patterned. This polymer layer is referred to as a "resist". There are two main advantages of EBL over shadow masking. First, EBL is capable of creating patterns with feature sizes much smaller than shadow masking or conventional photolithography. The reason for this is that an electron beam can be focused to a smaller spot size (down to several nanometers across) than even ultraviolet light (365 nm UV light is diffraction-limited to a spot size of about $\frac{365nm}{2} \approx 183nm$), which can itself produce much finer spots than mechanically cutting holes in metal sheets (as in shadow masking). Second, it is much easier to guarantee that multiple layers of a device are properly aligned with each other, even if they are to be created through multiple material depositions, for example. The discussion below includes descriptions of the EBL process in general. Specifics of the process we used for this work will be described in Section 4.3.3.1.

The EBL process begins by preparing a resist layer atop the sample which is to be patterned. The most common material used as a resist in EBL is poly(methyl methacrylate) (PMMA), as it is simple to use and is capable of supporting high-resolution patterns [142]. Polymer resists usually come pre-dissolved in a volatile solvent. As such, spin coating is a good way to apply resists to a sample and generally results in a resist layer with a fairly uniform thickness across the sample (except perhaps near any edges).

Next, the sample with resist is loaded into a system which can controllably expose the resist to high energy electrons (usually about 30-60 keV). The instrument could be a scanning electron microscope (SEM) or a dedicated EBL system. Performing EBL with an SEM requires additional hardware, enabling finer (and most likely external) control of the electron beam, that does not usually come with SEMs. Regardless of the type of system used, a focused electron beam will be moved (typically in a raster pattern) over a specified region of the sample in such a way that it draws the desired pattern. This is shown schematically in step 1 of Figure 4.1. This process is referred to as writing the pattern. The dashed black line (forming a square) with arrows in this figure indicates an example pattern to be written in the resist. During the writing process, some electrons from the focused beam will be absorbed by the resist, either before or after reflecting from the substrate. When this happens, the kinetic energy of the electrons is transferred to the molecules in the polymer resist and some portions of the polymer chains that comprise the resist layer will be severed (this is called "scission"), at least for PMMA-based resists [142]. As this process continues, an increasing volume of the resist underneath the electron beam will be affected, leading to an increasing concentration of severed polymer chains. Thus, the result of the writing process is that there will be one or more regions of the resist that have undergone scission to a significant degree (corresponding to the desired pattern), with the remaining resist unaffected. This is represented schematically in step 2 of Figure 4.1, with the darker green portion of the resist corresponding to the region that has undergone scission.

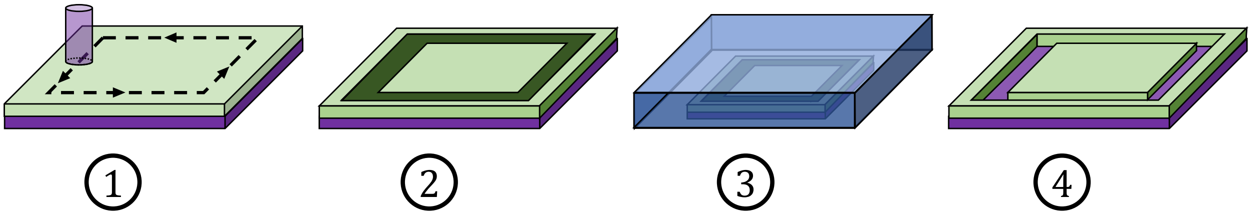

Figure 4.1: Schematic representation of the steps in an electron beam lithography process. The purple rectangular prism represents the substrate, while green colored objects represent the EBL resist. Additionally, the transparent purple cylinder in the leftmost subfigure represents the electron beam, the dark green portions the exposed regions of the EBL resist, and the blue shape in the second from right subfigure the developer solution.

Up to this point, essentially no material will have been removed from the resist. With this in mind, the next step is to remove the desired material using a process called "developing". In order to develop the pattern, the sample/resist that has had a pattern written into it is immersed in a solvent, called a "developer solution" (shown schematically in step 3 of Figure 4.1). The choice of developer solution depends on the resist being used. The general idea is that, upon immersion in the developer solution, the resist layer will start to dissolve. Crucially, however, the portions of the resist layer that have undergone a significant degree of scission will be much more soluble, and will therefore dissolve faster, than the unexposed regions of the resist [142]. As such, for a well-optimized development process, the exposed portions of the resist will be completely removed, exposing the sample underneath, while leaving the rest of the resist intact. This result is shown schematically in step 4 of Figure 4.1. A final (and very important) step is to rinse the developed pattern in a "stopping solution" immediately after the development process is complete. This will not only arrest the development process, but also wash away any remaining developer solution that would otherwise stay on the sample, potentially over-developing the pattern if left unchecked. The stopping solution should comprise a solution in which the developer solution is soluble, but in which the resist is insoluble. At this point, sample fabrication proceeds as required, for example by depositing metal to pattern electrodes or etching to remove material in the exposed region.

Finally, it is worth noting that the above discussion about developing an EBL pattern assumes that the EBL resist is a positive-tone resist (PMMA is a positive-tone resist). This means that the exposed regions of the resist will become more soluble and will eventually be removed by the developer. However, the opposite situation would be true for a negative-tone EBL resist.

4.2.1.2 Writing with Alignment

It is fairly common in microfabrication processes that a device will need to be patterned using multiple layers. In this case, each layer is fabricated (either by depositing or removing material) sequentially. This often involves using a lithographic process to create multiple patterns. Ensuring the proper relative positioning of all layers needed to fabricate a device is crucial. This is because the different layers of a device are usually meant to be stacked on top of each other. For the first pattern to be defined for a device, this is not a problem, as the pattern can be defined anywhere on the sample (in principle). However, it is often difficult to load a sample with the first pattern back into the lithographic processing instrument in such a way that it is perfectly aligned with where the sample was when writing the first pattern. As such, there will be at least a small amount of interlayer shift when the sample is loaded into the lithographic processing equipment. If left unmitigated, this would likely result in a failed fabrication process for many microelectronic devices. With this in mind, aligning the pattern to be written with the sample (or vice versa) is a vital step in the process of fabricating microelectronic devices.

The first step to aligning a sample and a pattern to be written involves defining alignment markers. Alignment markers are special features in a design whose sole purpose is to ensure that a pattern to be written will be aligned with any previously-written patterns. As such, alignment is done before a writing process commences. These alignment markers are generally separate from the features required for the device itself, usually being placed near the device in the design of the pattern to be written. Additionally, it is important that all the necessary alignment markers are deposited when writing and processing the first layer, as this enables all subsequent layers to be properly aligned, both to the first layer and to each other. Another design component required to perform alignment is an alignment window. An alignment window is a region of the pattern which allows the user to see the sample where the pattern is to be written. The specific shape and size of an alignment window depends on the type of lithography being used (photolithography or EBL). Alignment windows used in photolithography are usually the same shape as the alignment marker to which they are paired, but slightly larger. Alignment windows for EBL processes are slightly more nuanced, and will be discussed in the next paragraph. The alignment process is, in principle, simple. The user looks through an alignment window and adjusts the pattern (i.e., rotating and translating it) until the alignment windows are all perfectly aligned with their corresponding alignment marker. Best practices for microfabrication processes dictate that there should be at least one set of alignment markers (with accompanying alignment windows) for every subsequent layer to be written. The reason for this is that processing steps can obscure alignment markers as they are used, since the alignment windows themselves will cause the sample underneath them to be exposed (since the user needs to be able to see through them). As such, an alignment marker used to align a pattern for a layer which requires metallization, for example, will be covered by a layer of metal during the metallization process, becoming obscured in the process.

As mentioned above, the alignment window is slightly more nuanced in EBL processes than in photolithography processes. The reason for this is that the alignment process works slightly differently for an EBL process than for a photolithography process. In a photolithography process, a pattern to be written is physically implemented (often using semitransparent coatings) on a glass plate called a photomask. As mentioned above, a user can look through alignment windows in the photomask to gain visual feedback used for adjusting the position of the photomask. However, in an EBL process, there is no physical implementation of the pattern before the pattern is written in the resist itself. Instead, the alignment process is performed using a computer. The EBL alignment process begins by making coarse adjustments to the position of a sample inside an EBL system, usually by moving and rotating the sample stage so that the location at which a pattern to be written is directly in the center of the field of view of the system. Figure 4.2a shows an example sample coarsely aligned to an EBL system's field of view. However, the sample is rotated slightly compared to the field of view, and is off-center. Next, the EBL system scans its electron beam over predesignated portions of the field of view that correspond to the alignment windows, which are usually square. This exposes a portion of the sample to an electron dosage (which should be set to be small compared to the dosage used during the actual writing process), but also produces an SEM image for each window. Ideally, the alignment markers would be visible in their respective alignment windows. Then, shapes corresponding to the alignment markers in the design are visually overlaid atop the SEM images (shown schematically in Figure 4.2b). These overlays can then be moved around the SEM images so that they perfectly overlap the alignment markers in the images themselves. As this is done, the EBL system's software tracks the motion of the overlays. After alignment of the overlays with the markers in the image is complete, the software performs calculations on how the design pattern needs to be distorted (usually translated and/or stretched, but rotation is also possible) so that the pattern will line up properly with the alignment markers on the sample. This is shown schematically in Figure 4.2c. Factors affecting the degree to which a pattern (be it a photomask or an EBL pattern) must be distorted include sample rotation, lateral offsets, and tilt.

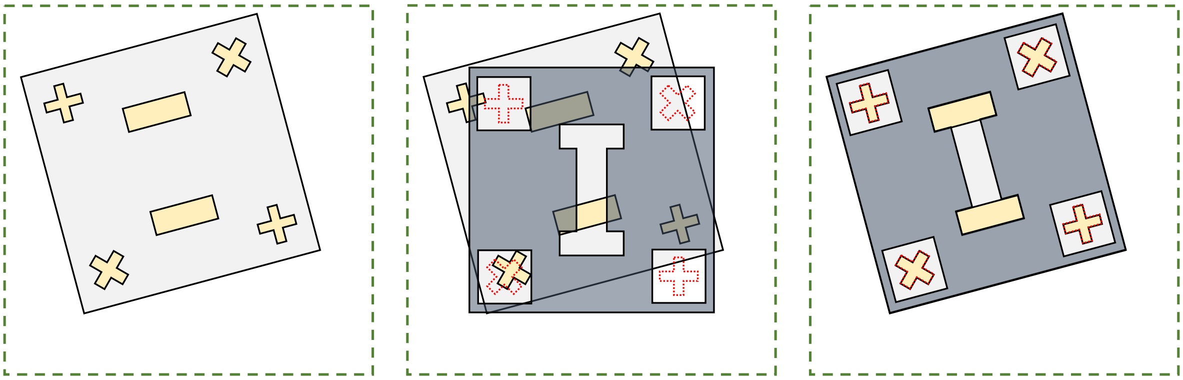

(a) Sample in SEM field of view. (b) Original pattern overlaid. (c) Pattern aligned to sample by rotation and translation.

Figure 4.2: Schematics showing an example EBL alignment process. The light gray square represents the sample's substrate. The yellow regions represent metallized features on the sample (with the 'x' and '+' marks being the alignment markers). The dark regions in subfigures b and c represent unused space in a pattern design. The open portions in the pattern represent regions where an electron beam will impinge, either during the alignment process or during writing. Specifically, the open squares near the corner of the pattern are the alignment windows, and the red dashed shapes are the reference shapes. The I-shaped open region is the pattern to be written.

4.2.1.3 Interlayer Shifts In EBL

As mentioned in Sections 4.2.1.2 and 4.2.1.6, the field of view is important for EBL processes. This is because the field of view of an EBL system dictates the largest features that can be written without changing writing parameters (such as magnification). On a related note, it is important to have a little extra space between the boundaries of the field of view and the outer edges of the design, as this is the space that will be used to transform the design to correct for sample tilt, *et cetera* during the alignment process. Generally, it is a good idea to choose a magnification which produces a field of view that is perhaps 20% larger than the device design, as long as the user can achieve relatively decent coarse alignment using the sample stage (a larger buffer zone might be required for poorer coarse alignments). This helps to maximize the writing resolution.

There is one issue, however, that can occur when using different magnifications (and therefore fields of view) and probe currents to maximize writing performance in an EBL process. The issue is that, when changing either the probe current or magnification, the field of view will likely be shifted away at least slightly from where it was centered before changing the parameters. This is particularly a problem when writing features across multiple length scales, as doing so usually requires adjusting the magnification mid-process. In an ideal world, such shifts would not happen. However, it is a common occurrence, at least in SEM-based EBL writing. For example, in the Tescan SEM system used for the EBL in this chapter (see Section 4.3.3.1), it is common for the field of view to shift by 1 - 5 μm along both the X and Y axes of the scan frame when changing parameters. This can (and has, in the past) resulted in failed device writes, as it leads either to features that should overlap instead being separated, or features that should be separate fusing with others. With this in mind, it is a good idea to account for such interlayer shifts during multi-layer writing processes. For example, the NPGS system utilized with our Tescan SEM includes a method to determine the layer offset values when changing parameters (ahead of the writing process) and correct for them (during the writing process).

4.2.1.4 Bi-Layer Resists

The discussion of EBL has thus far focused on the use of a single layer resist. However, it can be advantageous to use a bi-layer resist in some circumstances, as doing so can improve the chances of success of future steps in the device fabrication process. For example, if a resist with higher solubility is first spin coated onto the sample, followed by a resist with a lower solubility, the two resists will respond slightly differently during the development process. Unsurprisingly, more of the bottom resist will dissolve than the top resist layer during development. If done correctly, this will cause side walls of the top layer of resist to extend slightly further out beyond those of the bottom layer of resist, creating an overhang [143]. In reality, the width of the opening in the top layer of resist should more accurately represent the dimensions of the pattern to be written, whereas the portion of the bottom that is dissolved will be slightly larger than the design. As such, the bottom layer is referred to as an “undercut layer”. This is shown schematically in the leftmost subfigure in Figure 4.3, wherein the lighter green layer represents the undercut layer. This differs from the situation where only a single layer of resist is used, wherein the side walls of a developed pattern will be (nominally) completely vertical, with no overhang. The use of an undercut layer is useful in performing a liftoff process, which will be discussed in Section 4.2.2.

4.2.1.5 Charge Dissipation Layers

Performing SEM and EBL on non-conductive samples can be challenging. The reason for this is that, since the sample is non-conductive, incident electrons are not able to be dissipated to the grounded sample stage. As such, excess electrons accumulate on the surface of non-conducting samples and the sample becomes charged. A charged region of the sample will deflect, via the Coulomb interaction, some or all subsequent electrons that would otherwise impinge nearby. If this happens during EBL, the resulting pattern will be distorted, often looking wavy. The solution to this issue usually involves covering the sample with a thin, conducting layer, with Au being a common choice for coating material. This conducting layer is then somehow electrically connected to the sample stage, giving excess electrons a path to ground and allowing them to dissipate from the sample without causing charging. Such a layer is referred to as a “charge dissipation layer”.

4.2.1.6 Troubleshooting and Optimization

There is usually some amount of process engineering that must be done to optimize the EBL process. In general, the finer the features to be written, the more process engineering will be required (with features on the order of 10 nm or less requiring the most). For example, one important factor to optimize is the areal dosage of electrons delivered to the resist during writing (usually expressed in units of $^{\mu C}/_{cm^2}$, where C stands for Coulombs). The optimal value for the dosage depends on a number of other factors, such as the type and thickness of the resist, any heat treatments performed on the resist, the minimum feature size, and even the substrate on which the pattern is to be written. Additionally, the concentration of the developer solution (possibly itself diluted in a carrier solution), temperature of developer solution, and development time also affect the outcome of the EBL process. Other parameters that should be optimized (or at least rationally chosen) include the magnification and beam current of the EBL system, which both affect the spot size of the electron beam.

Due to the sensitivity of the EBL process to the various factors discussed above, it is recommended to perform a series of experiments before actually writing an EBL pattern to a sample or device that one cares about. These experiments should test a variety of parameters (expressed above or otherwise). For best results, the experiments should be performed on a substrate that is as close to that of the final device as possible. Additionally, the experiments should involve writing a test pattern, where the test pattern should include the finest features in the pattern to be written, as these will be the most prone to failure if the process is not properly optimized. One should specifically check the written and developed test pattern for each experiment under an optical microscope. A properly optimized process should reproduce the pattern in the resist exactly. If portions of the pattern appear to be narrower than expected, it could be that the electron dose or the development time are too low. Conversely, if the written features are flared out or even merged together, this could indicate that the electron dosage, electron beam spot size, or development time is too high. A useful tool for checking multiple combinations of electron dosage, spot size, or other EBL system-related parameters is the “dose array”. A dose array is a grid of test patterns, sequentially written on the same sample without removing it from the EBL system, with each pattern testing a different combination of parameters. Using a dose array can provide valuable troubleshooting information during the optimization process and saves time over trying a different combination on a separate sample each time.

4.2.2 The Liftoff Process

The liftoff technique is a technique that can be employed to create patterned metal electrodes on a sample. It is usually performed in conjunction with either electron beam lithography or photolithography, and proceeds as follows. The liftoff process involves first patterning a resist layer, exposing portions of the sample which are to be coated with metal, while leaving the remainder of the sample covered by the resist layer (e.g., as described in Section 4.2.1), shown schematically in step 1 of Figure 4.3. Next, a layer of metal is deposited across the entire sample, covering both the exposed portions of the sample and the remaining resist. However, there should still be portions of the resist exposed around the edges of the sample in the walls of the pattern itself, as shown schematically in step 2 of Figure 4.3. Of course, the remaining resist layer, along with the metal deposited atop it, must be removed before device fabrication can proceed. Thus, the next, and most crucial, step of the liftoff process is to remove the resist and metal layers together. This is accomplished by submerging the sample in a solvent in which the resist layer is highly soluble. The idea is that the solution will dissolve the resist layer underneath the metal while supporting the metal film. Then, any turbulence in the solution should cause the metal film to wash away, leaving behind only the metal which was deposited directly onto the sample itself (shown schematically in step 3 of Figure 4.3).

As one can imagine, it is vital that there be exposed resist for the solvent to dissolve in order for a liftoff process to be successful. There are several strategies that one can take to encourage

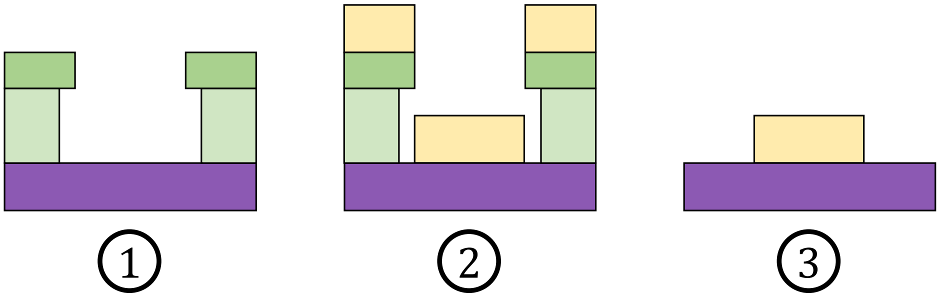

Figure 4.3: Schematic representation of the steps in a liftoff process. Purple denotes the substrate, shades of green represent resists with different solubilities and yellow represents deposited metal.

the success of a liftoff process. First, masking a portion of the sample around the edge of the pattern, perhaps by using tape to create a border around the edge of the top surface of the sample. The masked portion of the resist will not be covered with metal during deposition, thus allowing the solvent to start dissolving the resist from this region and working its way inward. The second strategy is to follow a rule of thumb for liftoff, which dictates that the thickness of the resist layer (or total thickness when multilayer resists are used) should be no less than twice the thickness of the metal to be deposited. This ensures that there will be some resist exposed in the walls of the pattern even after metal deposition. Another option is to use a bi-layer resist which includes an undercut layer (as described in Section 4.2.1.4). The extra space created by the undercut layer will better allow the solvent to work its way underneath the top resist layer and more effectively lift off the metal film. Finally, heating the solvent during the liftoff process can help it more effectively work its way underneath the metal film and produce a cleaner end result.

4.2.3 Photodetector Figures of Merit

It is useful to have standard figures of merit to compare the performance of photodetector devices. One might think to use a simple figure of merit, for example the photocurrent response of two photoconductive detectors, to compare their performance. However, such simple figures of merit lack sufficient detail to make any meaningful comparison between detectors, as the detectors could be different in a number of ways that would affect the photocurrent they produce from a given optical stimulus. Important differences between detectors include device active area and device composition. Additionally, the voltage applied to the detector and the optical power density used during the characterization process of a detector also usually affect such simple figures of merit. With this in mind, multiple other, more robust, figures of merit have been developed. Two such figures of merit are responsivity and external quantum efficiency. Responsivity is a quantity that characterizes the photoresponse of a particular photodetector device per unit optical power of the illumination at the detector. The responsivity is simple to calculate:

$$\mathscr{R} = \frac{I_{ph}}{PA} \quad , \tag{4.1}$$

where $\mathscr{R}$ is the calculated responsivity, I_{ph} is the photocurrent response, P is the areal optical power density, and A is the active area of the device. The external quantum efficiency of a detector represents essentially the percentage of photons that participate in producing the photoresponse of a detector. It is calculated as

$$\eta = \frac{\mathscr{R} h\nu}{e} \quad , \tag{4.2}$$

where e is the elementary charge constant and $h\nu$ is the photon energy for the incident light. Generally speaking, one would like both of these figures of merit to be as high as possible, as this indicates better performance for a device.

4.3 Methods

As in previous chapters, sample preparation and device fabrication for the work described in this chapter was a multistep process. As such, this section will first describe the general design of the photodetector devices. Then, we will discuss the individual processes which were used during device fabrication, before finally providing a description of how these processes were used to produce the final devices.

4.3.1 Device Design

As discussed above, the UV photodetector devices discussed in this chapter utilized a vertical detector design and used exfoliated rather than CVD hBN. As such, the active area of these devices was significantly smaller than the one reported in Chapter 3, since flakes of exfoliated materials are generally orders of magnitude smaller than CVD films, as discussed below. The device design is shown schematically in Figure 4.4. There are multiple sets of components in this design, and each will be discussed in this section.

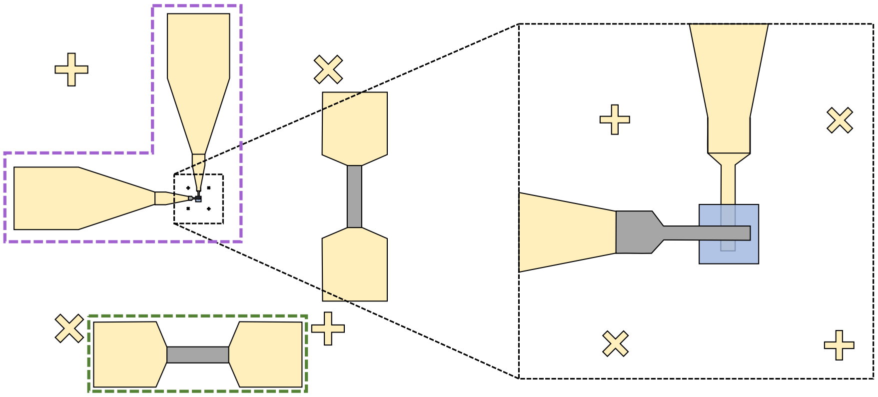

Figure 4.4: Schematic representation of the vertical photodetector design used for the work in this chapter. The left portion of this schematic shows the whole device design, whereas the right portion shows a view that has been zoomed in on the active area of the device. Colored dashed outlines designate separate components in the device design. The yellow regions represent Au/Cr electrodes, gray regions represent graphene, and the blue region represents an hBN flake.

The first set of components are those that comprise the photodetector device itself, and these are outlined with a purple dashed line in Figure 4.4. The photodetector device was composed of three objects. First, the bottom Au/Cr electrode is the vertically-oriented object on the left side of this figure. Second is the hBN flake, shown in the right portion of the figure. Finally, the top electrode is the horizontally-oriented object in the figure. The top electrode was itself composed of two materials. Most of the electrode (including the largest part, which is the contact pad) was made of Au/Cr. However, the portion of the top electrode that is closest to the hBN flake comprised a CVD graphene film. This portion is shown as the gray protrusion in the right portion of the figure. The overlap area between the top and bottom electrodes comprises the active area of the device.

The second set of components in the device design were the alignment markers. These are shown in Figure 4.4 as the "X" and "+" shaped objects. The design has two sets of alignment markers. The first and smallest set of alignment markers are visible in the right portion of the figure and were positioned very close to the active area of the photodetector. These are the primary alignment markers to be used during the alignment routine in the second of the EBL processes used to fabricate the device. More information on alignment processes can be found in Section 4.2.1.2. The second set of alignment markers were larger and are clearly visible in the left portion of the figure. These markers were intended as a backup set of alignment markers in case the primary set were somehow rendered unusable. Additionally, they helped with coarse alignment of the sample.

Finally, the overall device design included two additional sets of contact pads, with each set being connected by graphene strips. Each of these was effectively a graphene resistor and are outlined in green in Figure 4.4. We included these devices to serve as a means to check the continuity of the graphene film after the end of the device fabrication process, discussed below. The idea is that, if the fabrication process were successful, the two electrodes within one of the resistors should be connected to each other, but completely isolated from any other set of contact pads (including the photodetector device and the other resistor). Additionally, if the graphene etching process left the remaining graphene strips (both in the resistors and the photodetector) intact, the graphene resistors should have a finite resistance, depending on the quality of the CVD graphene, but likely on the order of several kΩ.

4.3.2 Sample Preparation

4.3.2.1 Substrate Choice and Cleaning

We chose not to use a SiO_2/Si substrate for the work described in this chapter. The reason for this decision is that we wanted to be able to pre-emptively rule out substrate-related effects (see the second half of Section 3.4 for discussion of such effects) as possible explanations for any photoresponse that we see in the hBN-based UV photodetecotrs described in this chapter. As such, we needed to use a substrate which has a band gap that was much higher than the hBN itself. With this in mind, we used single-crystalline, optical grade, Z-cut quartz (1 cm x 1 cm x 0.5 mm, two-side polished, product number SOZ101010S2 from MTI Corp) as the substrate material. This is essentially the same substrate used in the CVD hBN sample for UV-Vis described in Section 3.3.3, but with half the thickness. Before performing any processing steps, we cleaned the substrate by sonicating it sequentially in acetone, isopropanol, and DI water, followed by blow-drying it with dry nitrogen.

4.3.2.2 Mechanical Exfoliation of Hexagonal Boron Nitride Crystals

For the work described in this chapter, we received several batches of bulk hBN crystals from Kenji Watanabe and Takashi Taniguchi, researchers at the National Institute of Materials Science in Tsukuba, Japan. Crystals of similar provenance have been used in many research studies over the years (e.g., [85, 144–146]). Specifically, we used crystals from batch M912 in this work.

We used mechanical exfoliation to prepare thin films of hBN for use in the photodetectors discussed in this chapter. As discussed in Section 2.3.1.1, pre-cleaving bulk crystals is an important first step in the mechanical exfoliation process, as the outer surfaces of most bulk crystals tend to have many facets, leaving little to no sufficiently flat area that is suitable for high-quality exfoliation. With this in mind, we cleaved the bulk hBN source crystals multiple times before assembling a photodtector device. The first two cleaves involved using thermal release tape (from

Graphene Supermarket, as discussed in Section 2.3.1.1). After these initial cleaves, we transferred the hBN flakes to thin poly(dimethylsiloxane) (PDMS, product # PF-40/17-X4, obtained from Gel-Pak) films. We used PDMS for this because it facilitated the targeted transfer process, as will be discussed in Section 4.3.3.5. This technique leveraged the viscoelastic properties of PDMS, which make it so that the degree of adhesion between the PDMS surface and anything contacting it is dependent on the speed with which the two surfaces are separated [147, 148]. Since we needed stronger adhesion between the PDMS film and the hBN flakes, we peeled the PDMS away from its counter-adhesive (either tape or other PDMS) quickly (the whole peel taking about 200 - 500 ms). To transfer the flakes to the PDMS we simply used a PDMS film as the second adhesive during the third cleave (with the other piece being one of the pieces of tape with hBN flakes on it). We specifically did not thermally release the flakes from the thermal release tape, as we wanted to avoid tape residue as much as possible. We then used a second piece of PDMS for subsequent cleaving. Thus, performing about six cleaving steps (i.e., peeled the adhesives apart six times), resulted in multiple sheets of PDMS with fields of flakes with thicknesses ranging from bulk to several nanometers and with varying lateral dimensions.

4.3.2.3 Locating Suitably-Thin Hexagonal Boron Nitride Flakes

After mechanical exfoliation, we needed to select a few candidate flakes that could be used in producing a photodetector device. For the vertical device, we specifically wanted flakes that were about 10 nm thick and without any cracks. However, finding such thin flakes using an optical microscope proved challenging for three reasons. First, the lateral dimensions of exfoliated flakes tend to decrease with thickness. Second, such thin hBN flakes are essentially transparent to visible light (as discussed in Sections 3.1 and 3.4). Finally, there is very little optical contrast between ultra-thin hBN flakes and PDMS substrates. Nevertheless, we located multiple candidate flakes using optical microscopy. Before using any of the candidate flakes, however, we used atomic force microscopy (AFM) to confirm their thicknesses, with the hBN samples remaining in-place on the

PDMS film. This AFM work was performed using a Digital Instruments Dimension 5000 AFM, operated in tapping mode with amplitude feedback, equipped with a Si AFM probe (model PPP-NCHR, obtained from Nanosensors). After locating several flakes of suitable size and thickness, we cut the section of PDMS holding the flakes away from the rest of the PDMS sheet and proceeded with the fabrication process.

4.3.3 Device Fabrication Sub-Procedures

4.3.3.1 Electron Beam Lithography: The Process

We used an EBL process to pattern the electrodes for our photodetectors. The reason for choosing EBL over another patterning technique (such as shadow masking) is that the lateral dimensions of the exfoliated flakes produced using the process described in Section 4.3.2.2 were too small (about several microns) for other types of lithography or too variable to justify designing and ordering custom photomasks. The general process is described in Section 4.2.1, while the specific details of the process are given in this section.

We chose to use a bi-layer resist for patterning the electrodes in this work to take advantage of the benefits of an undercut layer (described in Section 4.2.1.4). We deposited each resist layer individually using a spin-coating process. This involved pipetting about 500 μL of the appropriate resist solution onto the sample to be patterned while the sample was mounted on the vacuum chuck of a spin coater. Immediately after pipetting, we engaged the spin coater, which had been programmed to rotate the sample (with resist solution on top) at a speed of 4000 RPM for 1 minute. During this process, the resist solution was forced to spread out evenly across the surface of the sample, with excess solution being flung off by centripetal force, ideally yielding a layer of resist with a uniform thickness. After spin coating, we heated the freshly-coated sample on a hot plate set to 180 °C for 5 minutes to drive off any remaining solvent from the resist layer. The first resist layer applied in this way was the undercut layer, which comprised a copolymer of PMMA: poly(methyl methacrylate/methacrylic acid). We used a commercially-available solution consisting of 9% copolymer dissolved in ethyl lactate. The trade name of this solution was "MMA(8.5)MAA EL9" (obtained from MicroChem). Spin coating this solution at 4000 RPM should have resulted in a film that was approximately 400 nm thick (according to the spin curves provided by the manufacturer). The second layer of resist was PMMA, and was also prepared using a commercial solution, consisting of 2% PMMA dissolved in anisole (trade name "495 PMMA A2", obtained from MicroChem). Spin coating this solution at 4000 RPM should have produced a film approximately 60 nm thick. The final step in preparing for electrode patterning was to deposit a Cr charge dissipation layer atop the bi-layer resist. This was required because the quartz substrates we used were insulating, and therefore charging would have been an issue during EBL if we had not deposited a dissipation layer (see Section 4.2.1.5 for more discussion). The process for this was almost the same as the metallization process described in Section 2.3.1.1, with the primary difference being that we did not deposit the Au layer described in that section. In brief, we loaded the resist-coated sample into a thermal evaporator, pumped the chamber down to base pressure, outgassed the Cr source, and then deposited a 5 nm thick layer of Cr atop the resist.

Having prepared a resist layer and charge dissipation layer atop the sample, the next step was to prepare and optimize the EBL system. To this end, we loaded the coated sample into the working chamber of an SEM (a Vega II system, manufactured by Tescan) equipped with a nanopositioning stage (manufactured by SmarAct GmbH) capable of positioning and repositioning the sample to within 100 nm or less. This SEM system was a thermionic emission-based SEM. As a result, the ultimate resolution of the microscope was lower than that of a field effect-based system, but the beam current tended to be much more stable over the course of hours (rather than minutes), which is desirable for EBL writing. After loading the sample, we evacuated the chamber to a pressure less than $1 \cdot 10^{-5}$ Torr by means of a mechanical vacuum pump. Next, we optimized the electron beam. This involved first "degaussing" the electromagnetic lenses in the column of the SEM to remove undesirable remnant magnetic fields that may be present in the lens. Next, we engaged an automatic routine during which the SEM system adjusted the filament heating power, electron gun centering, and tilt to achieve the most stable beam current. Following this, we imaged a reference sample, which was either a transmission electron microscope sample grid with Au nanoclusters deposited on it or, when higher resolution was required, a “gold on carbon” sample. While imaging the reference sample, we adjusted other SEM imaging parameters, such as aperture centering and stigmation to assess and optimize the quality of the beam. When the beam was sufficiently optimized, we then moved to a Faraday cup which had been integrated into the sample stage. We connected this Faraday cup to a Keithley 6485 picoammeter. After increasing the magnification such that the entire field of view was within the Faraday cup, the picoammeter could be used to measure the beam current. In this way, we measured the beam current corresponding to a number of different probe current settings, particularly those that would be used during the EBL writing process. Finally, before proceeding with the writing process, we measured the offset of the field of view produced by changing microscope parameters, using features on the reference sample. As discussed in Section 4.2.1.3, this is very important for writing devices with fine features. More details regarding this process will be given later in Section 4.3.3.3.

The next step in the EBL process was to perform coarse alignment of the sample. To accomplish this, we moved the stage such that the desired location of the sample (where the pattern should be written) was roughly centered in the field of view of the microscope. Next, we performed a series of increasingly fine rotations and translations of the stage, also using increasingly higher magnification, until any reference points (such as alignment markers) had roughly the correct orientation relative to the field of view and such that the field of view was roughly centered on the physical location corresponding to the origin of the design to be patterned. Generally, the coarse alignment wasn’t strictly necessary for writing the first pattern in the device (as there were no alignment markers to align to). However, we found that roughly aligning the first layer written on a substrate such that the edges of the substrate were relatively square with the field of view helped to speed up future coarse alignments. After coarse alignment, we engaged the electrostatic beam blankers in the SEM column and switched the system to external control mode.

After all the preparation work described above, we could finally write the pattern into the resist layer. The writing process was facilitated by a dedicated hardware and software suite called the Nanometer Pattern Generation System (NPGS). This suite was designed to take a pattern file (designed using one of several computer aided design tools, such as DesignCAD), generate a raster pattern for the electron beam to 'draw' the pattern in the resist, and then control both the beam and SEM parameters to execute the pattern writing process. As such, we had previously made design files of the patterns to be written and set up an NPGS run file with the desired parameters for writing. More details regarding the specific parameters we used will be included in Section 4.3.3.2. After setting up all required files, we initiated the writing process through the NPGS software. Thereafter, the NPGS hardware and software took complete control of the SEM (including adjusting the microscope's magnification and probe current) to affect the writing. After the writing process, we turned off the electron beam, waited about 5-10 minutes for the filament to cool, then vented the chamber and retrieved the sample.

As discussed in Section 4.2.1.1, the final step in the EBL process was to develop the pattern. However, our EBL process used a charge dissipation layer, which needed to be removed before we could develop the pattern. To this end, we immersed the written sample in a room temperature Cr etching solution (Chromium Etchant 1020, produced by Transene Inc.) for 1 minute before rinsing the sample for another minute in a clean, DI water bath. Next, we prepared our developer and stopping solutions. The developer solution consisted of one part (usually about 10 mL) of methyl isobutyl ketone (manufactured by MicroChem) diluted in three parts (usually 30 mL) of isopropanol (semiconductor grade or 99.5 % pure, purchased from VWR) in a glass beaker. We used about 40 mL of isopropanol as the stopping solution. To develop the pattern, we immersed the sample with EBL pattern in the developer solution, holding it upright with stainless steel tweezers and swishing it, for 1 minute. Immediately afterward, we immersed and swished the developed sample in the stopping solution and then blow-dried it with dry nitrogen. Finally, we used an optical microscope to evaluate the quality of the written pattern. The optical contrast between the (transparent) quartz substrate and the resist was rather low, but still sufficient to see the outline of the written pattern. If the pattern was of sufficiently high quality, we proceeded with the sample fabrication process. If not, we removed the resist layer and started the EBL process over again.

4.3.3.2 Electron Beam Lithography: The Design and Writing Parameters

Our designs required writing a pattern with features ranging over several order of magnitude. Specifically, the finest features were on the order of several microns, whereas the largest features occupied a 1.0 mm x 1.0 mm area. For this reason, writing the entire pattern in one field of view (i.e., at one magnification setting) would not have been possible. This is because we would have had to use a magnification suitable for the largest features, which means that the SEM system would likely not have had fine enough control of the beam to perform sub-micron positioning of the beam. Additionally, if we had used the same probe current (to which the spot size is tied), it would have taken an exceedingly long time to write the pattern. Therefore, we wrote our patterns using three different sets of parameters, breaking the design up into ‘fine’, ‘intermediate’, and ‘large’ EBL layers based on their feature size and spacing. These EBL layers are highlighted with different colors in Figure 4.5. The parameters used for each layer are shown in Table 4.1. For clarity, we note that the usage of “layer” in this case is the conventional parlance used in discussions of lithography processes. As such, the term is intended to mean essentially a grouping of features to be written simultaneously. This is in contrast with the perhaps more common usage, where a layer might indicate all features involved in a lithography process as a whole. For example, a single layer of gold to form the contacts is deposited, forming a layer of the device, but the EBL process would split the design up into multiple EBL “layers”.

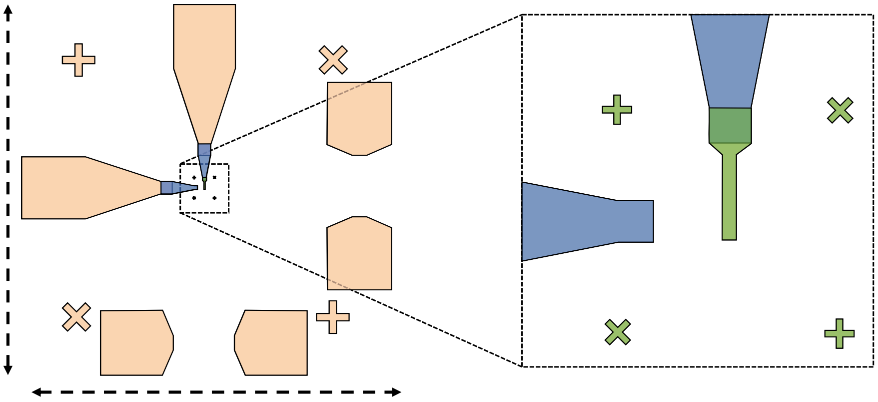

Figure 4.5: Schematic highlighting the different layers used during the EBL process for patterning the Au metal electrodes.The orange overlays denote the “large“ features, the blue overlays the “intermediate” features, and the green overlays the “fine” features. The dashed lines with arrowheads are intended to act as scale bars that are 800 μm long.

Table 4.1: EBL writing parameters

Pameter	Parameter Value Per EBL Layer		
	Fine	Intermediate	Large
Magnification	1000 X	500 X	125 X
PC	16	7	3
Approx. Spot Size (nm)	24	163	406
Approx. Beam Current (pA)	11	702	5184
Electron Dose ($\mu C/cm^2$)	175	175	175
Grid Point Spacing (nm)	7.2	50.4	57.6

4.3.3.3 Electron Beam Lithography: Determining the Origin Offsets

As discussed in Section 4.2.1.3, minimizing offsets due to changing of EBL system parameters is important to ensure the success of EBL writing. We used a tool provided as part of the NPGS software to assist us with this during the work described in this chapter. The tool was simply a design file, which contained two alignment windows and a cross-hair, and a run file. The run file was configured to perform two sets of alignment routines (the procedure for performing an alignment routine is conceptually described in Section 4.2.1.2), each with one set of SEM system parameters (particularly magnification and probe current). The first alignment routine allowed the user to move the cross-hair over the alignment window (which was actually a continuously-refreshing SEM image of a portion of the sample), recentering the window on the cross-hair if necessary. The goal of this first routine was to find a reference feature on the sample and center it in the alignment window (such that the cross-hair was overlaid directly on the feature).

After this process was complete, the second alignment routine started scanning the second alignment window. In particular, the second alignment window should have been centered at the same coordinates (relative to the field of view) that the first alignment window was centered at (at the end of the first step). In principle, one would prefer that the second alignment window (with accompanying cross-hair) be exactly centered on the reference feature, even though the scanning parameters were adjusted. As mentioned above, however, this is not likely to be the case, as changing the scanning parameters will almost certainly cause a shift. With this in mind, the cross-hair in the second alignment routine could be moved around the alignment window (without recentering the window) so that it was perfectly centered on the reference feature. The offset measurement tool then reported the distance between where the reference feature was in the first alignment routine and where it was in the second window. This distance, reported as X and Y components, was the measured offset. NPGS can be configured to automatically account for these offsets, once they have been measured, by entering the measured offset values in the “origin offset” field when configuring a run file. It is good practice to enter the previously-measured offset values in the offset checking tool and perform another offset check, as just described. If the measured origin offsets are correct, the second alignment window should be perfectly aligned with the reference feature chosen during the first routine without having to move the cross-hair at all.

4.3.3.4 Metal Electrode Patterning

We used a liftoff process (discussed conceptually in Section 4.2.2) to fabricate the metal electrode for each of our hBN-based UV photodetectors devices. This process started with performing an EBL process (as described in Section 4.3.3.1) to define a pattern in a resist layer in the shape of the electrode and contact pads. We then deposited 50 nm of Au with a 5 nm Cr sticking layer using the thermal evaporation process described in Section 2.3.1.1, except that we did not use a shadow mask in this case (the EBL-patterned resist layer served as the mask). This resulted in the Au/Cr being blanket-deposited over the whole sample. We then prepared a liftoff solution consisting of undiluted N-methyl-2-pyrrolidinone (trade name “Remover PG”, purchased from Kayaku Advanced Materials, Inc.) by heating it to about 70 °C in a glass beaker. After the solution reached temperature, we immersed the metallized sample in the solution for about 30 minutes. After this immersion, we could see the Au/Cr film either completely removed or bubbling where the PMMA had been dissolved. Any remaining metal that had originally been deposited atop the resist could then be dislodged by gently swirling the contents of the beaker. When the metal had been dislodged, we transferred the sample to a second beaker with a fresh aliquot of Remover PG solution, whereupon we let it sit for another 30 minutes to remove any remaining PMMA residue and loose metal. Finally, we removed the sample, which now had patterned metal electrodes, and dipped it in room temperature isopropanol to rinse away any Remover PG residue, followed by dipping in DI water to rinse away isopropanol residue, followed by blow-drying with dry nitrogen.

4.3.3.5 Targeted Transfer

We utilized a targeted transfer (i.e., a “dry transfer printing”) process to transfer candidate hBN flakes onto pre-patterned device electrodes during the sample fabrication process for the devices discussed in this chapter. The goal of this process was similar to the targeted transfer process described in Section 2.3.1.2, but the means of accomplishing it were slightly different. The starting point for this procedure is essentially the work described in Sections 4.3.2.2 and 4.3.2.3. This is to say that candidate hBN flakes should have already been selected, and should still be on the PDMS films used to cleave them. The first step, then, in the targeted transfer process is to place the PDMS film on one face of a glass slide near one end, pressing the bottom side (where the hBN is stuck to the top side) of the PDMS into the slide. The back side of the PDMS film should also be adhesive for this to work. Then, we mounted the glass slide, with PDMS and hBN upside down, into the jaw of a micromanipulator assembly. In this way, the hBN-covered surface of the PDMS was the lowest point of the slide/PDMS, facing downward without any obstructions. Next, we secured the sample onto which we wanted to transfer an hBN flake onto the translation stage of an optical microscope (a probe station in our case) using tape. It is important that the translation stage either have an integrated sample heater or be fitted with one before securing the sample to it. Following this, we moved the whole micromanipulator assembly so that the PDMS film was directly over the secured sample. The final step in this phase of the targeted transfer process was to ensure that both the hBN flake to be transferred and the target location to transfer it to were both aligned with the optical axis of the optical microscope. This is where one of the reasons that we chose to exfoliate the hBN crystals on PDMS comes into play. The reason is that PDMS is transparent in the visible range, so a user can see through it during the transfer process.

With the sample and hBN secured and roughly aligned, the main part of the targeted transfer process could proceed. The next phase of the transfer process involved bringing the PDMS ever closer to the sample. During this process, the user made slight adjustments to the positioning of the hBN flake (using the micromanipulator), both in the vertical and lateral directions, to ensure that the flake remained directly above the target location on the sample. The depth of field of most optical microscopes is too shallow to sharply resolve both the sample surface and the hBN flake simultaneously (at the magnifications required to see most ultra-thin exfoliated hBN flakes), so the user needed to switch between focusing on the sample and the hBN flake during this process. As the hBN flake got close to the surface of the sample, the user may notice that some portion of the PDMS contacts the surface of the sample before the hBN does. In principle, this is the desired behavior, as the transfer process involved a peeling motion, which is not easy to facilitate if the hBN flake is the first thing to touch the sample. However, it is important that the PDMS not contact the sample too soon before the hBN flake would do so. If the PDMS contacts the sample too soon, it will limit the degree to which the user can laterally adjust the position of the hBN flake and cause the transfer process to fail, with the hBN flake missing the target location. If the PDMS does contact the sample too soon, the user should raise the slide assembly to break contact, and then adjust the angle of the PDMS film to ensure that it does not contact the sample so soon. The rest of this phase of the transfer process involves adjusting and lowering the hBN flake until it comes into contact with the desired location of the sample. Additionally, the PDMS around the flake should also be in contact with the sample.

The final phase of the transfer process involved two steps. The first step was to heat the sample, hBN and PDMS to around 100 °C. This step served two purposes. The first purpose was to promote adhesion between the hBN flake and the target substrate by driving off any moisture at the interface between the two. The second purpose was to soften the PDMS film slightly. The final step to the transfer process was to peel away the PDMS from the sample in a controlled manner. It iwa extremely important that the peeling process be done very slowly. The reason for this is that, as mentioned in Section 4.3.2.2, PDMS is a viscoelastic material. As such, when peeling PDMS away from a surface, the strength of adhesion between the PDMS and the another surface during the peeling process is dependent on the speed at which the two are peeled apart. For the targeted transfer to work, the hBN flakes needed to be released from the PDMS film and be left behind on the target substrate. This meant that the hBN-substrate interaction must be stronger than the hBN-PDMS interaction. With this in mind, the PDMS must be peeled away from the surface very slowly, over the course of at least several minutes. Additionally, we found that we obtained the best transfer results when we let the PDMS slowly peel up from the substrate completely before retracting the PDMS. If everything went well, the hBN should have been left behind in the desired location on the substrate, and it should be ready for further processing.

4.3.4 Device Fabrication

As stated previously, the process that we used to fabricate the hBN-based photodetectors discussed in this chapter involved many sub-processes, and it is these sub-processes that have been discussed thus far. However, this section will detail the process of combining all of these sub-processes to perform the full sample fabrication procedure. As discussed in Section 4.3.2.1, we used single-crystal quartz as the substrate for our detectors. The very first task we did was to cleave hBN flakes using mechanical exfoliation and identify candidate flakes that were as thin as possible (described in Sections 4.3.2.2 and 4.3.2.3). This process also involved measuring the thickness of each candidate flake using AFM, performed directly on the PDMS substrate that we used to exfoliate the flakes. Thus, the result of the first phase of the device fabrication process was having two flakes of hBN on PDMS ready to be transferred. We note here that most of the next paragraph will detail the initial fabrication process for a single photodetector device. However, we made two detector devices for the work described in this chapter, with both devices being fabricated on the same substrate.

The second phase of the fabrication process involved depositing the bottom electrodes of the photodetector device and transferring an hBN atop the electrode. The first step in accomplishing this was to pattern the metal electrodes needed for the device. This included all metal electrodes shown in Figure 4.4. To this end, we used EBL, thermal evaporation, and liftoff to create patterned metal electrodes. The details of these processes were discussed in Sections 4.3.3.1 and 4.3.3.4. We note here that, since we fabricated two photodetector devices on the same quartz substrate, our electrode fabrication process involved repeating the EBL process a second time after the first write. We did this without removing the sample from the SEM, simply moving to a new location on the substrate after writing the first pattern. We proceeded with the development process, *et cetera*, only after the second EBL write. For the remainder of the device fabrication process (including the rest of this paragraph) we performed each task twice (once for each device). Having patterned the Au/Cr electrodes and contact pads, we moved on to transferring an hBN flake to the device. We did this using the targeted transfer technique described in 4.3.3.5. In particular, we transferred one hBN flake such that it covered the very end of the elongated protrusion comprising the bottom electrode of each device, as shown in Figure 4.4. Before proceeding with the final phase of device fabrication, we used AFM to image the hBN flakes transferred onto each device. We did this specifically to check for any cracks in the hBN films and to determine the flake thicknesses.

The last fabrication-related task was to create a patterned graphene top electrode for each device. To this end, we used the wet transfer process discussed in Section 3.3.2.1 to transfer monolayer CVD graphene over the entire substrate, covering both devices. Most of this graphene needed to be removed, leaving only the graphene in the desired locations (namely the top electrode of the photodetector device and in strips in the graphene resistors). The excess graphene removal process began with using EBL to create an etch mask. This EBL process was almost identical to that used in patterning the metal electrodes, in that it used the same bi-layer resist (with charge dissipation layer), the same EBL writing parameters and the same development process. The main difference was the pattern written into the resist. In particular, we needed to leave the resist intact where we wanted the graphene to remain. As such, we left these locations unexposed by the electron beam during the writing process, while exposing every other region of the sample. Thus, when we developed the pattern, most of the resist covering the sample was dissolved. The remaining resist formed an etch mask whose purpose was to protect the desired graphene from being removed during etching. The EBL pattern used to create the etch mask is shown schematically as the gray shaded regions in Figure 4.6. The unshaded regions in this figure represent the portions of the resist that remained on the sample after patterning, forming the etch mask. Having patterned the etch mask, we used reactive ion etching (with an O_2 plasma, as described in Section 3.3.2.3) to remove the exposed graphene from the surface of the sample. After etching, we dissolved the remaining resist by sequentially immersing the sample in acetone, isopropanol and DI water baths, followed by blow-drying with dry nitrogen. The final step in device fabrication was to mount the finished

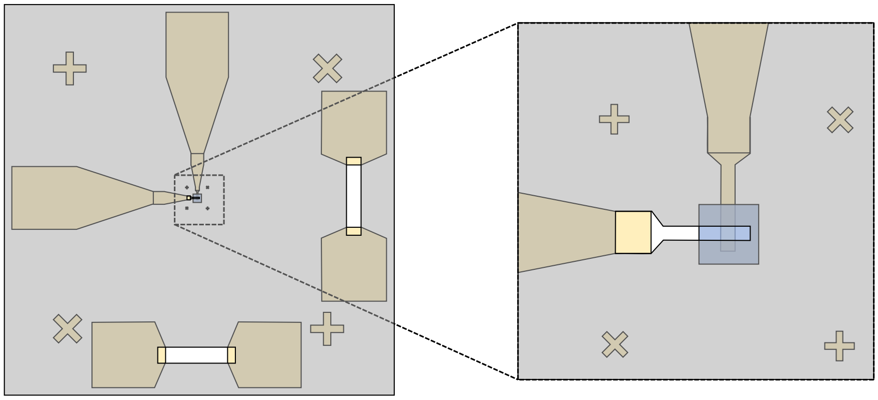

Figure 4.6: Schematic showing the etch mask used to pattern the graphene. The gray shaded regions represent the portion of the device area exposed during the EBL process.

devices to a leadless chip carrier (LCC) and wire bond the contact pads on the devices to those on the LCC. The process for accomplishing this was described toward the end of Section 3.3.2.5.

4.3.5 Device Characterization

The measurement process that we used to characterize the optoelectronic performance of the devices discussed in this chapter were similar to those described in Section 3.3.4. We performed primarily photoconductive measurements, rather than photovoltaic measurements, however. There are three main differences between the measurement setup used in Chapter 3 and in this chapter. These differences are discussed in each of the next three subsections.

4.3.5.1 Voltage Source and Current Measurement

As in Chapter 3, we used a Keithley 2400 SourceMeter (SMU) to supply the bias voltage to the photodetector devices via the LCC and its socket. However, we found that the currents through the devices were usually on the order of tens to hundreds of picoamperes, even at higher voltages. The SMU was not well-suited to measure such small currents with a high degree of accuracy. Instead, we used a current-to-voltage preamplifier manufactured by DL Instruments (model 1211).

This preamplifier featured a variable input gain, with sensitivities ranging from $1\ {}^{mA}\!/_{V}$ to $10\ {}^{pA}\!/_{V}$. Additionally, the preamplifier had an integrated battery, which enabled it to operate without being plugged into an outlet. This helped to reduce the noise in the measured currents. We measured the output voltage from the preamplifier, which was proportional to the measured current (the selected sensitivity was the proportionality constant), using the Keithley 2000 Multimeter (MMU). We used custom LabVIEW VIs to control the bias voltage and record the measured current during experiments.

4.3.5.2 Noise Reduction

Our initial measurements of the photodetector devices failed to resolve the changes in current through our device (on the order of picoamperes) due to the presence of excessive noise. Through several experiments, we determined that several factors contributed to the measured noise. First, line noise (60 Hz and higher-order harmonics thereof) was introduced into the measurements when the current sensing equipment (SMU or preamplifier) was plugged into an outlet. Running the preamplifier using its internal battery effectively solved this issue. Second, we found that the wires we had been using to measure the current signal, along with the devices themselves, were acting as antennae. As such, they could pick up noise from stray electromagnetic signals (such as those from nearby electronic devices or motors). Eliminating this noise required reworking our measurement setup somewhat. Specifically, we made two changes to shield the setup from the noise. First, we switched to using co-axial cables with BNC terminations, with the signals to be measured passing through the inner core of the cable, while the outer sheath was kept at ground. This effectively shielded the inner core, preventing it from picking up noise from external sources.

The second change we made to the setup involved shielding the devices themselves. To do so, we machined two versions of metal housings in which we could mount the device, LCC, and socket. The walls of the housings were grounded, to shield the devices mounted inside from picking up external noise, in the same way as with the co-axial cables. The electrical interfacing (i.e., supplying voltage and measuring current) was done through the center pin connection of a BNC connector mounted to the housing. The first version of the housing had two input BNC ports, and one output port. The idea with this design was that we could have two devices connected to input/output ports simultaneously, and could therefore sequentially measure the response of both devices without having to swap any BNC cables to change the device to be measured. The second version of the housing had only one set of connections. In addition to the BNC connectors, the housing had an opening machined in the front face to allow the mounted devices to be illuminated. We machined this opening to be the same size as the sample cavity in the LCC, as making it much larger would likely have decreased the noise shielding efficacy. Additionally, we designed and 3D printed several custom mounting brackets using polylactic acid, an electrically insulating polymer. These mounting brackets allowed us to mount the LCC socket inside the metal housing while keeping the socket, LCC, and sample electrically isolated from the housing itself. Using this configuration, we were able to reduce the noise in the measurements to a sufficient extent that we could resolve changes in current on the order of picoamperes. One final important note regarding the noise reduction strategy is that the outer sheath of the co-axial cable and the device housing were grounded to the instrument ground of the SMU via its low voltage output terminal. Maintaining a single ground in the circuit was important, as having multiple ground caused ground loops to form, which added extra noise to the measurements.

4.3.5.3 Light Source

In addition to the above changes, we also used a different light source for the work described in this chapter compared to those discussed in Chapter 3. Specifically, we used an optical parametric oscillator (OPO), which was capable of generating light with variable wavelength in the range of 192 nm (6.5 eV) to 2750 nm (0.5 eV). OPOs are pulsed light sources which can output high-intensity, semi-coherent beams without needing to be focused, giving them an advantage over traditional lamp-based sources (such as a deuterium lamp). The system we used was a model

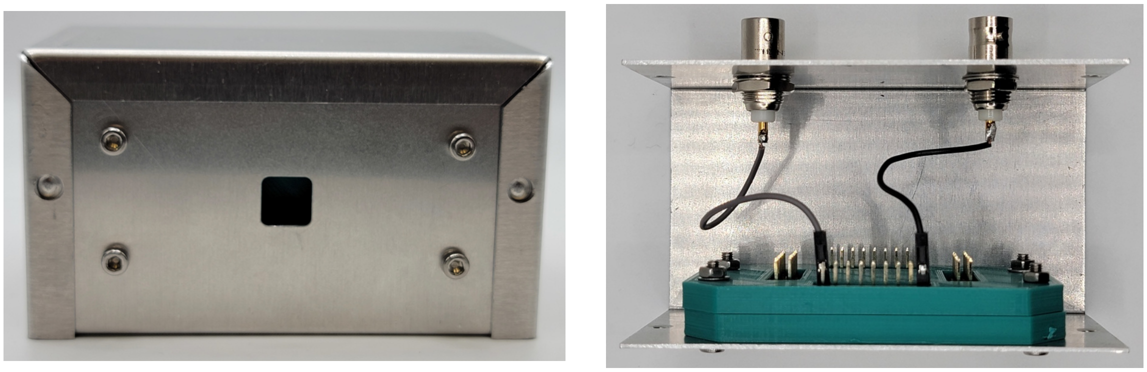

(a) Front face.

(b) Internal view.

Figure 4.7: Device housing for noise reduction.

Horizon-I, manufactured by Continuum, pumped by a frequency-doubled Nd:YAG laser (a Surelite 110 laser, output wavelength of 532 nm). The output of the OPO was pulses of light with a pulse width of about 15 ns and at a repetition rate of 10 Hz (i.e., one pulse every 100 ms).

The optical characterization process involved acquiring time series data of the current through the device, with the device held at a constant voltage, similar to the process used to acquire the data shown in Figure 3.12a. At the beginning of a measurement process we ramped the voltage from 0 V to the desired voltage and then started recording the resulting current, with the device positioned in the beam path of the OPO, but with the output from the OPO occluded. We recorded data in this configuration for between one and two minutes to acquire a dark current background against which we could compare any measured photoresponse. Following this dark period, we opened the output port of the OPO, exposing the device to UV light. In this way, we alternated between periods of illumination and darkness, with each period lasting for approximately 30 - 60 seconds.

We used a handheld laser power meter to measure the output optical power of the OPO. The power meter that we used (a model 843-R meter equipped with a model 818-UV sensor, both sold by Newport Optics) had a measurement bandwidth from 200 nm to 1100 nm. We determined the optical power at a distance of about 122 cm from the output port of the OPO, which is where we generally placed the sample during measurements. The power meter sensor had an aperture with a diameter of 3.0 mm. After measuring the optical power incident on the detector through the aperture, we divided the measured power by the area of the aperture to determine the optical power density of the OPO beam at several wavelengths.

4.4 Results and Discussion

The sample fabrication procedures described above resulted in two vertical, exfoliated hBN-based photodetector devices. As previously mentioned, both devices were fabricated on a single substrate, with one device each aligned slightly right and left of center of the substrate (with the device orientation being shown in Figure 4.6. For convenience, we will refer to the two devices as “DevA” for the left device and “DevB” for the right. Figure 4.8 shows several types of microscope images that provided visual feedback used during the fabrication process, with each sub-figure representing one of the devices. We took the AFM images, shown in the rightmost panel of each sub-figure, after transferring the hBN flakes atop the bottom Au/Cr electrodes (this process was described in Section 4.3.3.5). Using these images, we assessed the thickness and continuity of each flake in the vicinity of the electrodes, and this information guided the device planning process regarding exactly where to position the graphene top electrodes, what the lateral dimensions of the electrodes should be, and what shape they should be to yield the largest-area devices possible. These characterizations in particular were vital to the fabrication process, as we were able to avoid a crack in the hBN flake for DevA (indicated by the white arrow in Figure 4.8a) which, if we had patterned the graphene top electrode over, would have immediately caused a short circuit in DevA, thus ruining the device. The black outlined region in each AFM image denotes the area in which we decided to fabricate the graphene top electrodes. We acquired the optical microscope images in Figure 4.8 after the graphene etch mask patterning process (described in the last paragraph of Section 4.3.4). These images show an outlined region extending from each of the left electrodes and reaching over the transferred hBN flakes. These outlined regions are the portions of the EBL resist layer left behind after development and served as the protective layers to preserver the graphene underneath. The remaining regions of the (exposed) graphene were thereafter removed using RIE. A summary of the device dimensions is shown in Table 4.2.

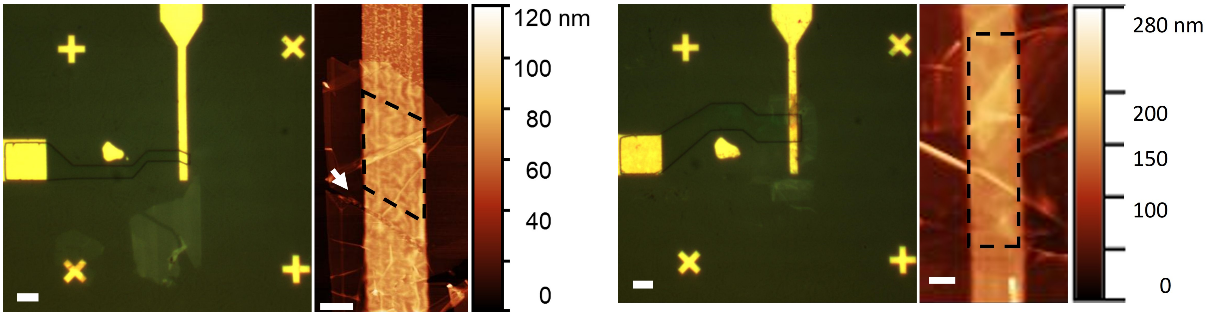

(a) Device A (b) Device B

Figure 4.8: AFM and optical microscope images of photodetectors. Left panel of each subfigure: Optical microscope image of devices showing graphene etch mask. Right panel of each subfigure: AFM image of hBN flake transferred atop electrode. The scale bars in the AFM images represent a line 2.0 μm long, whereas they are 10 μm long in the case of the optical microscope images.

Table 4.2: Dimensions of the fabricated exfoliated hBN UV photodetectors. "W.A." is an abbreviation for "weighted average".

Device	A	B
Length (μm)	5.6	13.0
Width (μm)	3.5	3.5
Area (μm^2)	19.6	45.5
Thickness, Min (nm)	6.0	10
Thickness, Max (nm)	7.5	50
Thickness, W.A. (nm)	6.4	29.3

The first characterization that we performed on our photodetector devices was measuring a series of IV curves. Initial IV curves of DevA acquired shortly after the conclusion of the device fabrication process are shown in Figure 4.9a. We see from this IV curve (averaged from four separate acquisitions) shows an approximately linear dependence on applied voltage at low voltages (below about 3.0 V), as one would expect from a tunneling device (see Section 2.2.2 for a discussion of this). Additionally, we see that, above about 4.0 V, the effective conductance of the device had increased dramatically from the low-voltage regime, suggesting that a separate conduction mechanism dominated at higher voltages. The changeover between the two conductance regimes occurred in the voltage range between about 3.0 - 4.0 V, corresponding to an approximate electric field strength of 4.7 - 6.3 $^{MV}/_{cm}$ (calculated by dividing the applied voltage by the weighted average hBN thickness). This is consistent with the turn-on voltage observed for similar devices reported in the literature [149]. This suggests that, at least initially, our hBN photodetector devices behaved as expected.

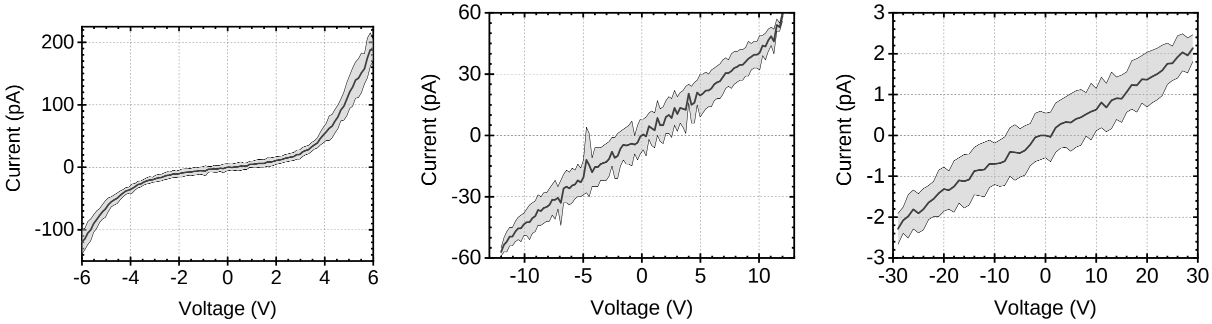

(a) Post-fabrication, DevA

(b) Post-UV, DevA

(c) Post-hiatus, DevB

Figure 4.9: IV curves of photodetector devices acquired at various stages of testing.

Having confirmed the expected performance of DevA, we moved on to performing initial characterizations of the photoresponse of DevA. Our intention was to measure the IV curve of DevA under illumination by a readily available UV source, so we could compare IV curves acquired with and without illumination (similar to the comparison made in Figure 3.11). To this end, we illuminated DevA with the germicidal lamp, whose primary optical output is at 365 nm (referred to as “UV Source 2” in Chapter 3). Our expectation, given the discussion regarding conduction mechanisms provided in the second half of Section 3.4, was that we would see a modest increase in the magnitude of the current with the device illuminated with light below the band gap of hBN, likely due to hot carrier effects. However, this is not what we observed. An IV curve acquired with the DevA illuminated by UV Source 2 is shown in Figure 4.9b. It is evident that the conducting character of DevA changed significantly as a result of the exposure to UV light, with the IV curve becoming essentially linear out to voltages double the previously-observed turn-on voltage. At this point in the testing, we refrained from measuring the IV curve of the device at voltages beyond those shown in Figure 4.9b, the upper limit shown therein (12 V) was already well into the voltage range where dielectric breakdown of the hBN could start to occur (beginning at around 12 $^{MV}/_{cm}$, corresponding to about 7.7 V for DevA) [106]. Nevertheless, we note that the current measurements discussed in this paragraph are comparable to the dark current measured in a graphene-hBN-Au device reported in the literature [140].

One possible explanation for this change in behavior is that the conductivity of the graphene electrode itself could have been affected by exposure to the UV light. One mechanism to affect such a change in conductivity is that of photodesporption, an explanation of which follows. When atmospheric gas molecules (O_2 and H_2O in particular) adsorb onto a sheet of graphene, they effectively hole-dope the graphene, increasing its conductivity [150–152]. However, when light with enough photon energy (usually in the UV range) impinges on the graphene, the energy from the photons will cause the gas molecules to desorb over time, decreasing the surface dopant concentration and the conductivity along with it. The rate at which desorption occurs depends on the optical power of the incident light [151]. With this in mind, it is possible that exposure to UV Source 2 could have caused atmospheric gas molecules (or remnants from the fabrication process) to desorb and decrease the conductivity of the top electrode in our device. However, we cannot say with any certainty what caused this effect, as doing so would require having performed additional experiments to rule out any possible explanations. For example, if photodesorption were the sole cause of the change in conductivity, one could controllably introduce O_2 or H_2O molecules onto the surface of our devices (with the devices mounted inside a vacuum chamber) and measure the change in current through the device. Given the discussion in this and the previous paragraph, it is clear that more work is required to better understand and unequivocally determine the exact physics at play leading to the observed changes in device current.

After measuring the IV curve of DevA following exposure to UV, as discussed above, we were obliged to take a hiatus from this project for several months. The photodetector devices were exposed to ambient conditions for the first few weeks of this hiatus before being transferred into a dry nitrogen environment. At the end of this hiatus, we were ready to use the OPO to measure the optical response of our photodetector device, so we removed the devices from storage and prepared to re-measure IV curves for them. During this process, however, we noticed that DevA had been damaged somehow during the hiatus. With this in mind, we performed all remaining measurements reported in this section using DevB. Figure 4.9c shows an IV curve acquired at the end of the hiatus. From this we see that the IV curve is qualitatively similar to that of DevA shown in Figure 4.9b in that it is also linear. We note, however, that the conductance is significantly lower for DevB than it was for DevA. This is as one would expect, given that the hBN comprising DevB was thicker than that in DevA. To check whether this explanation for the lower conductance seen in Figure 4.9c makes sense, we will perform an order of magnitude check for the expected current for DevB, assuming the only difference between DevA and DevB was the hBN thickness. To do so, we will assume that the primary route of conduction through the hBN flakes was through the thinnest regions. So, for the sake of these calculations, the flake thickness for DevA will be 6.0 nm and 10.0 nm for DevB. Now, if we assume that direct tunneling is the dominant conduction mechanism, the current through the device will have an exponential dependence on hBN thickness. As such, we expect that

$$\frac{I_B}{I_A} \approx \frac{e^{-10.0}}{e^{-6.0}} \quad . \tag{4.3}$$

Then, if we substitute in the current through DevA at -10 V ($I_A = -43.5pA$) and solve for I_B, we get an expected current of -0.8 pA. This agrees reasonably well with the measured current through DevB at -10 V, which was -0.7 pA. This, in turn, suggests that the electrical behavior in DevB should have been similar to that of DevA, after accounting for the increased hBN thickness of DevB compared to DevA.

We measured the optical response of DevB using an OPO using the process described in Section 4.3.5.3. During these measurements, we chose to apply 30 V to the device in an attempt to maximize the amount of signal measured. One set of time series data for DevB acquired in this way is shown in Figure 4.10a. There are several features to discuss in this figure. First, the beginning portion of the data is dominated by an approximately exponential decrease in current. After performing additional testing after the OPO measurements, we determined that this behavior is likely due to charging effects in the circuit rather than an intrinsic effect of the device itself. This likely stems from not insignificant capacitance in the measurement setup, including the cables, the device housing, and possibly the input terminals of the current preamplifier. The idea is that each of these components has an effective “shunt” capacitance that connects their high and low voltage sides. When the DC voltage is applied to the circuit, the current will initially flow through these shunt capacitances rather than through the device under test, as the effective resistance of the device (on the order of gigaohms or higher) will be greater than that of the shunt capacitances. However, as the shunt capacitances become charged, their effective resistances will increase, causing the current to start flowing through the device more readily. Eventually, after all charging is complete, the total measured current will be solely that through the device itself. With this discussion in mind, we subtracted a background from the time series data when analyzing this data. We generated the background to be subtracted by first choosing 16 closely-spaced points in the latter two thirds of the data that correspond to periods of darkness, where only the background signal was present. We then linearly interpolated between these points, with the resulting piecewise linear curve representing the background.

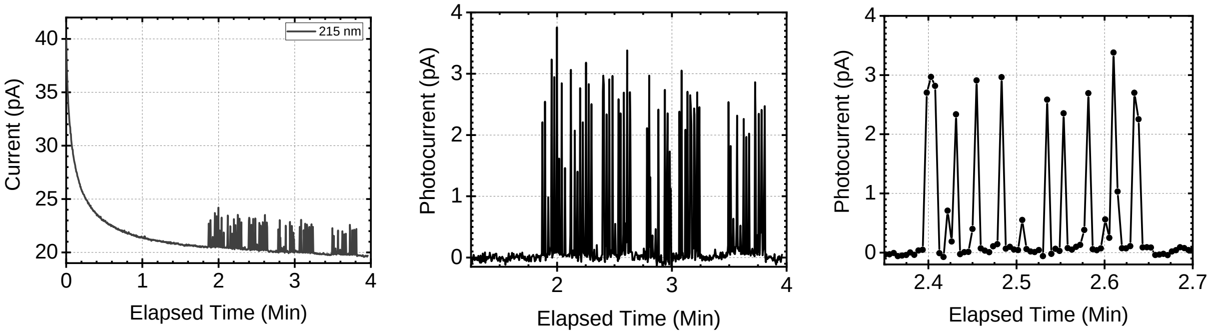

(a) Raw data (b) Background-substracted (c) Zoomed

Figure 4.10: Time series data for DevB acquired under 215 nm illumination.

The second feature of note is the presence of spikes in the current, starting at about two minutes into the acquisition, shown in Figure 4.10a. These current spikes were only present when the device was exposed to light from the OPO and are thus expected to represent the photoresponse of the device. Figure 4.10b shows the spikes from Figure 4.10a after the background had been subtracted from the data. Zooming in to a 30-second window corresponding to a period of illumination revealed that the spikes in current were relatively narrow (total width of about 0.9 seconds), as shown in Figure 4.10c. Additionally, the average spacing between adjacent spikes is about 1.8 seconds, which is much slower than the repetition rate of the OPO (which fires one pulse of light every 100 ms). A question then arises: if these spikes represent the photoresponse of the photodetector device, why are their heights inconsistent and their spacing variable? Our proposed answer to this question relates to the measurement setup we used to acquire this data. Specifically, our LabVIEW VIs used the data acquisition functionalities of the Keithley SMU and multimeter to record and transmit the measurements to a connected computer via a GPIB-to-USB interface. The data acquisition rate of the Keithley equipment, when paired with our LabVIEW VIs for this experiment, was about 3.5 Hz, corresponding to one sample every 286 ms. Given that the repetition rate of the OPO was 10 Hz, this data acquisition rate was far too slow to be able to adequately resolve the response due to individual pulses of the OPO. In order to better resolve the device response, we would have needed to sample data points at a minimum sampling frequency of 20 Hz (according to the Nyquist-Shannon sampling theorem). In reality, however, we would have needed to sample at a much higher frequency, as the pulse width of the output of the OPO was 15 ns. As such, if we expected our device to respond to the pulse excitations instantly, we would need a sampling frequency of about 133 MHz. On the contrary, for a more reasonable response time on the order of 1 ms or greater, a minimum sampling frequency of 2 kHz would have been sufficient. Another measurement consideration is the fact that our data sampling was not necessarily synchronized with the firing of the OPO, leading to a non-zero phase difference between the two. With this discussion in mind, it is possible that the spikes in current we see in Figure 4.10 represent the photoresponse of DevB, but with a significant degree of aliasing present. We will proceed with this section under the tentative assumption that this is true. However, we acknowledge that the veracity of this claim remains unproven, and therefore caution that the following discussion should be taken with a healthy dose of skepticism.

Based on the assumption that the spikes in current discussed above represent the photoresponse of the device, obscured by aliasing, we can use the heights of these spikes to obtain an estimate of the optical performance of the photodetector device. At this point, we needed to decide how to determine the magnitude of the photocurrent response from the background-subtracted data (e.g., as shown in Figure 4.10b). A common method that one could use to determine the magnitude of the response of a photodetector, in the case of a pulsed or optically-chopped excitation, is to use the peak-to-peak (or sometimes the root mean squared) amplitude of the variation in the current signal between periods with and without illumination. Given the aforementioned tenuous interpretation of the data, we felt that using this method to determine the magnitude of the photoresponse was unjustified, as it would not adequately reflect the uncertainty of the estimation. With this in mind, we decided to use a somewhat more statistical approach to determine the magnitude of the response. We first eliminated the data points corresponding to the background along with those within the noise envelope thereof (using the initial period without illumination as the reference for background and noise amplitude), leaving only the data points that were above the noise level. This generally left at least 70 data points, of which we then calculated the mean and standard deviation. Having done this, we used the calculated mean as the estimated photoresponse and the standard deviation as an estimate of the uncertainty in the response estimation. The results of these calculations are shown in Figure 4.11a and listed in Table 4.3.

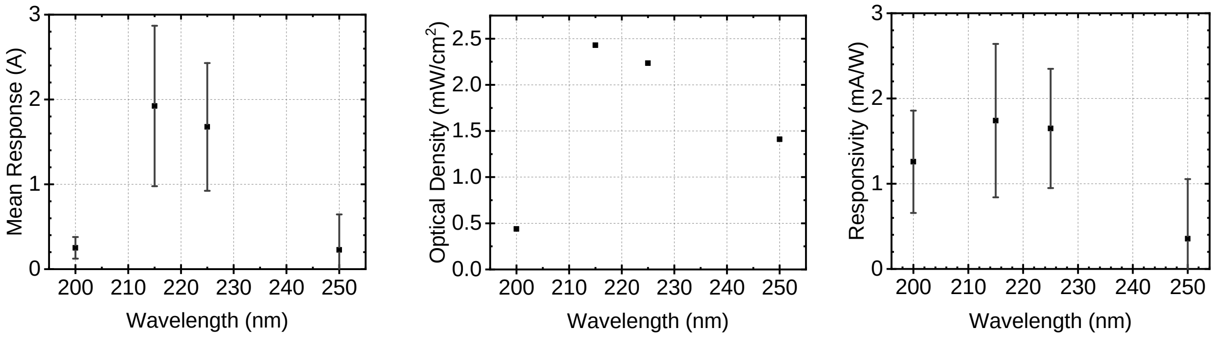

(a) Photocurrent response

(b) Optical power density data

(c) Responsivity

Figure 4.11: Photocurrent excitation and response and data.

Table 4.3: Optical response measurement data

Wavelength (nm)	200	215	225	250
Mean Response (pA)	0.251	1.92	1.68	0.227
Response Uncertainty (pA)	0.128	0.946	0.753	0.418
Optical Power Density $\left(\frac{mW}{cm^2}\right)$	0.439	2.43	2.24	1.41
Responsivity $\left(\frac{mA}{W}\right)$	1.26	1.74	1.65	0.35
Responsivity Uncertainty $\left(\frac{mA}{W}\right)$	0.6	0.9	0.7	0.7
Quantum Efficiency (%)	1.0	0.8	0.9	0.2

Having obtained an estimate of the photoresponse of DevB to illumination by several wavelengths in the UV, we proceeded to calculating a figure of merit of the detector. In order to do so, and as discussed in Section 4.3.5.3, we measured the optical power density of the light produced by the OPO using a laser power meter. The results of these measurements are shown in Figure 4.11b. Using this data, along with the area of DevB reported in 4.2, we calculated the responsivity and quantum efficiency of DevB at the wavelengths for which we had measurements (as discussed in Section 4.2.3). These two figures of merit are also shown in Table 4.3.

To provide context for the figures of merit discussed above, we will now discuss the responsivities of other UV photodetector devices reported in the literature. For example, lateral detectors based on hBN films (either CVD-grown or nanosheets) have achieved responsivities spanning a wide range, including 54 $^{\mu A}/_{W}$ to 675 $^{mA}/_{W}$ for illumination with ~250 nm light [90, 110, 111]. The lateral extent of these devices tends to be much larger than the ones used in this study. Additionally, the highest responsivities tend to be observed in those devices which utilized hBN films that were significantly thicker than those discussed here, likely resulting in the hBN absorbing a significantly higher proportion of incident photons. Additionally, UV detectors utilizing other absorbing materials have been reported. For example, several SnO_2 nanoparticle array-based detectors (using a lateral design) have demonstrated responsivities as high as 275 - 1002 $^{A}/_{W}$ [153]. Finally, the technical specification for the Si photodetector used with the laser power meter (model 818-UV) report a responsivity of about 120 $^{mA}/_{W}$. With these comparisons in mind, we can see that the photodetector devices discussed in this chapter performed orders of magnitude better than some reported devices, and orders of magnitude poorer than others (including the commercial Si-based detector).

4.5 Concluding Thoughts and Opportunities for Future Work

In this chapter, we have described efforts to fabricate a UV photodetector device based on exfoliated hBN crystals with thickness of tens of nanometers or less. The lateral sizes of the hBN flakes limited the dimensions of the resulting photodetector devices, requiring the use of electron beam lithography for device patterning. Nevertheless, we successfully patterned two such devices, each featuring a graphene top electrode, which served as both a semi-transparent material and likely a partial optical absorber to enhance the range of operation of the devices. Unfortunately, we experienced a significant number of challenges during the characterization process, eventually leading to the destruction of both devices discussed in this chapter. These challenges made performing a robust suite of device characterizations difficult, thus leading to significant uncertainty in the results, both in terms of the calculations and possible explanations for the observed behaviors. With this in mind, we would like to focus the remainder of this section on making suggestions to improve the work discussed in this chapter.

One of the main challenges in performing this study was the fabrication process. While the process described in Section 4.3 yielded two devices that behaved more or less as expected, at least initially, the active areas of the devices were far too small to be relevant on an industrially-applicable scale, even though they were reasonably large for ultra-thin exfoliated flakes. From our observations, there is a direct correlation between the lateral and vertical extent of exfoliated flakes, as the additional exfoliations required to produce thinner flakes also tend to fracture the crystal being exfoliated. Thus, one way to achieve larger active areas would be to simply exfoliate the hBN flakes fewer times. Alternatively, it is likely that the exfoliation process will produce flakes with varying thicknesses, even within the same flake. In this case, it could be possible for an experimenter to find a flake with a very thin, flat portion that also includes one or more thicker regions, creating a sort of staircase. It is possible that the individual steps on such a flake could be larger than several microns across, thus allowing for larger device areas. Additionally, such a stepped hBN flake would enable the fabrication of multiple photodetector devices simultaneously, each with a different hBN thickness. This would be advantageous for characterizing the thickness-dependence of any photoresponse observed, as discussed in the conclusion section of the previous chapter.

Despite their generally higher quality, materials produced by traditional mechanical exfoliation are simply not viable for use in industrially scalable processes. However, as the discussion of other journal articles in this and the previous chapter suggests, there are other material sources that can achieve decent performance in a more scalable manner. For example, solution-processed or laser-ablated boron nitride nanosheets can achieve large-area coverage. From the reports of detector devices based on hBN from these sources, we surmise that graphene-based top or bottom electrodes remain underutilized, despite their compact nature and added functionality of extending the wavelength range of operation for photodetector devices. Additionally, most groups seem to have historically focused primarily on fabricating detectors with lateral device designs. As such, it could be fruitful to characterize the performance of additional hBN-based devices that utilize vertical designs and hBN from alternative sources.

Another challenge we faced during the work for this chapter was finding and utilizing one or more light sources spanning the UV range and providing enough intensity. In the end, we settled on the OPO discussed in Section 4.3.5.3, as it was generally able to provide relatively high intensities over much of the UV and into the visible range. The goal was to use this to characterize our devices under illumination at a variety of wavelengths, which would have yielded a comprehensive set of photoresponse data ranging from about 192 nm (6.4 eV, above the band gap of hBN) to around 1000 nm (1.2 eV, well below the band gap of hBN). We expected that doing so would help us to determine the mechanism responsible for producing the photoresponses seen in this chapter and Chapter 3. The main challenge in using the OPO for our experiments was the pulse width of the output. Recall that the pulse width for the signals generated by the OPO (15 ns) is very short, making it difficult to record data fast enough using the Keithley equipment and our original LabVIEW VI. We did, however, develop an improved version of this VI to acquire data at a sampling frequency of about 200 kHz using different data acquisition hardware. Unfortunately, we never got to use this VI. In addition to this, we had also planned to use an oscilloscope to measure the response, as it had a sampling bandwidth of 200 MHz and could be synchronized to a sync signal from the OPO. Another consideration relating to data acquisition speed is the rise time of the current preamplifier. The rise time generally increased with increasing gain. For example, the 10 $^{nA}/_{V}$ and 10 $^{pA}/_{V}$ sensitivity (gain) settings having minimum rise times of 40 μs and 1.1 ms, respectively. As such, the preamplifier itself would have imposed a limit on how fast we could have justifiably acquired data (1 kHz - 25 kHz for the range of sensitivities mentioned previously). With this in mind, it would be useful to obtain a preamplifier with shorter response times. Another option, which would largely circumvent the constraints on sampling rate, would be to use a different light source. For example, a continuous wave laser, passing through an optical chopper, could accomplish the same task as the OPO. The optical chopper would likely be necessary to allow the experimenter to determine photodetector rise times and to more accurately measure the low-level signals like to be produced by hBN-based photodetectors.

Yet another issue we ran into while using the OPO to characterize our devices is that of alignment. The spot size of the output was only about 3 mm wide. From our understanding, this is a reasonable spot size for a relatively coherent light source such as an OPO or a laser. However, since our photodetector devices were so small (with the entire lateral extent of each device fitting inside a 1.0 mm wide bounding box), it was very difficult and time-consuming to ensure that we had aligned the devices to the beam properly. This issue was compounded by the fact that the devices were themselves mounted and recessed slightly inside a metallic housing and that they were fabricated on an optically transparent substrate. In the future, it would likely be useful to build a custom apparatus (mountable on an optical bread board) into which the device housing could be inserted to ensure proper alignment of the device with the beam. There are several suggestions to facilitate this. First, alignment would likely have been easier if we had fabricated only one device per substrate, with the device being exactly centered on the substrate. Second, inclusion of two adjustable irises centered on the optical axis through the apparatus, would serve two purposes. The first purpose is that they could be used, in conjunction with the detector of a laser power meter mounted in the sample position (instead of the custom photodetector device to be characterized), to ensure that the apparatus itself was aligned properly with the output beam of the OPO (or other coherent light source). According to our understanding, this is a relatively common technique used in complex optics setups. The idea here is that the beam from the OPO would need to pass through both irises to impinge on the detector and be measured. This will only happen when both irises are aligned to the beam, as the beam would be occluded if one or both of the irises were misaligned. In this way, translating and rotating the alignment apparatus while monitoring the measured beam intensity should allow the user to achieve very accurate alignment. The second use for the irises is the capability to quantitatively measure (or restrict) the spot size of the beam. For example, the open diameter of one of the irises could be reduced (if it is an adjustable iris) at a controlled rate while monitoring the measured beam intensity. By analyzing the resulting data, one can arrive at an estimate of the beam size. Alternatively, one can place a camera (ideally with a high dynamic range) in front of the beam and measure the beam size and shape using resulting images acquired from the camera.

The final area of improvement that we will discuss here involves addressing the influence of charging behavior on the measured current through a very high resistance device (such as the hBN photodetectors discussed in this chapter). The influence of charging on the current can be seen in Figure 4.10a, manifesting as a long settling time. Reducing shunt capacitance is one strategy to reduce the settling time. This could be done, for example, by using shorter BNC cables to connect the Keithley SMU (voltage source), device housing, and current preamplifier, as the capacitance of a coaxial cable increases with its length. Another way to reduce the capacitance would be to use a smaller metal box for the device housing. In fact, the second device housing that we machined was made with this in mind, being less than half the size of the original box. However, we did not have the chance to use this housing with our hBN photodetectors. Another option could involve using equipment which utilizes triaxial rather than coaxial cables. This would facilitate the use of a “guard” in the cabling. In this case, the guard would be the middle sheath of the triaxial cable, which would be held at a voltage almost exactly the same as the outermost sheath, which would carry the low voltage signal. This would have two beneficial effects. First, it would reduce the leakage current (due to shunt resistance from the insulation in the cable itself) between the high and low signal leads would be minimized, as it would instead flow into the guard lead. The guard sheath should also effectively reduce the capacitance between the high and low signal bearing wires, thus also reducing the transient background current.

APPENDIX A: COPYRIGHT PERMISSION NOTICES

The following copyright licenses were obtained from Springer Nature for the purpose of reproducing portions of the below-mentioned journal articles in this dissertation.

Table A.1: Springer Nature reuse permission information for content in Chapter 2

License Number	5264291360368
License date	Mar 08, 2022
Licensed Content Publisher	Springer Nature
Licensed Content Publication	MRS Advances
Licensed Content Title	STM Tip-Induced Switching in Molybdenum Disulfide-Based Atomristors
Licensed Content Author	Jesse E. Thompson et al
Licensed Content Date	Sep 17, 2019
Type of Use	Thesis/Dissertation
Requestor type	academic/university or research institute
Format	electronic
Portion	full article/chapter
Will you be translating?	no
Circulation/distribution	1 - 29
Author of this Springer Nature content	yes
Title	Electronic and Optoelectronic Properties of Two-Dimensional Heterostructures for Next-Generation Device Technologies
Institution name	University of Central Florida
Expected presentation date	Mar 2022
Order reference number	STMSwitching-Dissertation
Requestor Location	University of Central Florida, 4111 Libra Drive, PS430, ORLANDO, FL 32816, United States, Attn: University of Central Florida
Total	0.00 USD

Table A.2: Springer Nature reuse permission information for content in Chapter 3

License Number	5264300126574
License date	Mar 08, 2022
Licensed Content Publisher	Springer Nature
Licensed Content Publication	MRS Advances
Licensed Content Title	Solar-Blind Ultraviolet Photodetectors Based on Vertical Graphene-Hexagonal Boron Nitride Heterostructures
Licensed Content Author	Jesse E. Thompson et al
Licensed Content Date	Dec 26, 2020
Type of Use	Thesis/Dissertation
Requestor type	academic/university or research institute
Format	electronic
Portion	full article/chapter
Will you be translating?	no
Circulation/distribution	1 - 29
Author of this Springer Nature content	yes
Title	Electronic and Optoelectronic Properties of Two-Dimensional Heterostructures for Next-Generation Device Technologies
Institution name	University of Central Florida
Expected presentation date	Mar 2022
Order reference number	UVPD-Dissertation
Requestor Location	University of Central Florida, 4111 Libra Drive, PS430, ORLANDO, FL 32816, United States, Attn: University of Central Florida
Total	0.00 USD

APPENDIX B: METHOD OF ESTIMATING TIP-SAMPLE FORCE IN STM

Section 2.4 of this dissertation included an estimation of the attractive force between the STM tip and the top surface of the graphene comprising the Graphene-MoS_2-Au model RSE. This appendix outlines the method used to estimate this tip-sample attractive force.

To begin, we recall from Section 2.2.4 that STM tips typically have radii of curvature of around 20-200 nm. While these radii of curvature are small on the macro-scale, they are still large compared to atomic diameters (which are usually on the order of several Angstroms). This means that the very apex of an STM tip is actually quite blunt on the atomic scale. In fact, this is the reason that the 1D quantum tunneling model can be used to model the behavior of STM (since it was adapted from theory describing solid-state tunnel junctions, as discussed in Section 2.2.2)! With this in mind, we will henceforth treat the STM tip as a large, flat, metallic plane. This treatment means that the tunnel junction is essentially the same configuration as a parallel plate capacitor with stacked dielectrics. This configuration is shown schematically in Figure B.1.

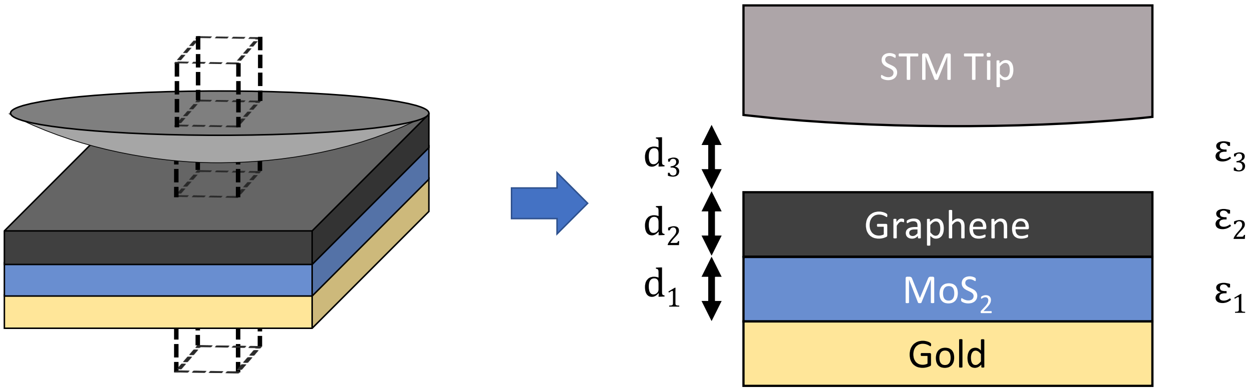

Figure B.1: Schematics showing a portion of the STM tip near the RSE device discussed in Chapter 2. Left: 3D representation. Right: A 2D projection of the vertical 'core' of the tip/sample encompassing the apex of the STM tip (represented as the dashed rectangular prism at left). The tip curvature seen in this subfigure is approximately to scale for a 20 nm wide core of a tip with a 100 nm radius of curvature.

We will first illustrate the method of calculating the force between the plates of a capacitor with a single dielectric, as it is simpler and still relevant to the discussion at hand. Recall that, for a parallel plate capacitor, an applied voltage will induce the accumulation of charge on surfaces of the dielectrics. For a capacitor with only a single dielectric, the capacitance, surface charge, and electric field inside the capacitor are given by

$$\begin{aligned} C &= \frac{A\varepsilon}{d} \\ \sigma &= \frac{Q}{A} = \frac{CV}{A} \\ E &= \frac{V}{d} \quad , \end{aligned} \tag{B.1}$$

where A is the area of the capacitor under consideration, $\varepsilon = k\varepsilon_0$ is the permittivity of the dielectric, ε_0 is the permittivity of free space, k is the dielectric constant of the dielectric (k=1 for vacuum), V is the voltage applied to the plates, d is the separation distance between the plates and Q is the magnitude of the total charge on each plate.

We know that the charges accumulated on each of the plates will be equal in magnitude but opposite in polarity. Thus, one plate will feel an attractive force from the other plate. The magnitude of this force will be given by

$$F = EQ = E\sigma A \quad . \tag{B.2}$$

Plugging the Equations B.1 into this equation and simplifying gives:

$$\frac{F}{A} = \frac{k\varepsilon_0 V^2}{d^2} \quad . \tag{B.3}$$

Now we consider the case of a stacked capacitor containing three dielectrics (corresponding to MoS_2, graphene and vacuum in the case of the RSE device). This arrangement can be treated as a set of three capacitors in series. Thus, the capacitance of each "sub-capacitor" (dielectric layer) can be calculated as in Equation B.1. The total capacitance of the stacked capacitor will be calculated as in Intro Physics II:

$$\frac{1}{C_{tot}} = \frac{1}{C_1} + \frac{1}{C_2} + \frac{1}{C_3} \quad . \tag{B.4}$$

Additionally,

$$\begin{aligned} \varepsilon E_i &= \frac{C_{tot} V}{A} \\ E_i &= \frac{V_i}{d_i} \quad . \end{aligned} \tag{B.5}$$

The first of these equations is essentially just Gauss's law (recall that the electric displacement field, $D = \varepsilon_i E$ is constant inside the stacked capacitor rather than the pure electric field) and $Q = C_{tot} V$. Combining the above two equations and using Equations B.1, we can calculate the voltage drop and capacitance for one of the sub-capacitors:

$$\begin{aligned} V_i &= \frac{C_{tot} d_i}{\varepsilon_i A} V \quad . \\ \sigma_i &= \frac{C_i V_i}{d_i} = \frac{C_i C_{tot} d_i}{\varepsilon_i A^2} \quad . \end{aligned} \tag{B.6}$$

After simplification, the surface charge on one of the sub-capacitors will be

$$\sigma_i = \frac{\varepsilon_j \varepsilon_k}{d_1 \varepsilon_2 \varepsilon_3 + d_2 \varepsilon_3 \varepsilon_1 + d_3 \varepsilon_1 \varepsilon_2} \quad , \tag{B.7}$$

for {i,j,k} ∈ {1,2,3} and $i \neq j \neq k$. The final mathematical operation is to simply combine Equations B.2, B.5, and B.7 to get

$$\frac{F_i}{A} = \frac{V^2 \varepsilon_0 k_i k_j^2 k_k^2}{(d_1 k_2 k_3 + d_2 k_3 k_1 + d_3 k_1 k_2)^2} \quad . \tag{B.8}$$

We know that the dielectric constant of graphene is 6.9 and about 4.1 for MoS_2 [154, 155].

We can now, in principle, calculate the attractive forces on the graphene. However, keeping in mind that this method of estimating the force is just an approximation (and doesn't capture all intricacies), we will concern ourselves only with the ratio of the forces. Specifically, we want to know the factor by which the force on a graphene sheet directly connected to an electrode is larger than the same force on the sheet of graphene in the model RSE described in Chapter 2. Calculation of the force in the first case (graphene directly shorted to electrode) is relatively straightforward - substitute the dielectric constant (k=1, since the gap is vacuum) and the tip-sample separation distance into Equation B.3. Calculating the force on the graphene in the stacked capacitor arrangement is similar (using Equation B.8). In this case, variables with subscript 1 and j correspond to MoS_2, subscripts 2 and k correspond to graphene and subscripts 3 and i correspond to the vacuum gap. We will assume a MoS_2 thickness of 0.6 nm (corresponding with a single layer) and graphene thickness of 1.2 nm (corresponding to four layers). Calculating in this way and then dividing the force on the single capacitor by the force on the stacked capacitor with the above values gives the desired ratio. For a tip-sample separation distance in the range of 0.8 - 1.0 nm, the ratio is in the range of 7-10. Since the expressions for forces in both the single and stacked cases have the same dependence on area and voltage, they cancel out of the ratio, showing that the ratio is insensitive to the specific area or voltage applied.

APPENDIX C: ESTIMATING PHOTOCURRENT GENERATED IN A GRAPHENE FILM

Section 3.4 includes a discussion of photocarrier generation in the graphene electrodes of the hBN-based UV photodetector devices discussed in that chapter. The discussion involved estimating the magnitude of the possible photocurrent generated in the photodetector device under illumination by UV light. This appendix contains the details of this estimation. The following derivation essentially follows the method reported by Kang, *et al.* in [150], though the derivation method employed herein is slightly different. Our derivation is included here primarily for completeness and to demonstrate the estimation method.

The estimation process begins by determining the distance that a photogenerated carrier can travel before it undergoes recombination. This is the drift length, and is related to the drift speed and carrier lifetime in the graphene:

$$\ell_d = v_d \tau \quad . \tag{C.1}$$

The drift speed, in turn, is related to the electron or hole mobility (μ) in the graphene and the electric field strength inside the graphene. Assuming that the electric field strength is given by $E = {}^{V}\!/_{d}$, where V is the voltage applied to the contacts and d is the distance between the contacts,

$$v_d = \mu E = \frac{\mu V}{d} \quad . \tag{C.2}$$

the average lifetime of photogenerated charge carriers in graphene is between less than one picosecond to several hundreds of picoseconds, depending on the quality of the graphene film [156–158]. Herein we will use 100 ps as the value for the carrier lifetime, as it is on the higher end of the range and will therefore give a reasonable upper bound on the expected photocurrent. The carrier mobility in graphene also varies considerably, depending on the quality of the graphene film and substrate interactions. For the purposes of this estimation process, we will assume a value of 30,000 ${}^{cm^2}\!/_{Vs}$ for the mobility, which is quite high for a CVD graphene film ([159]). Additionally, we will assume that the applied voltage is 150 mV and that the distance between contacts is 8 mm, so that our estimations will be representative of the device described in Chapter 3. Substituting these values into the equations above gives a maximum drift length of 5.6 nm before recombining and an expected drift speed of 56.3 $^{m}/_{s}$.

Now we turn our attention to determining the current due to photocarriers generated in the graphene film. Only those photocarriers that are generated within one drift length from a contact will be able to travel to the contact, and therefore contribute to a measurable current, before recombining. We will assume that photocarriers are generated uniformly across the entire graphene film in question. Consider a small strip of the graphene film extending the full "width" of the strip (W, running perpendicular to the direction of current) and infinitesimal " length" ($d\ell$, running parallel to the direction of current). The number of photocarriers generated in this infinitesimal strip is given by

$$N = \frac{\varepsilon_G P A}{E_{photon}} = \frac{\varepsilon_G P W d\ell}{E_{photon}} \quad , \tag{C.3}$$

where ε_G is the number of photocarriers generated per incident photon, P is the optical power density of the incident light, and E_{photon} is the photon energy of the incident light. As previously stated, only those carriers generated within one drift length of a contact will be able to reach the contact before recombining. Nevertheless, we assume that each differential slice will produce the same number of carriers per unit time. The fraction of carriers generated a distance ℓ away from the contact that will be able to reach the contact before recombining will be given by

$$r = \frac{\ell}{\ell_0} = \frac{\ell}{v_d \tau} \quad . \tag{C.4}$$

So, for carriers generated a distance $^{\ell_0}/_{2}$ away from a contact, two portions (as given by Equation C.3) will be able to reach the contact, whereas only one portion of those generated at a distance of one full drift length. The amount of photocurrent contributed by a single differential area, then, will be

$$dI = rNq = q\left(\frac{\ell}{\ell_0}\right)\left(\frac{\varepsilon_G PW d\ell}{E_{photon}}\right) \quad , \tag{C.5}$$

where q is the elementary charge unit. Integrating over the contributions of all differential areas within one drift length gives the total photocurrent expected:

$$I = 2\int dI = 2q\frac{\varepsilon_G PW}{\ell_0 E_{photon}}\int_0^{\ell_0} \ell d\ell = \frac{q\ell_0\varepsilon_G PW}{E_{photon}} \quad , \tag{C.6}$$

where the factor of 2 is included to account for the fact that the processes discussed in this appendix will occur at both contacts. As discussed in Section 3.3.2.5, the width of the graphene strips used in the photodetector under discussion was 4 mm. The primary wavelength component of UV Source 1 was 254 nm (4.89 eV) with an optical power density of 23 $^{\mu W}/_{cm^2}$, while UV Source 2 emitted primarily at 365 nm (3.40 eV) with an optical power density of 6700 $^{\mu W}/_{cm^2}$. Finally, for the sake of obtaining an upper bound on the potential photocurrent generated, we will assume that photocarriers are generated with perfect efficiency (i.e., one photocarrier generated per incident photon). In reality, the efficiency would be closer to 0.04 to 0.09 (corresponding to the absorptance of graphene at the respective wavenelgths) [113]. Substituting these values (separately) into Equation C.6 gives an expected photocurrent of 1 pA for UV Source 1 and 443 pA for UV Source 2.

APPENDIX D: WIRE BONDING

We used a wire bonder to make electrical connections between microelectronic devices and the chip carriers they were mounted in the work described in this dissertation. This appendix serves as a record of the knowledge and experience acquired during the process of repairing the wire bonder and using it to bond. Specifically, we used a wire bonder made by West Bond (model 7400D), equipped with a 45° wedge. For reference, the firmware version used by the bonder during this work was version 3.80. This wire bonder, along with annotations specifying some of the most important parts of the machine, is shown in Figure D.1.

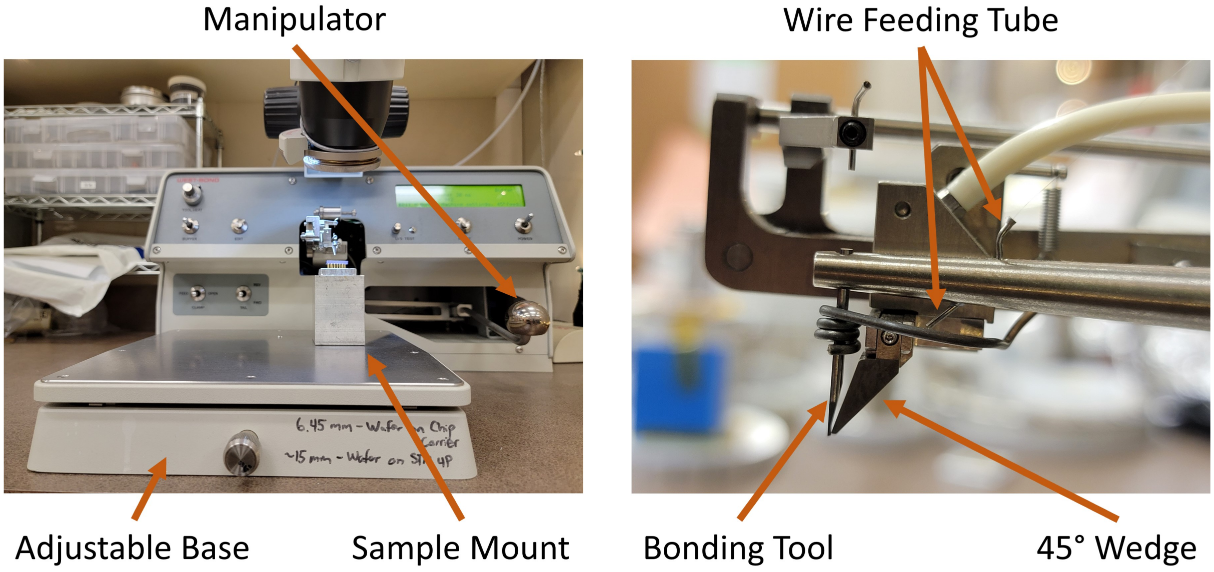

(a) Overview

(b) Close-up of bonding arm

Figure D.1: Annotated images of the West Bond 7400D wire bonder.

D.1 Opening Remarks

Successful wire bonds should produce relatively low-resistance electrical connections between two contact pads. Additionally, the bonds should be fairly mechanically robust. Based on our discussions with West Bond technicians, the mechanical robustness of a wire bond is typically determined by the maximum amount of mass that can be suspended by the bond (with the bonded sample turned upside down) before the bonds break. A “good” wire bond should be able to hold about 50 g (corresponding to about 0.1 lbs or 0.5 N of force) without breaking. We didn’t quantitatively determine the strength of the wire bonds that we made. However, we note here that the bonds made using the process below could withstand being gently pulled on with tweezers without breaking free from the sample. Our contact pads consisted of 50 nm of Au with about 5 nm of Cr for our devices, and textured Au on ceramic for the contact pads on the chip carriers.

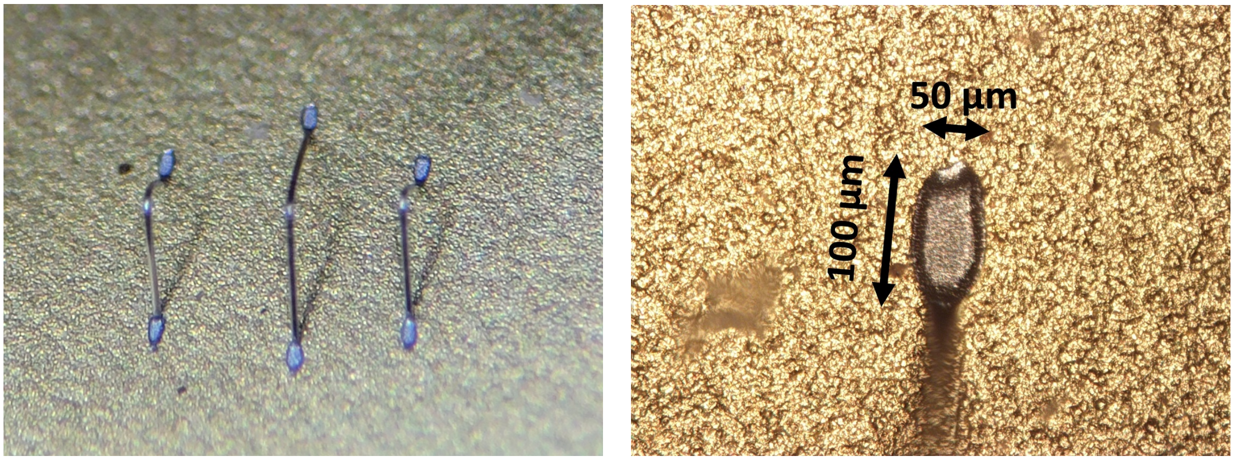

(a) Example of successful bonds

(b) Dimensions of wire bond

Figure D.2: Example wire bonds on Au contact pad

Another point worth making at the beginning of this appendix relates to optimization of the bonding process. The success rate of wire bonding depends critically on a number of factors (discussed below), including various parameters which can be changed in the settings of the wire bonder. Experience shows that different bonding tasks can require different sets of parameters. For example, the parameters which produce decent bonds for a particular type of wire bonding to Al contact pads might be different from those used to bond to Au contact pads. Similarly, using wire with different compositions will likely require different parameters. For example, the work in this dissertation used primarily Al wire, but the Ishigami research group had previously used Au wires. Additionally, different wires can have different properties, such as wire diameter and tensile strength. When comparing or ordering bonding wire, one should pay specific attention to the "elongation" rating of the wires, as this gives information about how much the wire can stretch before breaking. Finally, bonding wires can become brittle over time. Thus, new wire will not necessarily behave the same way as wire that is one or more years old. Our experience (and that of West Bond technicians) suggests that the bonding parameters must be optimized whenever a significant change is made to the bonding process (such as changing any of the factors mentioned in this paragraph).

D.2 Basic Procedure

The following is a description of the basic procedure used in this work to perform wire bonding. The machine parameters we used to accomplish the bonding for this work are shown in Table D.1. We used Al wire (1 mil diameter, corresponding to about 10 gauge) doped with 1% Si. We purchased this wire (product number: Wire.001B) from Bonding Source (a company located in Manchester, New Hampshire). At the time of writing, the wire bonder is fitted to accept half inch spools.

1. Mount the sample to be wire bonded to a sample holder.
2. Place the mounted sample onto the adjustable base of the wire bonder.
3. Adjust the height of the base so that the bonding surface of the sample is 127 mm (5.0 inches) above the surface of the table on which the wire bonder is placed.
4. Set the parameters of the wire bonder, paying special attention to the number of bonds to be made, the ultrasonic power, and the duration for which the ultrasonic power is applied.
    - This is done by pressing the EDIT button on the front of the wire bonder until the

desired setting is displayed, then using the FWD/REV positions on the TAIL toggle switch to make adjustments.

5. Position the mounted sample in the field of view of the wire bonder's microscope, then focus on the surface of the sample. The bonding locations should be roughly centered in the field of view. Also, the sample should be oriented so that any locations to be bonded are aligned vertically in the field of view.
    - It may be necessary to decrease the magnification of the microscope (using the small knob nearest the eyepieces on the microscope itself), as higher magnifications have lower depths of field.
    - Aligning bonding locations horizontally in the field of view will likely result in the wire bond failing, and possibly pulling the wire out of the bonding tool.
6. Move the bonding tool into the field of view of the microscope using the manipulator arm.
7. Maneuver the bonding tool toward the sample so that the tip gently (and slowly) touches the surface of the sample in the location of the first bond. The bonder should beep when contact is made with the surface.
    - This can be done by lowering the bonding tool straight downward until it touches the sample. However, we found that lowering it in a diagonal fashion (about 30-45° from the surface normal) tends to work better.
8. Lift the bonding tool away from the surface slowly, either straight upward or in a diagonal fashion.
    - During this process, a hissing will be heard from the bonder. This indicates that the jaws of the 45° wedge are open, allowing the wire to unspool and be pulled out the end of the bonding tool.

  - The bonding tool should be lifted high enough to unspool a sufficient amount of wire. The amount of wire unspooled determines the maximum distance between the wire bonds, the tension in the wire, and the maximum height of the wire after bonding.

9. Lower the bonding tool toward the second bonding location.
    - When the bonding tool is lowered sufficiently, the hissing will stop, the jaws close, and the wire will be once again clamped.
    - Raising the bonding tool again should cause the jaws to open again, allowing for additional wire to be unspooled if desired.
10. Press the bonding tool into the sample at the bond location gently. This should create the second bond.
11. Retract the bonding tool.
12. Proceed to making any additional wire bonds.

D.3 Troubleshooting

While the wire bonding process is simple and straightforward in principle, it can nevertheless be challenging to produce good, strong bonds on samples. We have generally observed two modes of failure during wire bonding. The first involves wires failing to bond to surfaces altogether (this seems to be the most common issue). The second issue is having bonds that form, but are sufficiently weak that they can detach easily. There are a variety of reasons that this can be the case, and some of them are outlined in this section.

Table D.1: Bonding parameters used for the work described in this dissertation.

Parameter	Bond 1	Bond 2
Bonds Per Wire	2	
Ultrasonic Power	300	300
Ultrasonic Time (ms)	30	30
Loop Height (mils)	N/A	30 (762 μm)
Drop Before Clamp (mils)	N/A	10 (254 μm)
Wire Pull (Motor Steps)	20	
Wire Tail (Motor Steps)	20	
Dual Force	Off	
Beep Upon Contact	On	
Must Lift	Off	
Bond Counter	On	
U/S Power During Feed	0	
Self-Thread	Off	

D.3.1 General Considerations

For best results, any surfaces of a sample involved in wire bonding should generally be clean and dry. If a sample is left out in atmospheric conditions, for example, dust and other contaminants can settle on it and this could potentially result in wire bonding failure. Additionally, bonding surfaces must be hard enough to withstand the bonding process. If the surface is not sufficiently hard, the ultrasonic power will cause the bonding tool to punch through the contact pad. We have found that about 50 nm of Au (with 2-5 nm Cr adhesion layer) forms sufficiently robust contact pads on SiO_2/Si substrates. Also, 280 nm of SiO_2 is generally robust enough that typical wire bonding shouldn't punch through the oxide layer, which would potentially cause electrical shorts through the substrate itself. Another factor to keep in mind is that the bonding surfaces must be flat and parallel to the adjustable base of the wire bonder. If this is not the case, the bottom of the bonding tool will not be parallel to the plane of the bonding surface, which will inhibit the application of force required to deform the wire and adhere it to the sample during the bonding

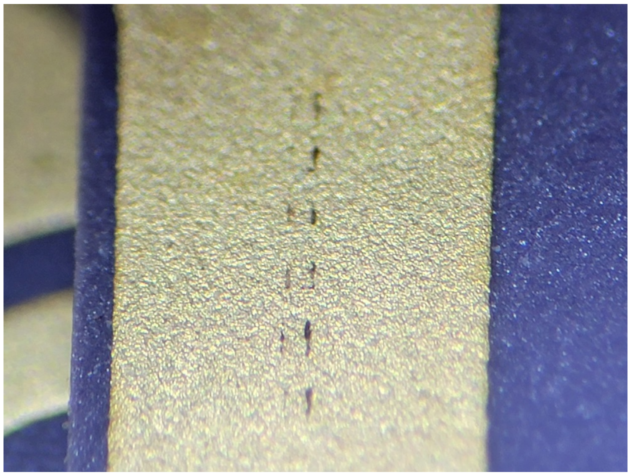

Figure D.3: Impressions from bonding tool.

process. Finally, it is very important that the bonding surfaces should be vertically positioned to be very close to the middle of the vertical travel range of the bonding arm. This corresponds to a height of about 5.0 inches (127 mm) above the surface of the table (or counter) that the wire bonder rests on. This ensures that the bottom of the bonding tool will be parallel to the surface during the bonding process.

D.3.2 Issue: Wires Do Not Bond to Surface, But Indentations Are Left On Sample

One reason that a wire bond can fail is that the wire might not be unspooling properly. From experience, when this happens the bonding tool will usually leave impressions on the bonding surface in the form of two short, parallel lines oriented along the direction from the front to the back of the bonder. A picture showing several sets of such impressions is given in Figure D.3. If such impressions are observed, it is very likely that the wire has been pulled out of the bonding tool. This means that, during an attempted bonding process, the bonding tool will press into the sample rather than the wire, leaving behind the impressions.

There are several potential causes for this behavior. The first is that the spool holding the wire might not be able to spin freely enough. The spool itself is held in place on a spindle by a spring which is, in turn, held in place by a retaining screw. This spring should be slightly compressed to keep the spool in place. However, if the retaining screw is tightened too much, the tension in the spring will cause too much friction between the spool and the end of the spindle, making it difficult for the spool to rotate. When this happens, the wire will not be able to unspool properly during the bonding process (when the bonding tool is moved with the jaws open), and the wire will instead be pulled out of the bonding tool. The solution to this is to simply loosen the retaining screw to decrease the tension in the spring.

Another factor that can cause the wire to pulled out of the bonding tool relates to one of the settings that is available in the wire bonder's menu. In particular, the setting is called "U/S Power During Feed". When this setting is enabled (set to a non-zero value), the ultrasonic transducer operates when the bonding tool is being lifted (with the jaws unclamped). This disrupts the wire as it passes through the wire feeding tube and can cause the wire to come out of the bonding tool. Discussions with West Bond technicians indicate that this setting is only intended to be used when performing 90° bonding. However, this wire bonder is normally equipped with a 45° wedge bonder, so the application of additional ultrasonic excitation is unnecessary, as the wire typically should not have trouble routing through the 45° system. With this in mind, the solution to this problem is to set the ultrasonic power during seed setting to 0.

After the cause of the wire pulling issue has been solved, the wire will need to be rethreaded into the bonding tool. Depending on the severity of the issue, the wire should have remained in the jaws of the 45° wedge, so it should be relatively straightforward to rethread it. This situation is shown in Figure D.4a (note that there is no wire extending out the front of the bonding tool). However, if the issue was more severe, or if the wire had not been threaded properly through the wedge, it is likely that the wire will need to be rethreaded through the wedge before threading into the bonding tool.

The first thing to try if the wire comes unthreaded from the bonding tool, but remains

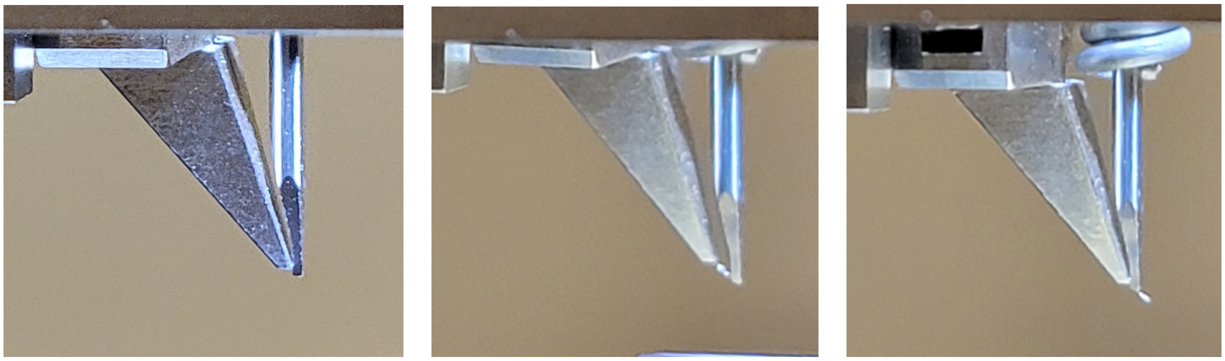

(a) No wire in bonding tool.
(b) Jaw open, wire extended
(c) Jaw closed, with excess wire

Figure D.4: Side view of wedge.

properly fed through the wedge, is to simply open and close the jaws of the wedge. When the jaw is opened, the wire bonder will try to extend the wire a small amount. If the wire is still in the wedge, the extended wire should end up being very close to the hole in the bonding tool (this is shown in Figure D.4b). Upon closing the jaws again, the wire should be pushed through the hole in the bonding tool. This should result in an extra long 'tail' extending out the bottom of the bonding tool, as shown in Figure D.4c. If this happens, the wire should be rethreaded and essentially ready for use. The final step, in this case, is to perform a sacrificial bond to remove the excess. The wire bonder's screen instructs the user to do this whenever the jaws are closed.

If the above procedure fails to reinsert the wire into the bonding tool, the rethreading process will typically need to be performed manually. There is a small hole near the end of the bonding tool on its back side. This hole leads to a channel which extends diagonally downward and out an even smaller hole at the very end of the bonding tool. These can be seen in Figure D.5. In order to rethread the bonding tool, the user should use tweezers to guide the wire into the hole on the back side of the bonding tool and gently push the wire through. Unfortunately, the user will not be able to see the hole, as it is on the back side and is also very small. Ultimately, it takes practice to be able to do this in an expeditious manner, but there are a few tricks that can help improve

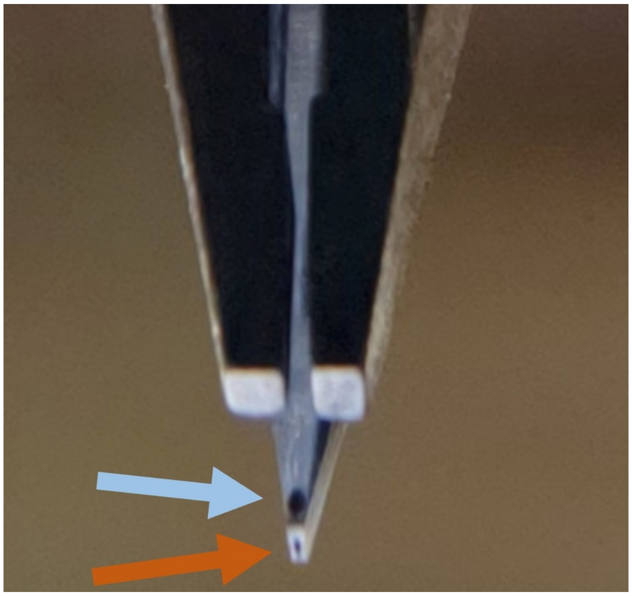

Figure D.5: Backside of the bonding tool. The blue arrow indicates the beginning of the channel into which the wire needs to be threaded. The orange arrow indicates the hole in the bottom where the wire will come out.

chances of success. First, the wire should be held in such a way that it is angled about 45° from the vertical. This will ensure that the wire can slide into the channel when positioned properly, rather than hitting the channel wall and simply bending. Next, the space between the two halves of the wedge jaw (when they are open, which they need to be to rethread) can be used as a sort of guide to approximately align the wire with the center of the bonding tool laterally. After approaching the bonding tool with the wire, the movement of the wire will give a hint as to how the user needs to adjust it before trying again. If the wire is deflected in one direction (around the bonding tool), move the wire in the opposite direction before approaching again. If the wire bends rather than deflects, the wire was either too high or not angled properly.

D.3.3 Issue: The Wire Came Out of the 45° Wedge

It is possible for the wire to come out of the wedge/jaws when a user is manipulating the wire (e.g., while rethreading it into the bonding tool) or if the tension in the wire (e.g., from the spool) is too high during bonding. Figure D.6a shows the situation where the wire has come fully out of the wedge. In this case, the wire will need to be fed back through the wedge. This is done by angling the wire at about a 45° angle relative to the vertical and passing it through an opening at the top rear of the wedge and down through the wedge. Unfortunately, the orientation of the wire feed means that this process must be done without being able to easily see what is happening without assistance (since the wire needs to be fed through the back side of the wedge). It is possible to use a small mirror (for example, the kind used by dentists) to help the user see the back side.

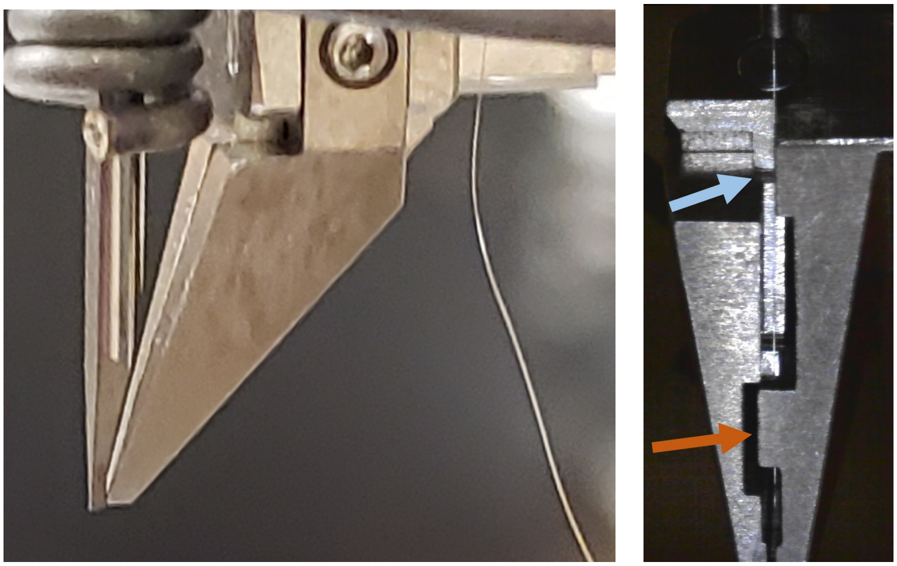

(a) Wire out of wedge (b) Back of wedge

Figure D.6: Images of 45° wedge. The orange arrow indicates the ledge that the wire must be fed over. The blue arrow indicates pin/shelf that the wire can be optionally fed over.

There are two things to keep in mind when doing this. First, the wedge has a ledge (indicated in Figure D.6b with an orange arrow) that the wire must be fed over (i.e., between the ledge and the upper portion of the wedge). This ledge acts as a retainer to keep the wire properly situated in the channel through the wedge. Second, there is a pin/shelf near the top rear of the wedge (shown in Figure D.6b with a blue arrow). This can cause trouble when inserting the wire into the wedge, as it can easily obstruct the wire, causing it to bend rather than pass through properly. There are two options for how to deal with this shelf. First, the user can try to pass the wire underneath it, and then feeding over the ledge further down. Second, the user can pass the wire over the pin, so that it travels between the pin and the top portion of the wedge, and then down over the lower ledge. If the second option is used, the pin itself will act as a retainer to help hold the wire in the wedge, even if it comes loose from the bonding tool.

D.3.4 Issue: The Wire Came Out Of The Feeding Tube

Sometimes, the wire can come out of the feeding tube, especially when a user is trying to feed it through the wedge. If this happens, the wire will need to be fed back through the feeding tube before threading it through the wedge and bonding tool. The idea for this is straightforward: simply push the wire into the opening closer to the wire spool and out the end closer to the wedge. In practice, however, this can be challenging to do, as the feeding tube has several bends which can cause the wire to get stuck. The general strategy is as follows. First, use tweezers (preferably duck-billed tweezers) to gently grab the wire about 5-10 mm above the end. At this point, the wire should be free of any significant bends. Next, gently push the wire into the opening of the feeding tube closest to the wire spool (the opening is flared outward slightly to help with this). It is helpful to engage the ultrasonic transducer while doing this, as the vibrations will help to keep the wire from sticking to the walls of the tube. This is done by pressing the button marked “U/S Test” on the front of the wire bonder. The button should be held down while the wire is being fed, but should be released when the user lets go of the wire (to prevent the wire from slipping back out of the tube). After inserting the first section of wire, the user should use the tweezers to gently grab the next 5-10 mm section of the wire, and gently (and slowly) push it into the tube, using the ultrasonic test while doing so. Repeat this process until the wire comes out the far end of the tube. It is very important that the wire be fed gently, as being too rough will almost certainly cause the wire to form a sharp bend. When this happens, it is very likely that the wire will either not feed properly, or it will snap. In either case, the wire will need to be withdrawn from the feeding tube and the process restarted from the beginning. If the wire is bent, the bent portion should be removed (see the next section for a description of how to do this).

D.3.5 Issue: The Wire Is Too Long To Manipulate Or Is Bent

It is likely that, during the course of working with the wire while fixing any of the above issues, the wire will not necessarily be the optimal length to perform desired manipulations. For example, wires that are either too long or too short are more difficult to thread through the hole in the bonding tool than those that are the optimal length (around 5-10 mm). If the wire is too short, gently pull on the wire (with the jaws open) to unspool more. If the wire is too long, the wire can be cut. Wire cutters are not necessary for this, as the wire is quite small. Instead, use two pairs of tweezers. Use one pair of tweezers to hold the wire at the approximate location where the wire needs to be cut. We have found that using duck-bill tweezers (or any that have wide, flat ends) works best for this. Then, use the second pair of tweezers (usually needle-nose) to gently pull the end of the wire. In this way, the wire should break off near where it is being held by the duck-billed tweezers. The user can then use the needle-nose tweezers to grab the wire slightly further away from the end and proceed to the desired manipulations. Care must be taken, however, not to bend the wire during the process of grabbing it while the end is still being held by the duck-bill tweezers. Bent wires are much more difficult to thread, so if a bend occurs, the wire will likely need to be cut again. An alternate technique to cut a wire is to hold the wire using duck-billed tweezers, and then using needle-nose tweezers to pinch the wire hard enough at the desired location to sever the lower portion.

APPENDIX E: TECHNICAL DRAWINGS

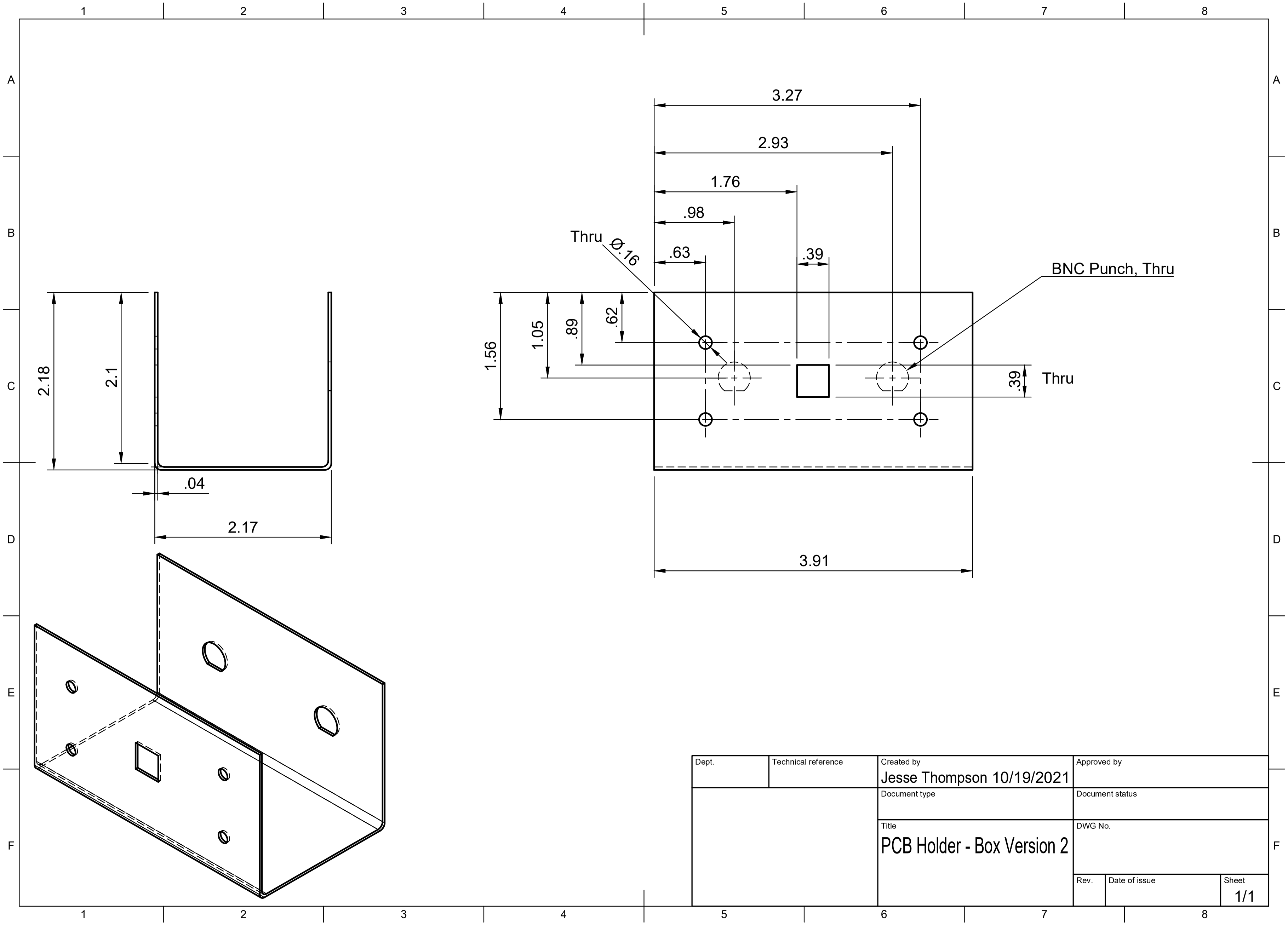

Dept.

Technical reference

Created by
Jesse Thompson 10/19/2021

Approved by

Document type

Document status

Title
PCB Holder - Box Version 2

DWG No.

Rev.

Date of issue

Sheet
1/1

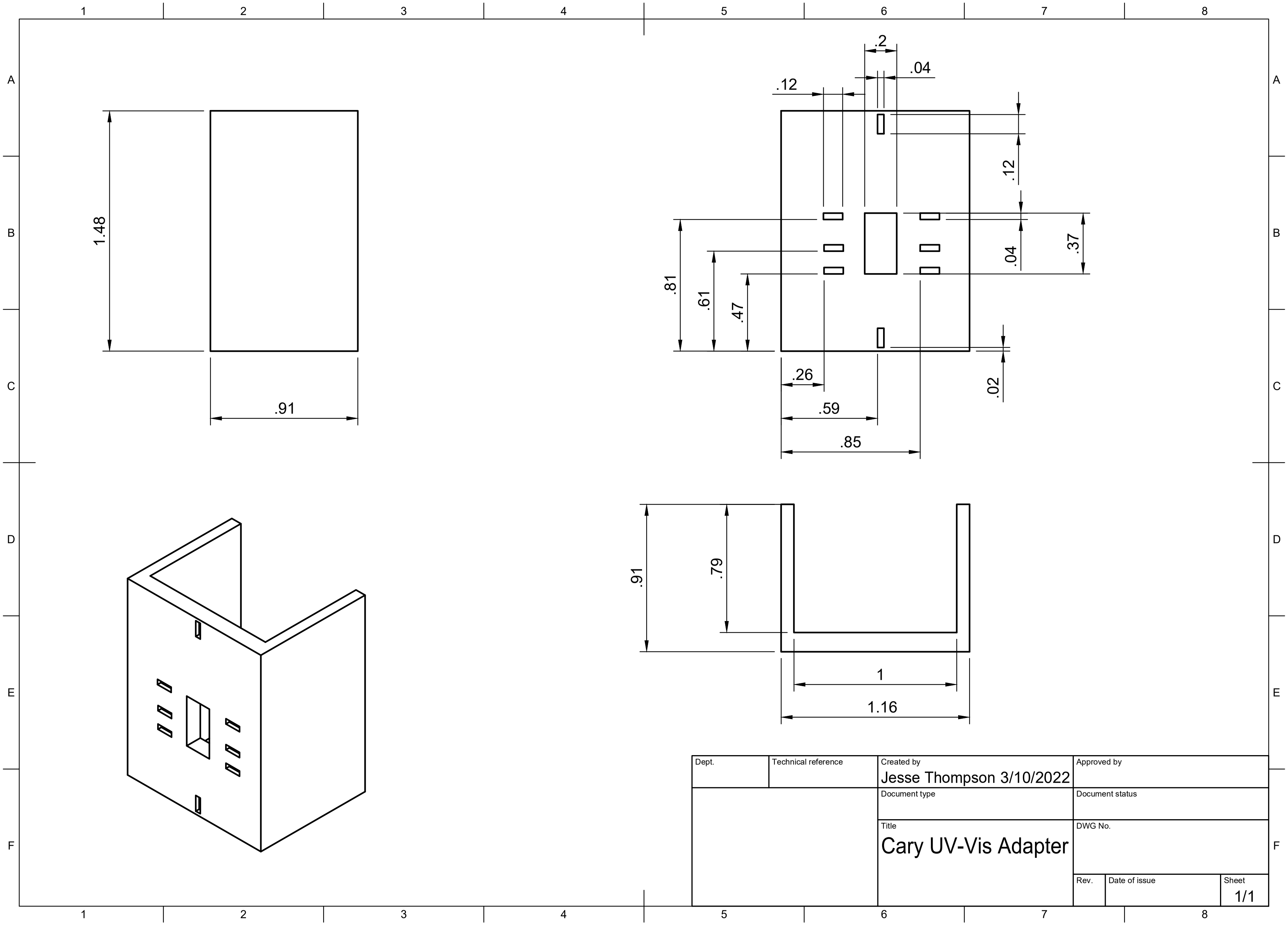

Dept.
Technical reference
Created by
Jesse Thompson 3/10/2022
Approved by
Document type
Document status
Title
Cary UV-Vis Adapter
DWG No.
Rev.
Date of issue
Sheet
1/1

LIST OF REFERENCES

[1] Xuewen Wang et al. “Substrate modified thermal stability of mono- and few-layer MoS2”. In: *Nanoscale* 10.7 (2018), pp. 3540–3546. ISSN: 2040-3364. DOI: `10.1039/C7NR08941D`. URL: `http://dx.doi.org/10.1039/C7NR08941D`.

[2] Hai Yan Nan et al. “The thermal stability of graphene in air investigated by Raman spectroscopy”. In: *Journal of Raman Spectroscopy* 44.7 (2013), pp. 1018–1021. ISSN: 0377-0486. DOI: `https://doi.org/10.1002/jrs.4312`. URL: `https://analyticalsciencejournals.onlinelibrary.wiley.com/doi/abs/10.1002/jrs.4312`.

[3] Fu Liu et al. “Thermal stability of graphene in inert atmosphere at high temperature”. In: *Journal of Solid State Chemistry* 276 (2019), pp. 100–103. ISSN: 0022-4596. DOI: `https://doi.org/10.1016/j.jssc.2019.04.008`. URL: `https://www.sciencedirect.com/science/article/pii/S0022459619301781`.

[4] F. Mahvash et al. “Corrosion resistance of monolayer hexagonal boron nitride on copper”. In: *Scientific Reports* 7.1 (2017), p. 42139. ISSN: 2045-2322. DOI: `10.1038/srep42139`. URL: `https://doi.org/10.1038/srep42139`.

[5] Eric Singh et al. “Flexible Molybdenum Disulfide (MoS2) Atomic Layers for Wearable Electronics and Optoelectronics”. In: *ACS Applied Materials & Interfaces* 11.12 (2019). doi: 10.1021/acsami.8b19859, pp. 11061–11105. ISSN: 1944-8244. DOI: `10.1021/acsami.8b19859`. URL: `https://doi.org/10.1021/acsami.8b19859`.

[6] Seung-Mo Lee, Jae-Hyun Kim, and Jong-Hyun Ahn. “Graphene as a flexible electronic material: mechanical limitations by defect formation and efforts to overcome”. In: *Materials Today* 18.6 (2015), pp. 336–344. ISSN: 1369-7021. DOI: `https://doi.org/10.1016/j.mattod.2015.01.017`. URL: `https://www.sciencedirect.com/science/article/pii/S1369702115000188`.

[7] Giorgia Fugallo et al. "Thermal Conductivity of Graphene and Graphite: Collective Excitations and Mean Free Paths". In: *Nano Letters* 14.11 (2014). doi: 10.1021/nl502059f, pp. 6109–6114. ISSN: 1530-6984. DOI: `10.1021/nl502059f`. URL: `https://doi.org/10.1021/nl502059f`.

[8] Mingyu Sang et al. "Electronic and Thermal Properties of Graphene and Recent Advances in Graphene Based Electronics Applications". In: *Nanomaterials* 9.3 (2019), p. 374. ISSN: 2079-4991. URL: `https://www.mdpi.com/2079-4991/9/3/374`.

[9] Kin Fai Mak et al. "Atomically Thin MoS_2: A New Direct-Gap Semiconductor". In: *Physical Review Letters* 105.13 (2010). PRL, p. 136805. DOI: `10.1103/PhysRevLett.105.136805`. URL: `https://link.aps.org/doi/10.1103/PhysRevLett.105.136805`.

[10] Weijie Zhao et al. "Origin of Indirect Optical Transitions in Few-Layer MoS2, WS2, and WSe2". In: *Nano Letters* 13.11 (2013). doi: 10.1021/nl403270k, pp. 5627–5634. ISSN: 1530-6984. DOI: `10.1021/nl403270k`. URL: `https://doi.org/10.1021/nl403270k`.

[11] Sujay B. Desai et al. "Strain-Induced Indirect to Direct Bandgap Transition in Multilayer WSe2". In: *Nano Letters* 14.8 (2014). doi: 10.1021/nl501638a, pp. 4592–4597. ISSN: 1530-6984. DOI: `10.1021/nl501638a`. URL: `https://doi.org/10.1021/nl501638a`.

[12] Jesse E. Thompson et al. "STM Tip-Induced Switching in Molybdenum Disulfide-Based Atomristors". In: *MRS Advances* 4.48 (2019), pp. 2609–2617. ISSN: 2059-8521. DOI: `10.1557/adv.2019.322`. URL: `https://doi.org/10.1557/adv.2019.322`.

[13] Chris D. English et al. "Improved Contacts to MoS2 Transistors by Ultra-High Vacuum Metal Deposition". In: *Nano Letters* 16.6 (2016). doi: 10.1021/acs.nanolett.6b01309, pp. 3824–3830. ISSN: 1530-6984. DOI: `10.1021/acs.nanolett.6b01309`. URL: `https://doi.org/10.1021/acs.nanolett.6b01309`.

[14] R. J. Ge et al. “Atomristor: Nonvolatile Resistance Switching in Atomic Sheets of Transition Metal Dichalcogenides”. In: *Nano Letters* 18.1 (2018), pp. 434–441. ISSN: 1530-6984. DOI: `10.1021/acs.nanolett.7b04342`. URL: `https://pubs.acs.org/doi/pdfplus/10.1021/acs.nanolett.7b04342`.

[15] Myungsoo Kim et al. “Zero-static power radio-frequency switches based on MoS2 atomristors”. In: *Nature Communications* 9.1 (2018), p. 2524. ISSN: 2041-1723. DOI: `10.1038/s41467-018-04934-x`. URL: `https://doi.org/10.1038/s41467-018-04934-x`.

[16] Hirokjyoti Kalita et al. “Artificial Neuron using Vertical MoS2/Graphene Threshold Switching Memristors”. In: *Scientific Reports* 9.1 (2019), p. 53. ISSN: 2045-2322. DOI: `10.1038/s41598-018-35828-z`. URL: `https://doi.org/10.1038/s41598-018-35828-z`.

[17] Muhammad Muqeet Rehman et al. “Resistive Switching in All-Printed, Flexible and Hybrid MoS2-PVA Nanocomposite based Memristive Device Fabricated by Reverse Offset”. In: *Scientific Reports* 6.1 (2016), p. 36195. ISSN: 2045-2322. DOI: `10.1038/srep36195`. URL: `https://doi.org/10.1038/srep36195`.

[18] G. Venugopal and S. J. Kim. “Observation of Nonvolatile Resistive Memory Switching Characteristics in Ag/Graphene-Oxide/Ag Devices”. In: *Journal of Nanoscience and Nanotechnology* 12.11 (2012), pp. 8522–8525. ISSN: 1533-4880. DOI: `10.1166/jnn.2012.6675`. URL: `%3CGo%20to%20ISI%3E://WOS:000313851000040`.

[19] K. S. Vasu, S. Sampath, and A. K. Sood. “Nonvolatile unipolar resistive switching in ultrathin films of graphene and carbon nanotubes”. In: *Solid State Communications* 151.16 (2011), pp. 1084–1087. ISSN: 0038-1098. DOI: `https://doi.org/10.1016/j.ssc.2011.05.018`. URL: `https://www.sciencedirect.com/science/article/pii/S0038109811002535`.

[20] Chengbin Pan et al. “Coexistence of Grain-Boundaries-Assisted Bipolar and Threshold Resistive Switching in Multilayer Hexagonal Boron Nitride”. In: *Advanced Functional Materials* 27.10 (2017), p. 1604811. ISSN: 1616-301X. DOI: `https://doi.org/10.1002/adfm.201604811`. URL: `https://onlinelibrary.wiley.com/doi/abs/10.1002/adfm.201604811`.

[21] Pingping Zhuang et al. “Nonpolar Resistive Switching of Multilayer-hBN-Based Memories”. In: *Advanced Electronic Materials* 6.1 (2020), p. 1900979. ISSN: 2199-160X. DOI: `https://doi.org/10.1002/aelm.201900979`. URL: `https://onlinelibrary.wiley.com/doi/abs/10.1002/aelm.201900979`.

[22] Hokyeong Jeong et al. “Resistive Switching in Few-Layer Hexagonal Boron Nitride Mediated by Defects and Interfacial Charge Transfer”. In: *ACS Applied Materials & Interfaces* 12.41 (2020). doi: 10.1021/acsami.0c12012, pp. 46288–46295. ISSN: 1944-8244. DOI: `10.1021/acsami.0c12012`. URL: `https://doi.org/10.1021/acsami.0c12012`.

[23] Jing-Yu Mao et al. “A van der Waals Integrated Damage-Free Memristor Based on Layered 2D Hexagonal Boron Nitride”. In: *Small* 18.12 (2022), p. 2106253. ISSN: 1613-6810. DOI: `https://doi.org/10.1002/smll.202106253`. URL: `https://onlinelibrary.wiley.com/doi/abs/10.1002/smll.202106253`.

[24] Yuchao Yang et al. “Observation of conducting filament growth in nanoscale resistive memories”. In: *Nature Communications* 3.1 (2012), p. 732. ISSN: 2041-1723. DOI: `10.1038/ncomms1737`. URL: `https://doi.org/10.1038/ncomms1737`.

[25] Shubhadeep Bhattacharjee et al. “Insights into Multilevel Resistive Switching in Monolayer MoS2”. In: *ACS Applied Materials & Interfaces* 12.5 (2020). doi: 10.1021/acsami.9b15677, pp. 6022–6029. ISSN: 1944-8244. DOI: `10.1021/acsami.9b15677`. URL: `https://doi.org/10.1021/acsami.9b15677`.

[26] Melkamu Belete et al. “Nonvolatile Resistive Switching in Nanocrystalline Molybdenum Disulfide with Ion-Based Plasticity”. In: *Advanced Electronic Materials* 6.3 (2020), p. 1900892. ISSN: 2199-160X. DOI: `https://doi.org/10.1002/aelm.201900892`. URL: `https://onlinelibrary.wiley.com/doi/abs/10.1002/aelm.201900892`.

[27] Renjing Xu et al. “Vertical MoS2 Double-Layer Memristor with Electrochemical Metallization as an Atomic-Scale Synapse with Switching Thresholds Approaching 100 mV”. In: *Nano Letters* 19.4 (2019). doi: 10.1021/acs.nanolett.8b05140, pp. 2411–2417. ISSN: 1530-6984. DOI: `10.1021/acs.nanolett.8b05140`. URL: `https://doi.org/10.1021/acs.nanolett.8b05140`.

[28] Vinod K. Sangwan et al. “Gate-tunable memristive phenomena mediated by grain boundaries in single-layer MoS2”. In: *Nature Nanotechnology* 10.5 (2015), pp. 403–406. ISSN: 1748-3395. DOI: `10.1038/nnano.2015.56`. URL: `https://doi.org/10.1038/nnano.2015.56`.

[29] Vinod K. Sangwan et al. “Multi-terminal memtransistors from polycrystalline monolayer molybdenum disulfide”. In: *Nature* 554.7693 (2018), pp. 500–504. ISSN: 1476-4687. DOI: `10.1038/nature25747`. URL: `https://doi.org/10.1038/nature25747`.

[30] Peifu Cheng, Kai Sun, and Yun Hang Hu. “Memristive Behavior and Ideal Memristor of 1T Phase MoS2 Nanosheets”. In: *Nano Letters* 16.1 (2016). doi: 10.1021/acs.nanolett.5b04260, pp. 572–576. ISSN: 1530-6984. DOI: `10.1021/acs.nanolett.5b04260`. URL: `https://doi.org/10.1021/acs.nanolett.5b04260`.

[31] Xiaojian Zhu et al. “Ionic modulation and ionic coupling effects in MoS2 devices for neuromorphic computing”. In: *Nature Materials* 18.2 (2019), pp. 141–148. ISSN: 1476-4660. DOI: `10.1038/s41563-018-0248-5`. URL: `https://doi.org/10.1038/s41563-018-0248-5`.

[32] Bert Voigtländer. *Scanning Probe Microscopy : Atomic Force Microscopy and Scanning Tunneling Microscopy*. Springer Berlin Heidelberg, 2015. DOI: `10.1007/978-3-662-45240-0`.

[33] Roland Wiesendanger. *Scanning Probe Microscopy and Spectroscopy: Methods and Applications*. Cambridge University Press, 1994. DOI: `10.1017/CBO9780511524356`.

[34] Kyle Godin, Christian Cupo, and Eui-Hyeok Yang. "Reduction in Step Height Variation and Correcting Contrast Inversion in Dynamic AFM of WS2 Monolayers". In: *Scientific Reports* 7.1 (2017), p. 17798. ISSN: 2045-2322. DOI: `10.1038/s41598-017-18077-4`. URL: `https://doi.org/10.1038/s41598-017-18077-4`.

[35] Felix Loske, Philipp Rahe, and Angelika Kühnle. "Contrast inversion in non-contact atomic force microscopy imaging of $C_6$0 molecules". In: *Nanotechnology* 20.26 (2009), p. 264010. ISSN: 0957-4484. DOI: `10.1088/0957-4484/20/26/264010`. URL: `http://dx.doi.org/10.1088/0957-4484/20/26/264010`.

[36] Ivan Mukhin et al. "Influence of condensation enhancement effect on AFM image contrast inversion in hydrophilic nanocapillaries". In: *Applied Surface Science* 471 (2019), pp. 621–626. ISSN: 0169-4332. DOI: `https://doi.org/10.1016/j.apsusc.2018.11.212`. URL: `https://www.sciencedirect.com/science/article/pii/S0169433218332926`.

[37] Inger Ekvall et al. "Preparation and characterization of electrochemically etched W tips for STM". In: *Measurement Science and Technology* 10.1 (1999), pp. 11–18. ISSN: 0957-0233. DOI: `10.1088/0957-0233/10/1/006`. URL: `http://dx.doi.org/10.1088/0957-0233/10/1/006`.

[38] J. P. Ibe et al. "On the electrochemical etching of tips for scanning tunneling microscopy". In: *Journal of Vacuum Science & Technology A* 8.4 (1990), pp. 3570–3575. DOI: `10.1116/1.576509`. URL: `https://doi.org/10.1116/1.576509`.

[39] Bowen Li et al. "Fabricating ultra-sharp tungsten STM tips with high yield: double-electrolyte etching method and machine learning". In: *SN Applied Sciences* 2.7 (2020), p. 1246. ISSN: 2523-3971. DOI: `10.1007/s42452-020-3017-4`. URL: `https://doi.org/10.1007/s42452-020-3017-4`.

[40] Shobhana Narasimhan and David Vanderbilt. "Elastic stress domains and the herringbone reconstruction on Au(111)". In: *Phys. Rev. Lett.* 69 (10 1992), pp. 1564–1567. DOI: `10.1103/PhysRevLett.69.1564`. URL: `https://link.aps.org/doi/10.1103/PhysRevLett.69.1564`.

[41] Ch. Wöll et al. "Determination of atom positions at stacking-fault dislocations on Au(111) by scanning tunneling microscopy". In: *Phys. Rev. B* 39 (11 1989), pp. 7988–7991. DOI: `10.1103/PhysRevB.39.7988`. URL: `https://link.aps.org/doi/10.1103/PhysRevB.39.7988`.

[42] J. V. Barth et al. "Scanning tunneling microscopy observations on the reconstructed Au(111) surface: Atomic structure, long-range superstructure, rotational domains, and surface defects". In: *Phys. Rev. B* 42 (15 1990), pp. 9307–9318. DOI: `10.1103/PhysRevB.42.9307`. URL: `https://link.aps.org/doi/10.1103/PhysRevB.42.9307`.

[43] W. Chen et al. "Scanning Tunneling Microscopy Observation of an Electronic Superlattice at the Surface of Clean Gold". In: *Physical Review Letters* 80.7 (1998). PRL, pp. 1469–1472. DOI: `10.1103/PhysRevLett.80.1469`. URL: `https://link.aps.org/doi/10.1103/PhysRevLett.80.1469`.

[44] Won-Yong Lee et al. "Layer dependence of out-of-plane electrical conductivity and Seebeck coefficient in continuous mono- to multilayer MoS2 films". In: *Journal of Materials Chemistry A* 9.47 (2021), pp. 26896–26903. ISSN: 2050-7488. DOI: `10.1039/D1TA07854B`. URL: `http://dx.doi.org/10.1039/D1TA07854B`.

[45] Tennyson Smith. “The hydrophilic nature of a clean gold surface”. In: *Journal of Colloid and Interface Science* 75.1 (1980), pp. 51–55. ISSN: 0021-9797. DOI: `https://doi.org/10.1016/0021-9797(80)90348-3`. URL: `https://www.sciencedirect.com/science/article/pii/0021979780903483`.

[46] M. Velicky et al. “Mechanism of Gold-Assisted Exfoliation of Centimeter-Sized Transition-Metal Dichalcogenide Monolayers”. In: *ACS Nano* 12.10 (2018), pp. 10463–10472. ISSN: 1936-086X (Electronic), 1936-0851 (Linking). DOI: `10.1021/acsnano.8b06101`. URL: `https://www.ncbi.nlm.nih.gov/pubmed/30265515`.

[47] Horacio Coy Diaz, Rafik Addou, and Matthias Batzill. “Interface properties of CVD grown graphene transferred onto MoS2(0001)”. In: *Nanoscale* 6.2 (2014), pp. 1071–1078. ISSN: 2040-3364. DOI: `10.1039/C3NR03692H`. URL: `http://dx.doi.org/10.1039/C3NR03692H`.

[48] DaeEung Lee, Gwanghyun Ahn, and Sunmin Ryu. “Two-Dimensional Water Diffusion at a Graphene–Silica Interface”. In: *Journal of the American Chemical Society* 136.18 (2014). doi: 10.1021/ja4121988, pp. 6634–6642. ISSN: 0002-7863. DOI: `10.1021/ja4121988`. URL: `https://doi.org/10.1021/ja4121988`.

[49] A. Pirkle et al. “The effect of chemical residues on the physical and electrical properties of chemical vapor deposited graphene transferred to SiO2”. In: *Applied Physics Letters* 99.12 (2011), p. 122108. DOI: `10.1063/1.3643444`. URL: `https://aip.scitation.org/doi/abs/10.1063/1.3643444`.

[50] Masa Ishigami et al. “Atomic Structure of Graphene on SiO2”. In: *Nano Letters* 7.6 (2007), pp. 1643–1648. ISSN: 1530-6984. DOI: `10.1021/nl070613a`. URL: `https://doi.org/10.1021/nl070613a`.

[51] I. Horcas et al. “WSXM: A software for scanning probe microscopy and a tool for nanotechnology”. In: *Review of Scientific Instruments* 78.1 (2007), p. 013705. DOI: `10.1063/1.2432410`. URL: `https://aip.scitation.org/doi/abs/10.1063/1.2432410`.

[52] David Nečas and Petr Klapetek. “Gwyddion: an open-source software for SPM data analysis”. In: *Central European Journal of Physics* 10 (1 2012), pp. 181–188. ISSN: 1895-1082. DOI: `10.2478/s11534-011-0096-2`.

[53] A. C. Ferrari et al. “Raman Spectrum of Graphene and Graphene Layers”. In: *Physical Review Letters* 97 (18 2006), p. 187401. DOI: `10.1103/PhysRevLett.97.187401`. URL: `https://link.aps.org/doi/10.1103/PhysRevLett.97.187401`.

[54] Andrea C. Ferrari and Denis M. Basko. “Raman spectroscopy as a versatile tool for studying the properties of graphene”. In: *Nature Nanotechnology* 8.4 (2013), pp. 235–246. ISSN: 1748-3395. DOI: `10.1038/nnano.2013.46`. URL: `https://doi.org/10.1038/nnano.2013.46`.

[55] Yufeng Hao et al. “Probing Layer Number and Stacking Order of Few-Layer Graphene by Raman Spectroscopy”. In: *Small* 6.2 (2010), pp. 195–200. DOI: `https://doi.org/10.1002/smll.200901173`. eprint: `https://onlinelibrary.wiley.com/doi/pdf/10.1002/smll.200901173`. URL: `https://onlinelibrary.wiley.com/doi/abs/10.1002/smll.200901173`.

[56] Jiang-Bin Wu et al. “Raman spectroscopy of graphene-based materials and its applications in related devices”. In: *Chemical Society Reviews* 47.5 (2018), pp. 1822–1873. ISSN: 0306-0012. DOI: `10.1039/C6CS00915H`. URL: `http://dx.doi.org/10.1039/C6CS00915H`.

[57] Changgu Lee et al. “Anomalous Lattice Vibrations of Single- and Few-Layer MoS2”. In: *ACS Nano* 4.5 (2010). doi: 10.1021/nn1003937, pp. 2695–2700. ISSN: 1936-0851. DOI: `10.1021/nn1003937`. URL: `https://doi.org/10.1021/nn1003937`.

[58] Hong Li et al. “From Bulk to Monolayer MoS2: Evolution of Raman Scattering”. In: *Advanced Functional Materials* 22.7 (2012), pp. 1385–1390. DOI: `https://doi.org/10.1002/adfm.201102111`. eprint: `https://onlinelibrary.wiley.com/doi/pdf/10.1002/adfm.201102111`. URL: `https://onlinelibrary.wiley.com/doi/abs/10.1002/adfm.201102111`.

[59] A. Michail et al. “Optical detection of strain and doping inhomogeneities in single layer MoS2”. In: *Applied Physics Letters* 108.17 (2016). doi: 10.1063/1.4948357, p. 173102. ISSN: 0003-6951. DOI: `10.1063/1.4948357`. URL: `https://doi.org/10.1063/1.4948357`.

[60] Woo Hyun Chae et al. “Substrate-induced strain and charge doping in CVD-grown monolayer MoS2”. In: *Applied Physics Letters* 111.14 (2017), p. 143106. DOI: `10.1063/1.4998284`. URL: `https://aip.scitation.org/doi/abs/10.1063/1.4998284`.

[61] Matěj Velický et al. “Strain and Charge Doping Fingerprints of the Strong Interaction between Monolayer MoS2 and Gold”. In: *The Journal of Physical Chemistry Letters* 11.15 (2020), pp. 6112–6118. DOI: `10.1021/acs.jpclett.0c01287`. URL: `https://doi.org/10.1021/acs.jpclett.0c01287`.

[62] Yuanbo Zhang et al. “Giant phonon-induced conductance in scanning tunnelling spectroscopy of gate-tunable graphene”. In: *Nature Physics* 4.8 (2008), pp. 627–630. ISSN: 1745-2481. DOI: `10.1038/nphys1022`. URL: `https://doi.org/10.1038/nphys1022`.

[63] Kin Fai Mak et al. “Atomically Thin MoS_2: A New Direct-Gap Semiconductor”. In: *Physical Review Letters* 105.13 (2010). PRL, p. 136805. DOI: `10.1103/PhysRevLett.105.136805`. URL: `https://link.aps.org/doi/10.1103/PhysRevLett.105.136805`.

[64] Brandon T. Blue et al. “Metallicity of 2H-MoS2 induced by Au hybridization”. In: *2D Materials* 7.2 (2020), p. 025021. ISSN: 2053-1583. DOI: `10.1088/2053-1583/ab6d34`. URL: `http://dx.doi.org/10.1088/2053-1583/ab6d34`.

[65] Franz R. Eder et al. “Probing from Both Sides: Reshaping the Graphene Landscape via Face-to-Face Dual-Probe Microscopy”. In: *Nano Letters* 13.5 (2013). doi: 10.1021/nl3042799, pp. 1934–1940. ISSN: 1530-6984. DOI: `10.1021/nl3042799`. URL: `https://doi.org/10.1021/nl3042799`.

[66] Saban M. Hus et al. “Observation of single-defect memristor in an MoS2 atomic sheet”. In: *Nature Nanotechnology* 16.1 (2021), pp. 58–62. ISSN: 1748-3395. DOI: `10.1038/s41565-020-00789-w`. URL: `https://doi.org/10.1038/s41565-020-00789-w`.

[67] Jesse E. Thompson, Darian Smalley, and Masahiro Ishigami. “Solar-Blind Ultraviolet Photodetectors Based on Vertical Graphene-Hexagonal Boron Nitride Heterostructures”. In: *MRS Advances* 5.37 (2020), pp. 1993–2002. ISSN: 2059-8521. DOI: `10.1557/adv.2020.331`. URL: `https://doi.org/10.1557/adv.2020.331`.

[68] Yutaka Matsumi and Masahiro Kawasaki. “Photolysis of Atmospheric Ozone in the Ultraviolet Region”. In: *Chemical Reviews* 103.12 (2003), pp. 4767–4782. ISSN: 0009-2665. DOI: `10.1021/cr0205255`. URL: `https://doi.org/10.1021/cr0205255`.

[69] G. Thuillier et al. “The Solar Spectral Irradiance from 200 to 2400 nm as Measured by the SOLSPEC Spectrometer from the Atlas and Eureca Missions”. In: *Solar Physics* 214.1 (2003), pp. 1–22. ISSN: 1573-093X. DOI: `10.1023/A:1024048429145`. URL: `https://doi.org/10.1023/A:1024048429145`.

[70] Peter C. Andersen, Craig J. Williford, and John W. Birks. “Miniature Personal Ozone Monitor Based on UV Absorbance”. In: *Analytical Chemistry* 82.19 (2010). doi: 10.1021/ac1013578, pp. 7924–7928. ISSN: 0003-2700. DOI: `10.1021/ac1013578`. URL: `https://doi.org/10.1021/ac1013578`.

[71] Michael H. Proffitt and Richard J. McLaughlin. “Fast-response dual-beam UV-absorption ozone photometer suitable for use on stratospheric balloons”. In: *Review of Scientific In-*

struments 54.12 (1983), pp. 1719–1728. ISSN: 0034-6748. DOI: `10.1063/1.1137316`. URL: `https://doi.org/10.1063/1.1137316`.

[72] E. J. Williams et al. “Comparison of Ultraviolet Absorbance, Chemiluminescence, and DOAS Instruments for Ambient Ozone Monitoring”. In: *Environmental Science & Technology* 40.18 (2006), pp. 5755–5762. ISSN: 0013-936X. DOI: `10.1021/es0523542`. URL: `https://doi.org/10.1021/es0523542`.

[73] Z. Xu and B. M. Sadler. “Ultraviolet Communications: Potential and State-Of-The-Art”. In: *IEEE Communications Magazine* 46.5 (2008), pp. 67–73. ISSN: 1558-1896. DOI: `10.1109/MCOM.2008.4511651`.

[74] P. Cheong et al. “A ZigBee-Based Wireless Sensor Network Node for Ultraviolet Detection of Flame”. In: *IEEE Transactions on Industrial Electronics* 58.11 (2011), pp. 5271–5277. ISSN: 1557-9948. DOI: `10.1109/TIE.2011.2119455`.

[75] A. Lavrov et al. “Application of lidar in ultraviolet, visible and infrared ranges for early forest fire detection”. In: *Applied Physics B* 76.1 (2003), pp. 87–95. ISSN: 1432-0649. DOI: `10.1007/s00340-002-1053-y`. URL: `https://doi.org/10.1007/s00340-002-1053-y`.

[76] Zhengyuan Xu et al. “Experimental performance evaluation of non-line-of-sight ultraviolet communication systems”. In: *Free-Space Laser Communications VII*. Ed. by Arun K. Majumdar and Christopher C. Davis. Vol. 6709. International Society for Optics and Photonics. SPIE, 2007, pp. 287–298. DOI: `10.1117/12.735183`. URL: `https://doi.org/10.1117/12.735183`.

[77] Daoyou Guo et al. “Zero-Power-Consumption Solar-Blind Photodetector Based on β-Ga_2O_3/NSTO Heterojunction”. In: *ACS Applied Materials & Interfaces* 9.2 (2017), pp. 1619–1628. ISSN: 1944-8244. DOI: `10.1021/acsami.6b13771`. URL: `https://doi.org/10.1021/acsami.6b13771`.

[78] X. C. Guo et al. “β-Ga_2O_3/p-Si heterojunction solar-blind ultraviolet photodetector with enhanced photoelectric responsivity”. In: *Journal of Alloys and Compounds* 660 (2016), pp. 136–140. ISSN: 0925-8388. DOI: `10.1016/j.jallcom.2015.11.145`. URL: `http://www.sciencedirect.com/science/article/pii/S0925838815317011`.

[79] Xuanhu Chen et al. “Review of gallium-oxide-based solar-blind ultraviolet photodetectors”. In: *Photonics Research* 7.4 (2019). ISSN: 2327-9125. DOI: `10.1364/prj.7.000381`.

[80] Hongyu Chen et al. “Ultrasensitive Self-Powered Solar-Blind Deep-Ultraviolet Photodetector Based on All-Solid-State Polyaniline/MgZnO Bilayer”. In: *Small* 12.42 (2016), pp. 5809–5816. ISSN: 1613-6810. DOI: `10.1002/smll.201601913`. URL: `https://onlinelibrary.wiley.com/doi/abs/10.1002/smll.201601913`.

[81] Xing Chen et al. “Self-Powered Solar-Blind Photodetector with Fast Response Based on Au/β-Ga_2O_3 Nanowires Array Film Schottky Junction”. In: *ACS Applied Materials & Interfaces* 8.6 (2016), pp. 4185–4191. ISSN: 1944-8244. DOI: `10.1021/acsami.5b11956`. URL: `https://doi.org/10.1021/acsami.5b11956`.

[82] Bin Zhao et al. “An Ultrahigh Responsivity (9.7 mA W^{-1}) Self-Powered Solar-Blind Photodetector Based on Individual ZnO–Ga_2O_3 Heterostructures”. In: *Advanced Functional Materials* 27.17 (2017), p. 1700264. ISSN: 1616-301X. DOI: `10.1002/adfm.201700264`. URL: `https://onlinelibrary.wiley.com/doi/abs/10.1002/adfm.201700264`.

[83] Xuanhu Chen et al. “Review of gallium-oxide-based solar-blind ultraviolet photodetectors”. In: *Photonics Research* 7.4 (2019), pp. 381–415. DOI: `10.1364/PRJ.7.000381`. URL: `http://opg.optica.org/prj/abstract.cfm?URI=prj-7-4-381`.

[84] G. Cassabois, P. Valvin, and B. Gil. “Hexagonal boron nitride is an indirect bandgap semiconductor”. In: *Nature Photonics* 10.4 (2016), pp. 262–266. ISSN: 1749-4893. DOI: `10.1038/nphoton.2015.277`. URL: `https://doi.org/10.1038/nphoton.2015.277`.

[85] Kenji Watanabe, Takashi Taniguchi, and Hisao Kanda. “Direct-bandgap properties and evidence for ultraviolet lasing of hexagonal boron nitride single crystal”. In: *Nature Materials* 3.6 (2004), pp. 404–409. ISSN: 1476-4660. DOI: `10.1038/nmat1134`. URL: `https://doi.org/10.1038/nmat1134`.

[86] Li Song et al. “Large Scale Growth and Characterization of Atomic Hexagonal Boron Nitride Layers”. In: *Nano Letters* 10.8 (2010), pp. 3209–3215. ISSN: 1530-6984. DOI: `10.1021/nl1022139`. URL: `https://doi.org/10.1021/nl1022139`.

[87] A. Zunger, A. Katzir, and A. Halperin. “Optical properties of hexagonal boron nitride”. In: *Physical Review B* 13.12 (1976). PRB, pp. 5560–5573. DOI: `10.1103/PhysRevB.13.5560`. URL: `https://link.aps.org/doi/10.1103/PhysRevB.13.5560`.

[88] Ki Kang Kim et al. “Synthesis of Monolayer Hexagonal Boron Nitride on Cu Foil Using Chemical Vapor Deposition”. In: *Nano Letters* 12.1 (2012). doi: 10.1021/nl203249a, pp. 161–166. ISSN: 1530-6984. DOI: `10.1021/nl203249a`. URL: `https://doi.org/10.1021/nl203249a`.

[89] A. M. Hassanien et al. “Effect of annealing temperature on structural and optical properties of gallium oxide thin films deposited by RF-sputtering”. In: *Optical and Quantum Electronics* 52.4 (2020), p. 194. ISSN: 1572-817X. DOI: `10.1007/s11082-020-02306-8`. URL: `https://doi.org/10.1007/s11082-020-02306-8`.

[90] Heng Liu et al. “High-performance deep ultraviolet photodetectors based on few-layer hexagonal boron nitride”. In: *Nanoscale* 10.12 (2018), pp. 5559–5565. ISSN: 2040-3364. DOI: `10.1039/C7NR09438H`. URL: `http://dx.doi.org/10.1039/C7NR09438H`.

[91] Changgu Lee et al. “Frictional Characteristics of Atomically Thin Sheets”. In: *Science* 328.5974 (2010), pp. 76–80. DOI: `doi:10.1126/science.1184167`. URL: `https://www.science.org/doi/abs/10.1126/science.1184167`.

[92] D. Pacilé et al. “The two-dimensional phase of boron nitride: Few-atomic-layer sheets and suspended membranes”. In: *Applied Physics Letters* 92.13 (2008), p. 133107. DOI: `10.1063/1.2903702`. URL: `https://aip.scitation.org/doi/abs/10.1063/1.2903702`.

[93] Miao Du, Yongzhong Wu, and Xiaopeng Hao. “A facile chemical exfoliation method to obtain large size boron nitride nanosheets”. In: *CrystEngComm* 15.9 (2013), pp. 1782–1786. DOI: `10.1039/C2CE26446C`. URL: `http://dx.doi.org/10.1039/C2CE26446C`.

[94] Zhiyuan Zeng et al. “An Effective Method for the Fabrication of Few-Layer-Thick Inorganic Nanosheets”. In: *Angewandte Chemie International Edition* 51.36 (2012), pp. 9052–9056. ISSN: 1433-7851. DOI: `https://doi.org/10.1002/anie.201204208`. URL: `https://onlinelibrary.wiley.com/doi/abs/10.1002/anie.201204208`.

[95] Václav Štengl et al. “Ultrasound exfoliation of inorganic analogues of graphene”. In: *Nanoscale Research Letters* 9.1 (2014), p. 167. ISSN: 1556-276X. DOI: `10.1186/1556-276X-9-167`. URL: `https://doi.org/10.1186/1556-276X-9-167`.

[96] Soo Min Kim et al. “Synthesis of large-area multilayer hexagonal boron nitride for high material performance”. In: *Nature Communications* 6.1 (2015), p. 8662. ISSN: 2041-1723. DOI: `10.1038/ncomms9662`. URL: `https://doi.org/10.1038/ncomms9662`.

[97] Yumeng Shi et al. “Synthesis of Few-Layer Hexagonal Boron Nitride Thin Film by Chemical Vapor Deposition”. In: *Nano Letters* 10.10 (2010). doi: 10.1021/nl1023707, pp. 4134–4139. ISSN: 1530-6984. DOI: `10.1021/nl1023707`. URL: `https://doi.org/10.1021/nl1023707`.

[98] Chandkiram Gautam and Selvam Chelliah. “Methods of hexagonal boron nitride exfoliation and its functionalization: covalent and non-covalent approaches”. In: *RSC Advances* 11.50 (2021), pp. 31284–31327. DOI: `10.1039/D1RA05727H`. URL: `http://dx.doi.org/10.1039/D1RA05727H`.

[99] Lu Hua Li et al. “Strong Oxidation Resistance of Atomically Thin Boron Nitride Nanosheets”. In: *ACS Nano* 8.2 (2014), pp. 1457–1462. ISSN: 1936-0851. DOI: `10.1021/nn500059s`. URL: `https://doi.org/10.1021/nn500059s`.

[100] Lu Hua Li et al. “Boron Nitride Nanosheets for Metal Protection”. In: *Advanced Materials Interfaces* 1.8 (2014), p. 1300132. ISSN: 2196-7350. DOI: `10.1002/admi.201300132`. URL: `https://onlinelibrary.wiley.com/doi/abs/10.1002/admi.201300132`.

[101] Esam Husain et al. “Marine Corrosion Protective Coatings of Hexagonal Boron Nitride Thin Films on Stainless Steel”. In: *ACS Applied Materials & Interfaces* 5.10 (2013), pp. 4129–4135. ISSN: 1944-8244. DOI: `10.1021/am400016y`. URL: `https://doi.org/10.1021/am400016y`.

[102] Insun Jo et al. “Thermal Conductivity and Phonon Transport in Suspended Few-Layer Hexagonal Boron Nitride”. In: *Nano Letters* 13.2 (2013), pp. 550–554. ISSN: 1530-6984. DOI: `10.1021/nl304060g`. URL: `https://doi.org/10.1021/nl304060g`.

[103] M. T. Alam et al. “Thermal conductivity of ultra-thin chemical vapor deposited hexagonal boron nitride films”. In: *Applied Physics Letters* 104.1 (2014). ISSN: 0003-6951 1077-3118. DOI: `10.1063/1.4861468`.

[104] Yanfeng Ji et al. “Boron nitride as two dimensional dielectric: Reliability and dielectric breakdown”. In: *Applied Physics Letters* 108.1 (2016), p. 012905. DOI: `10.1063/1.4939131`. URL: `https://aip.scitation.org/doi/abs/10.1063/1.4939131`.

[105] Sung Kyu Jang et al. “Synthesis and Characterization of Hexagonal Boron Nitride as a Gate Dielectric”. In: *Scientific Reports* 6.1 (2016), p. 30449. ISSN: 2045-2322. DOI: `10.1038/srep30449`. URL: `https://doi.org/10.1038/srep30449`.

[106] Yoshiaki Hattori et al. “Layer-by-Layer Dielectric Breakdown of Hexagonal Boron Nitride”. In: *ACS Nano* 9.1 (2015), pp. 916–921. ISSN: 1936-0851. DOI: `10.1021/nn506645q`. URL: `https://doi.org/10.1021/nn506645q`.

[107] J. W. McPherson et al. “Trends in the ultimate breakdown strength of high dielectric-constant materials”. In: *IEEE Transactions on Electron Devices* 50.8 (2003), pp. 1771–1778. ISSN: 0018-9383. DOI: `10.1109/ted.2003.815141`.

[108] Heng Liu et al. “High-performance deep ultraviolet photodetectors based on few-layer hexagonal boron nitride”. In: *Nanoscale* 10.12 (2018), pp. 5559–5565. ISSN: 2040-3364. DOI: `10.1039/C7NR09438H`. URL: `http://dx.doi.org/10.1039/C7NR09438H`.

[109] Ren-Jye Shiue et al. “High-Responsivity Graphene–Boron Nitride Photodetector and Autocorrelator in a Silicon Photonic Integrated Circuit”. In: *Nano Letters* 15.11 (2015), pp. 7288–7293. ISSN: 1530-6984. DOI: `10.1021/acs.nanolett.5b02368`. URL: `https://doi.org/10.1021/acs.nanolett.5b02368`.

[110] Manuel Rivera et al. “High Operating Temperature and Low Power Consumption Boron Nitride Nanosheets Based Broadband UV Photodetector”. In: *Scientific Reports* 7.1 (2017), p. 42973. ISSN: 2045-2322. DOI: `10.1038/srep42973`. URL: `https://doi.org/10.1038/srep42973`.

[111] Manuel Rivera et al. “UV photodetector based on energy bandgap shifted hexagonal boron nitride nanosheets for high-temperature environments”. In: *Journal of Physics D: Applied Physics* 51.4 (2018), p. 045102. ISSN: 0022-3727. DOI: `10.1088/1361-6463/aa9fa8`. URL: `http://dx.doi.org/10.1088/1361-6463/aa9fa8`.

[112] Shou-En Zhu, Shengjun Yuan, and G. C. A. M. Janssen. “Optical transmittance of multilayer graphene”. In: *EPL (Europhysics Letters)* 108.1 (2014), p. 17007. ISSN: 0295-5075. DOI: `10.1209/0295-5075/108/17007`. URL: `http://dx.doi.org/10.1209/0295-5075/108/17007`.

[113] Wei Li et al. "Broadband optical properties of graphene by spectroscopic ellipsometry". In: *Carbon* 99 (2016), pp. 348–353. ISSN: 0008-6223. DOI: `https://doi.org/10.1016/j.carbon.2015.12.007`. URL: `https://www.sciencedirect.com/science/article/pii/S0008622315304991`.

[114] Kin Fai Mak et al. "Optical spectroscopy of graphene: From the far infrared to the ultraviolet". In: *Solid State Communications* 152.15 (2012), pp. 1341–1349. ISSN: 0038-1098. DOI: `https://doi.org/10.1016/j.ssc.2012.04.064`. URL: `https://www.sciencedirect.com/science/article/pii/S0038109812002700`.

[115] Thomas Germer, Joanne C. Zwinkels, and Benjamin K. Tsai. *Spectrophotometry: Accurate Measurement of Optical Properties of Materials*. Vol. 46. San Diego: Elsevier Science & Technology, 2014. ISBN: 0123860229.

[116] J. Tauc, R. Grigorovici, and A. Vancu. "Optical Properties and Electronic Structure of Amorphous Germanium". In: *physica status solidi (b)* 15.2 (1966), pp. 627–637. ISSN: 0370-1972. DOI: `10.1002/pssb.19660150224`. URL: `https://onlinelibrary.wiley.com/doi/abs/10.1002/pssb.19660150224`.

[117] Maria Losurdo et al. "Graphene CVD growth on copper and nickel: role of hydrogen in kinetics and structure". In: *Physical Chemistry Chemical Physics* 13.46 (2011), pp. 20836–20843. ISSN: 1463-9076. DOI: `10.1039/C1CP22347J`. URL: `http://dx.doi.org/10.1039/C1CP22347J`.

[118] Choon-Ming Seah, Siang-Piao Chai, and Abdul Rahman Mohamed. "Mechanisms of graphene growth by chemical vapour deposition on transition metals". In: *Carbon* 70 (2014), pp. 1–21. ISSN: 0008-6223. DOI: `https://doi.org/10.1016/j.carbon.2013.12.073`. URL: `https://www.sciencedirect.com/science/article/pii/S0008622313012281`.

[119] Xuesong Li, Luigi Colombo, and Rodney S. Ruoff. "Synthesis of Graphene Films on Copper Foils by Chemical Vapor Deposition". In: *Advanced Materials* 28.29 (2016), pp. 6247–6252. ISSN: 0935-9648. DOI: `https://doi.org/10.1002/adma.201504760`. URL: `https://onlinelibrary.wiley.com/doi/abs/10.1002/adma.201504760`.

[120] Philipp Braeuninger-Weimer et al. "Understanding and Controlling Cu-Catalyzed Graphene Nucleation: The Role of Impurities, Roughness, and Oxygen Scavenging". In: *Chemistry of Materials* 28.24 (2016). doi: 10.1021/acs.chemmater.6b03241, pp. 8905–8915. ISSN: 0897-4756. DOI: `10.1021/acs.chemmater.6b03241`. URL: `https://doi.org/10.1021/acs.chemmater.6b03241`.

[121] Dheeraj Golla et al. "Optical thickness determination of hexagonal boron nitride flakes". In: *Applied Physics Letters* 102.16 (2013), p. 161906. DOI: `10.1063/1.4803041`. URL: `https://aip.scitation.org/doi/abs/10.1063/1.4803041`.

[122] C. Elias et al. "Direct band-gap crossover in epitaxial monolayer boron nitride". In: *Nature Communications* 10.1 (2019), p. 2639. ISSN: 2041-1723. DOI: `10.1038/s41467-019-10610-5`. URL: `https://doi.org/10.1038/s41467-019-10610-5`.

[123] Yijing Stehle et al. "Synthesis of Hexagonal Boron Nitride Monolayer: Control of Nucleation and Crystal Morphology". In: *Chemistry of Materials* 27.23 (2015), pp. 8041–8047. ISSN: 0897-4756. DOI: `10.1021/acs.chemmater.5b03607`. URL: `https://doi.org/10.1021/acs.chemmater.5b03607`.

[124] Haolin Wang et al. "Synthesis of Large-Sized Single-Crystal Hexagonal Boron Nitride Domains on Nickel Foils by Ion Beam Sputtering Deposition". In: *Advanced Materials* 27.48 (2015), pp. 8109–8115. ISSN: 0935-9648. DOI: `10.1002/adma.201504042`. URL: `https://onlinelibrary.wiley.com/doi/abs/10.1002/adma.201504042`.

[125] Lijie Ci et al. “Atomic layers of hybridized boron nitride and graphene domains”. In: *Nature Materials* 9.5 (2010), pp. 430–435. ISSN: 1476-4660. DOI: `10.1038/nmat2711`. URL: `https://doi.org/10.1038/nmat2711`.

[126] Pavel Gevko et al. “Optical absorption of boron nitride nanomaterials”. In: *physica status solidi (b)* 245.10 (2008), pp. 2107–2110. ISSN: 0370-1972. DOI: `https://doi.org/10.1002/pssb.200879600`. URL: `https://onlinelibrary.wiley.com/doi/abs/10.1002/pssb.200879600`.

[127] Nathaniel M. Gabor et al. “Hot Carrier–Assisted Intrinsic Photoresponse in Graphene”. In: *Science* 334.6056 (2011), pp. 648–652. DOI: `10.1126/science.1211384`. URL: `https://science.sciencemag.org/content/sci/334/6056/648.full.pdf`.

[128] Xitao Guo et al. “High-performance graphene photodetector using interfacial gating”. In: *Optica* 3.10 (2016), pp. 1066–1070. DOI: `10.1364/OPTICA.3.001066`. URL: `http://opg.optica.org/optica/abstract.cfm?URI=optica-3-10-1066`.

[129] Hehai Fang and Weida Hu. “Photogating in Low Dimensional Photodetectors”. In: *Advanced Science* 4.12 (2017), p. 1700323. ISSN: 2198-3844. DOI: `https://doi.org/10.1002/advs.201700323`. URL: `https://onlinelibrary.wiley.com/doi/abs/10.1002/advs.201700323`.

[130] Fang Luo et al. “High responsivity graphene photodetectors from visible to near-infrared by photogating effect”. In: *AIP Advances* 8.11 (2018), p. 115106. DOI: `10.1063/1.5054760`. URL: `https://aip.scitation.org/doi/abs/10.1063/1.5054760`.

[131] Fengnian Xia et al. “Ultrafast graphene photodetector”. In: *Nature Nanotechnology* 4.12 (2009), pp. 839–843. ISSN: 1748-3395. DOI: `10.1038/nnano.2009.292`. URL: `https://doi.org/10.1038/nnano.2009.292`.

[132] Thomas Mueller, Fengnian Xia, and Phaedon Avouris. “Graphene photodetectors for high-speed optical communications”. In: *Nature Photonics* 4.5 (2010), pp. 297–301. ISSN: 1749-4893. DOI: `10.1038/nphoton.2010.40`. URL: `https://doi.org/10.1038/nphoton.2010.40`.

[133] Marco Furchi et al. “Microcavity-Integrated Graphene Photodetector”. In: *Nano Letters* 12.6 (2012). doi: 10.1021/nl204512x, pp. 2773–2777. ISSN: 1530-6984. DOI: `10.1021/nl204512x`. URL: `https://doi.org/10.1021/nl204512x`.

[134] Chang-Hua Liu et al. “Graphene photodetectors with ultra-broadband and high responsivity at room temperature”. In: *Nature Nanotechnology* 9.4 (2014), pp. 273–278. ISSN: 1748-3395. DOI: `10.1038/nnano.2014.31`. URL: `https://doi.org/10.1038/nnano.2014.31`.

[135] Nathaniel M. Gabor et al. “Hot Carrier-Assisted Intrinsic Photoresponse in Graphene”. In: *Science* 334.6056 (2011), pp. 648–652. DOI: `doi:10.1126/science.1211384`. URL: `https://www.science.org/doi/abs/10.1126/science.1211384`.

[136] Xiaodong Xu et al. “Photo-Thermoelectric Effect at a Graphene Interface Junction”. In: *Nano Letters* 10.2 (2010). doi: 10.1021/nl903451y, pp. 562–566. ISSN: 1530-6984. DOI: `10.1021/nl903451y`. URL: `https://doi.org/10.1021/nl903451y`.

[137] Mathieu Massicotte et al. “Hot carriers in graphene – fundamentals and applications”. In: *Nanoscale* 13.18 (2021), pp. 8376–8411. ISSN: 2040-3364. DOI: `10.1039/D0NR09166A`. URL: `http://dx.doi.org/10.1039/D0NR09166A`.

[138] Fu-Chien Chiu. “A Review on Conduction Mechanisms in Dielectric Films”. In: *Advances in Materials Science and Engineering* 2014 (2014), p. 578168. ISSN: 1687-8434. DOI: `10.1155/2014/578168`. URL: `https://doi.org/10.1155/2014/578168`.

[139] Joaquin F. Rodriguez-Nieva, Mildred S. Dresselhaus, and Justin C. W. Song. “Enhanced Thermionic-Dominated Photoresponse in Graphene Schottky Junctions”. In: *Nano Letters* 16.10 (2016). doi: 10.1021/acs.nanolett.6b01965, pp. 6036–6041. ISSN: 1530-6984. DOI: `10.1021/acs.nanolett.6b01965`. URL: `https://doi.org/10.1021/acs.nanolett.6b01965`.

[140] Young Rae Kim et al. “Unveiling the Hot Carrier Distribution in Vertical Graphene/h-BN/Au van der Waals Heterostructures for High-Performance Photodetector”. In: *ACS Applied Materials & Interfaces* 12.9 (2020). doi: 10.1021/acsami.9b19904, pp. 10772–10780. ISSN: 1944-8244. DOI: `10.1021/acsami.9b19904`. URL: `https://doi.org/10.1021/acsami.9b19904`.

[141] Qiong Ma et al. “Tuning ultrafast electron thermalization pathways in a van der Waals heterostructure”. In: *Nature Physics* 12.5 (2016), pp. 455–459. ISSN: 1745-2481. DOI: `10.1038/nphys3620`. URL: `https://doi.org/10.1038/nphys3620`.

[142] H. Hiraoka. “Radiation Chemistry of Poly(methacrylates)”. In: *IBM Journal of Research and Development* 21.2 (1977), pp. 121–130. ISSN: 0018-8646. DOI: `10.1147/rd.212.0121`.

[143] Alexei L. Bogdanov and Eva Karin Andersson. “Fine undercut control in bilayer PMMA-P(MMA-MAA) resist system for e-beam lithography with submicrometer resolution”. In: *Electron-Beam, X-Ray, and Ion-Beam Submicrometer Lithographies for Manufacturing*. Ed. by Martin C. Peckerar. Vol. 1465. International Society for Optics and Photonics. SPIE, 1991, pp. 324–329. DOI: `10.1117/12.47368`. URL: `https://doi.org/10.1117/12.47368`.

[144] C. R. Dean et al. “Boron nitride substrates for high-quality graphene electronics”. In: *Nature Nanotechnology* 5.10 (2010), pp. 722–726. ISSN: 1748-3395. DOI: `10.1038/nnano.2010.172`. URL: `https://doi.org/10.1038/nnano.2010.172`.

[145] Yuan Cao et al. "Unconventional superconductivity in magic-angle graphene superlattices". In: *Nature* 556.7699 (2018), pp. 43–50. ISSN: 1476-4687. DOI: `10.1038/nature26160`. URL: `https://doi.org/10.1038/nature26160`.

[146] L. Wang et al. "One-Dimensional Electrical Contact to a Two-Dimensional Material". In: *Science* 342.6158 (2013), pp. 614–617. DOI: `doi:10.1126/science.1244358`.

[147] Francois Chambon and H. Henning Winter. "Linear Viscoelasticity at the Gel Point of a Crosslinking PDMS with Imbalanced Stoichiometry". In: *Journal of Rheology* 31.8 (1987), pp. 683–697. DOI: `10.1122/1.549955`. URL: `https://sor.scitation.org/doi/abs/10.1122/1.549955`.

[148] Shinji Deguchi et al. "Viscoelastic and optical properties of four different PDMS polymers". In: *Journal of Micromechanics and Microengineering* 25.9 (2015), p. 097002. ISSN: 0960-1317. DOI: `10.1088/0960-1317/25/9/097002`. URL: `http://dx.doi.org/10.1088/0960-1317/25/9/097002`.

[149] Yoshiaki Hattori et al. "Impact ionization and transport properties of hexagonal boron nitride in a constant-voltage measurement". In: *Physical Review B* 97.4 (2018). PRB, p. 045425. DOI: `10.1103/PhysRevB.97.045425`. URL: `https://link.aps.org/doi/10.1103/PhysRevB.97.045425`.

[150] Chang Goo Kang et al. "Intrinsic photocurrent characteristics of graphene photodetectors passivated with Al2O3". In: *Optics Express* 21.20 (2013), pp. 23391–23400. DOI: `10.1364/OE.21.023391`. URL: `http://opg.optica.org/oe/abstract.cfm?URI=oe-21-20-23391`.

[151] Yang-Yang Hsu et al. "Optical-power-dependent photodesorption kinetics of graphene studied by conductance response". In: *Optics Express* 23.11 (2015), pp. 14344–14350. DOI: `10.1364/OE.23.014344`. URL: `http://opg.optica.org/oe/abstract.cfm?URI=oe-23-11-14344`.

[152] Yumeng Shi et al. “Photoelectrical Response in Single-Layer Graphene Transistors”. In: *Small* 5.17 (2009), pp. 2005–2011. ISSN: 1613-6810. DOI: `https://doi.org/10.1002/smll.200900294`. URL: `https://onlinelibrary.wiley.com/doi/abs/10.1002/smll.200900294`.

[153] Xinhua Pan et al. “High responsivity ultraviolet detector based on novel SnO2 nanoarrays”. In: *RSC Advances* 9.64 (2019), pp. 37201–37206. DOI: `10.1039/C9RA03999F`. URL: `http://dx.doi.org/10.1039/C9RA03999F`.

[154] Jingtian Fang, William G. Vandenberghe, and Massimo V. Fischetti. “Microscopic dielectric permittivities of graphene nanoribbons and graphene”. In: *Physical Review B* 94.4 (2016). PRB, p. 045318. DOI: `10.1103/PhysRevB.94.045318`. URL: `https://link.aps.org/doi/10.1103/PhysRevB.94.045318`.

[155] Elton J. G. Santos and Efthimios Kaxiras. “Electrically Driven Tuning of the Dielectric Constant in MoS2 Layers”. In: *ACS Nano* 7.12 (2013), pp. 10741–10746. ISSN: 1936-0851. DOI: `10.1021/nn403738b`. URL: `https://doi.org/10.1021/nn403738b`.

[156] Paul A. George et al. “Ultrafast Optical-Pump Terahertz-Probe Spectroscopy of the Carrier Relaxation and Recombination Dynamics in Epitaxial Graphene”. In: *Nano Letters* 8.12 (2008). doi: 10.1021/nl8019399, pp. 4248–4251. ISSN: 1530-6984. DOI: `10.1021/nl8019399`. URL: `https://doi.org/10.1021/nl8019399`.

[157] Farhan Rana et al. “Carrier recombination and generation rates for intravalley and intervalley phonon scattering in graphene”. In: *Physical Review B* 79.11 (2009). PRB, p. 115447. DOI: `10.1103/PhysRevB.79.115447`. URL: `https://link.aps.org/doi/10.1103/PhysRevB.79.115447`.

[158] F. T. Vasko and V. Ryzhii. “Voltage and temperature dependencies of conductivity in gated graphene”. In: *Physical Review B* 76.23 (2007). PRB, p. 233404. DOI: `10.1103/PhysRevB.76.233404`. URL: `https://link.aps.org/doi/10.1103/PhysRevB.76.233404`.

[159] Domenico De Fazio et al. “High-Mobility, Wet-Transferred Graphene Grown by Chemical Vapor Deposition”. In: *ACS Nano* 13.8 (2019). doi: 10.1021/acsnano.9b02621, pp. 8926–8935. ISSN: 1936-0851. DOI: `10.1021/acsnano.9b02621`. URL: `https://doi.org/10.1021/acsnano.9b02621`.